NOVA SCHOOL OF SCIENCE & TECHNOLOGY

DEPARTMENT OF MECHANICAL AND INDUSTRIAL ENGINEERING

Experimental characterization of liquid-liquid stratified flow interacting with vertical emergent cylinders

JOÃO PEDRO BARRADAS DO Ó RAMOS
BSc in Mechanical Engineering Sciences

MASTER IN MECHANICAL ENGINEERING
NOVA University Lisbon
November,2021

DEPARTMENT OF
MECHNICAL AND INDUSTRIAL
ENGINEERING

Experimental characterization of liquid-liquid stratified flow interacting with vertical emergent cylinders

João Pedro Barradas do Ó Ramos

BSc in Mechanical Engineering Sciences

Adviser: Moisés Gonçalves de Brito
Invited Assistant Professor, Department of Mechanical and Industrial Engineering, NOVA University Lisbon

Co-adviser: Ana Margarida da Costa Ricardo
Researcher, *Department of Civil Engineering,* IST-ID

Examination Committee:

Chair: José Fernando de Almeida Dias
Associate Professor, Department of Mechanical and Industrial Engineering, NOVA University Lisbon

Rapporteurs: Rui Miguel Laje Ferreira
Associate Professor, Department of Civil Engineering, IST-UL

Adviser: Moisés Gonçalves de Brito
Invited Assistant Professor, Department of Mechanical and Industrial Engineering, NOVA University Lisbon

MASTER IN MECHANICAL ENGINEERING
NOVA University Lisbon
November,2021

Experimental characterization of liquid-liquid stratified flow interacting with vertical emergent cylinders

Para a minha família e amigos.

Acknowledgments

This work was inserted in the WinTherface project and funded by national funds through Portuguese Foundation for Science and Technology (FCT) project PTDC/CTA-OHR/30561/2017.

My first words of gratitude are addressed to my thesis supervisors, Professors Moisés de Brito and Ana Ricardo for the support, knowledge, dedication and advice they gave to me during the different stages of the thesis. The constant follow-up during the experimental stage and the help given during the data treatment was crucial for the thesis progress and for that reason I would like to express my sincere gratefulness.

I also want to express my thanks to my laboratory colleagues during the thesis project, my italian friends Giovanni and Gianluca. The experimental work was much easier due to their presence and was good to have someone to talk and relax after the stressful and demanding work.

I also want to thank the professors I meet during my degree in NOVA School of Science and Technology. Without their help and enthusiasm to explain different subjects it would not be possible to make this journey with the success accomplished.

In the same way to the closest friends I made during my degree, I would like to express my gratitude for the good times I spent with them, for the moments they boost my moral when I was feeling down, the hours we studied together and the lessons I learn from them while we were working in different projects.

For last but not the least I would like to thank to my family for the values they gave me, the investment in my education all over the years and most important all kind of support and effort they put into me.

Abstract

Density currents are mainly horizontal flows that are driven by density differences between contacting flows, which may result from temperature gradients, suspended solid particles or dissolved substances. These currents play an important role in nature and industry as they can have a negative environmental impact through global ocean circulation, oil spills, climate variations through water formation and the redistribution of ocean or river water. They have been widely studied since the 20th century, but despite the data acquired and the experiments carried out to date, there is still much research to be done on understanding the dynamics of density currents and their environmental impact.

The present work is part of the WinTherface project that addresses the study of wind and temperature-driven mass exchange at wetland lake interfaces and its impacts on water quality through a multidisciplinary approach integrating, field, laboratory, and numerical work. The aim of the present work is to experimentally investigate how different initial current densities and the presence of vegetation interfere with the propagation and mass exchange between the current and the ambient fluid, as well as the turbulence mechanisms around a set of cylinders present in the channel.

The laboratorial tests were carried out in a channel containing a set of cylinders intended to simulate rigid vegetation. The lock exchange technique was used to generate the density currents with a reduced gravity of $0.09\ \mathrm{m}/s^2$ and $0.36\ \mathrm{m}/s^2$.

During the laboratory work several tests were carried out using the Particle Image Velocimetry (PIV) measuring technique and the image analysis technique. First the PIV system was used to measure the two-dimensional instantaneous velocity fields in two planes, these being called the side view and plan view which were situated near the cylinder array. After the PIV tests, the image analysis technique was used to mainly evaluate the mass distribution of the current. This technique consists of using a concentration of dye (Rhodamine) in the flow, allowing the understanding of the current dynamics, being able to analyse the temporal evolution of the current front, and the density, its height along the channel, as well as the entrainment evolution.

It is concluded that some parameters of the current such as the height, the position of the front and the entrainment suffer a change due to the interaction with the cylinders. With the results obtained by the PIV it was observed that the interaction of the current with the set of cylinders induces a strong vertical component in the flow becoming three-dimensional. This interaction creates in the flow a set of turbulent structures dominated by a large circulation area that is evident in the approximation area of the cylinders and increases the complexity of the turbulence mechanisms in the current.

Keywords: Density currents, laboratory tests, PIV, array of cylinders, lock-exchange

Resumo

As correntes de densidade são escoamentos principalmente horizontais que são impulsionados por diferenças de densidade entre escoamentos de contacto, que podem resultar de gradientes de temperatura, partículas sólidas em suspensão ou substâncias dissolvidas. Estas correntes desempenham um papel importante na natureza e na indústria, uma vez que podem ter um impacto ambiental negativo através da circulação oceânica global, derramamento de petróleo, variações climáticas através da formação de água e da redistribuição da água do oceano ou dos rios. Têm sido amplamente estudadas desde o século XX, mas apesar dos dados adquiridos e das experiências feitas até hoje, há ainda muito a pesquisar sobre a compreensão da dinâmica das correntes de densidade e o seu impacto ambiental.

O presente trabalho está inserido no âmbito do projeto WinTherface que aborda o estudo da troca de massas impulsionada pelo vento e pela temperatura em interfaces de lagoas húmidas e os seus impactos na qualidade da água através de uma abordagem multidisciplinar, que integra trabalho de campo, de laboratório e numérico. O objetivo do presente trabalho é investigar experimentalmente como as diferentes densidades iniciais de corrente e a presença de vegetação interferem na propagação e troca de massa entre a corrente e o fluido ambiente, bem como os mecanismos de turbulência em torno de um conjunto de cilindros presentes no canal.

Os testes laboratoriais foram realizados num canal que continha um conjunto de cilindros que pretendiam simular a vegetação rígida. Foi utilizada a técnica de *lock exchange* para gerar as correntes de densidade com uma gravidade reduzida de $0.09\ \mathrm{m}/s^2$ e $0.36\ \mathrm{m}/s^2$.

Durante o trabalho laboratorial foram realizados vários testes utilizando a técnica de medição de *Particle Image Velocimetry* (PIV) e a técnica de análise de imagem. Primeiro foi utilizado o sistema PIV para medir o campo bidimensional de velocidade instantânea em dois planos, sendo eles o plano horizontal e o vertical, que estavam situados perto do conjunto de cilindros. Após os testes de PIV, foi utilizada a técnica de análise de imagem para avaliar principalmente a distribuição da massa da corrente. Esta técnica consiste em utilizar uma concentração de corante (Rodamina) no fluxo, permitindo a compreensão da dinâmica da corrente, podendo analisar a evolução temporal da frente da corrente e da densidade, a sua altura ao longo do canal, bem como a evolução do *entrainment*.

Conclui-se que alguns parâmetros da corrente tais como a altura, a posição da frente e o *entrainment* sofrem uma alteração devido à interação com os cilindros. Com os resultados obtidos pelo PIV observou-se que a interação da corrente com o conjunto de cilindros induz uma forte componente vertical no escoamento passando a ser tridimensional. Esta interação cria no escoamento um conjunto de estruturas turbulentas dominadas por uma grande circulação que são evidentes na zona de aproximação aos cilindros e aumentam a complexidade dos mecanismos de turbulência na corrente.

Palavras-chave: Correntes de densidade, ensaios laboratoriais, PIV, conjunto de cilindros, *lock-exchange*

Table of Contents

List of Figures

List of Tables

Symbols and Abbreviations

Symbol	Designation	Units
b	Channel width	m
C	Concentration	-
d	Cylinder diameter	m
E	Entrainment parameter	-
F_r	Froude number	-
g	Gravitational acceleration	m/s^2
g'	Reduced gravity	m/s^2
h_0	Fluid initial depth	m
h	Current height	m
M	Mass	kg
R_e	Reynolds number	-
t	time	s
u	Longitudinal velocity	m/s
u_0	Buoyancy velocity	m/s
u_f	Current mean velocity	m/s
v	Transversal velocity	m/s
w	Vertical velocity	m/s
x	Longitudinal spatial coordinate	m
x_0	Lock position distance	m
x_f	Current front position	m
y	Transversal spatial coordinate	m
z	Vertical spatial coordinate	m
ρ_0	Ambient fluid density	kg/m^3
ρ_1	Denser fluid density	kg/m^3
v	Kinematic viscosity	m^2/s
Δt	Time between pulses	s

Abbreviation

LED	Light emitting diode
PIV	Particle Image velocimetry
PSP	Polyamide Seeding Particles
RGB	Red-Green-Blue
2D	Two-dimensional
3D	Three-dimensional

1 Introduction

1.1 Motivation

In transition zones from shallow lakes to wetlands, water flows may occur induced by density or wind-driven currents. Density currents, also known as gravity currents, are buoyancy driven flows where temperature gradients, concentration fields being created by dissolved particles and different chemical compositions contribute for a difference in density between two fluids.

These currents can play a key role in transporting nutrients and pollutants, affecting the ecological status of water bodies. An example of the effects of the density currents transport is shown in Figure 1.1, where Cooper River spills light grey sediments into the open sea in the Gulf of Alaska, affecting the water quality in that region. Therefore, the transport capacity of these currents is of great importance in water quality management and industrial safety. In this sense it is essential to characterize the dynamics of density currents, namely which are the conditions that sustain the flow structure.

Figure 1.1: Effects of density currents transport in Cooper River.

The dynamics of density currents in lakes depends on several parameters, such as difference in fluid densities, presence of vegetation, wind direction and velocity, roughness of boundaries and geometry of the transitions between lakes and wetlands. Therefore, the detailed description of the dynamics of density currents is extremely complex. In this sense, several studies have been carried out considering isolated effects of each parameter. However, the interaction of the effects of difference of densities and the presence of vegetation was not yet conveniently studied. In this context, the starting question of this research work is:

"How do the different initial current densities and the presence of submersed vegetation interfere in the propagation and mass exchange between the current and the ambient fluid?"

There are other questions for the motivation of the thesis such as:

- Are the vortex shedding mechanisms in the array different from those occurring in the isolated cylinder?

- What type of structures are formed as the current approaches the array of emergent cylinders?

This work seeks to answer these questions by carrying out laboratory work as presented in the next chapters.

1.2 Objectives

The thesis objective is to experimentally study the presence of an array of emergent cylinders, simulating rigid vegetation, in density currents structure. It will be also analysed and make a comparison to the case where was only used an isolated cylinder in the channel, using the data acquired in a previous project. To effectively study the presence of an array of cylinders, several small objectives will be taken in consider such as:

- Evaluate the kinematics of the current through parameters such as the evolution of the current front and current height.
- Characterize the density fields.
- Characterize the dilution of the current.
- Evaluate the velocity fields and turbulent structures in the current plan view.
- Evaluate the velocity fields and turbulent structures in the current side view.
- Comparing the turbulent structures results to the case where an isolated cylinder was used

1.3 Methodology

For the present work was used the method called “full depth lock-exchange” to produce density currents in a channel. This method consists in dividing the channel in two with a lock, filling it on one side with a dense fluid and on the other side with a lower density ambient fluid. It is important to refer the initial height of the two fluids is the same.

To correctly perform this method the lock needs to be quickly removed. When that happens, the column of dense fluid collapses and begins to propagate along the bottom of the channel, towards the ambient fluid, due to the hydrostatic pressure difference. As the density current propagates downstream, the ambient fluid flows in the opposite direction.

In this thesis were studied two different values of reduced gravitational acceleration, g', to characterize its influence on the current. Were employed two techniques of analysis, the PIV (Particle Image Velocimetry) and the image analysis technique for the high-speed video recording.

For each value of g' regarding the plan being viewed, were performed 10 repetitions to obtain an average, based on a number of repetitions large enough to reduce experimental errors and to have a sufficient number of statistical evidence.

The array of cylinders consists in 31 lines of three bulk cylinders side by side placed in the second half of the channel. The cylinders have a diameter of 2 cm, were separated 2.5 cm from each other and each line distant 2.5 cm from another.

1.4 Structure of the Dissertation

The following document is divided into 6 chapters and different appendixes:

Chapter 1: Introduction.

Chapter 2: State-of-art review

Chapter 3: Description of experimental tests

Chapter 4: Density field characteristics

Chapter 5: Velocity field characteristics

Chapter 6: Conclusion and future work

Chapter 1 presents an introduction of the topic under discussion with a slight theoretical approach, with the objectives of the work, the methodology used and the document structure.

In Chapter 2 the topic of these thesis will be discussed in detail, explaining the state-of-art of density currents.

Chapter 3 deals with the experimental method, where the experimental set-up will be described, the experimental procedure will be explained and how the data was collected and the mechanism of the data analysis for the PIV and concentration tests will also be discussed.

Chapter 4 and 5 are related to the analysis and discussion of the given results, where the chapter 4 it is related to the concentration tests and the chapter 5 to the PIV tests. Finally in chapter 6 a summary of the present thesis is done, it is proposed themes for development in the experimental field regarding density currents study, as well as conclusions drawn about the obtained results.

2 State-of-art review

The present chapter provides a general view on the topic of density currents, and it is divided in five main sections. The first is related to density currents in nature, in the second it´s given the definition of a density current and their morphology when generated by the lock exchange technique. The third part addresses the fundamental characterization of these type of currents, where is given the definition of some parameters. The fourth is related to the interaction of the current with bluff obstacles, which is the focus of this thesis. Finally, the last section presents a brief literature review on the experimental methodologies that were used in the laboratory.

2.1 Density currents in the nature

As stated in section 1.1, a density current can be defined as buoyancy driven flows where temperature gradients, concentration fields being created by dissolved particles and different chemical compositions contribute for a difference in density between two fluids. Besides being present in water, density currents can also be present in the atmosphere because of temperature gradients acting as the primary force, and one of the best examples are thunderstorms, Figure 2.1. They are generated by a heated air moving vertically upwards during unstable conditions (Simpson,1982). When the front reaches the tropopause, the mass of air starts to spread out. Rain and hail produce a descending flow of cold air towards the ground and since this cold air is denser than the ambient air, it can expand and generate a density current when it reaches the ground.

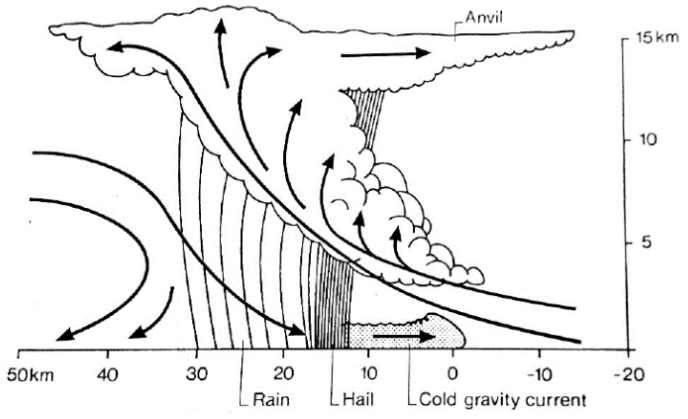

Figure 2.1 : Example of an atmospheric density current in the nature (thunderstorm).

Temperature gradients are also responsible to create the sea breezes phenomenon, where a cold air mass above the sea flows under the warm air mass heated by the land (Simpson, 1982).

The analyses of sea breeze phenomenon it´s important for the understanding of the distribution of airborne pollutants where the concentration of air contaminants is severely increased by recirculation flows.

Another type of well-known density current are the snow avalanches and volcanic density currents. In the avalanche a flow of snow separated from the rest generates a rapid density current down a slope such a hill or mountain. For the volcanic density current, they are associated with the emergence of material from the magma, as the molten rock beneath the grounds forms currents whose nature is correlated to the magma viscosity and the quantity of dissolved gas contained under pressure (Simpson, 1982).

2.2 Density currents definition and morphology

Density currents can be defined as the flow of a fluid with a certain density, ρ_1, within an ambient fluid with a different density, ρ_0 . Mainly the density gradient between fluids in this type of currents it is horizontal but when the flows are generated by a vertical gradient they are called as plumes. Density currents can be classified as bottom currents when the current is denser than the ambient fluid, $\rho_1 > \rho_0$, which is shown in Figure 2.2 (Isabel & Nogueira, 2013) and top boundary density current when the ambient fluid is denser $\rho_0 > \rho_1$. For this classification it is important to consider the type of density differences between the fluids and the stratification of the ambient fluid.

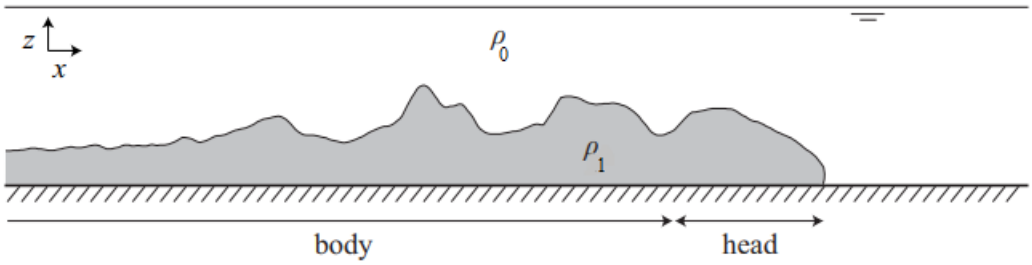

Figure 2.2: Scheme of a bottom density current with density ρ_1 intruding in the less dense ambient fluid with uniform density ρ_0 (Isabel & Nogueira, 2013).

Regarding the morphology of density current, these are formed by a head region, or front, that advances into the ambient fluid, being followed by the body or tail.

According to (Simpson, 1982), although there is intense mixing occurring in the current is possible to find a sharp dividing line between the two fluids. Normally the current head is deeper than the following flow and the upper part of the head is a zone where the breaking waves and a strong mixing plays an important role on all the current control. On a horizontal moving current, the head can be described as unsteady but in the presence of a slope the head increases with the angle of the slope.

Usually, the foremost point of the current generates an elevated nose that allows the overtake of the density current over the less dense ambient fluid. Apart from viscous effects, the turbulence in the flow surroundings and the movement relatively to ambient fluid generates a strong modification on the head profile.

The current head is characterized by a three-dimensional flow, being related to two dominant modes of instability which govern the mixing processes: Kelvin-Helmholtz instability and lobes and clefts (Simpson, 1982), as shown in Figure 2.3. Kelvin-Helmholtz billows are generated in the interfacial region, at the rear of the current head, and roll up as the current advances. They remain quasi-steadily in the current body, fading away due to the entrainment with the surrounding fluid. Lobes and clefts are generated by a convective instability formed at the foremost region of the head, caused by the incorporation of less dense fluid by the current head during its propagation along a no-slip lower boundary (Simpson, 1982). According to the initiation mechanisms and supply, the flow in the body region can be classified as unsteady or steady (or quasi-steady). In currents generated by instantaneous, or short-duration, release of heavy fluid, the body is typically unsteady where the characteristic variables are both space and time dependent. In continuously fed density currents, the constant supply of denser fluid balances the density reduction of the current due to mixing with the surrounding fluid, leading to quasi-steady flow in the body region, where the characteristic variables have small variations in time (Isabel & Nogueira, 2013).

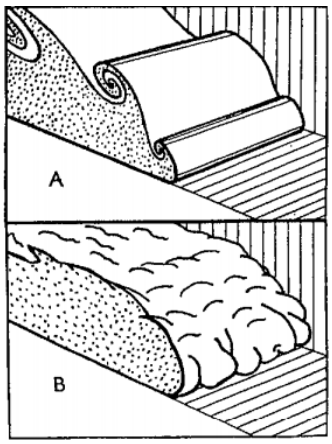

Figure 2.3: Instabilities modes at the density current front: (a) Kelvin-Helmholtz billows; (b) lobes and clefts (Simpson, 1982).

The present study will focus heavily on density currents produced by the lock-exchange technique, Figure 2.4. These density currents over a smooth bed can present two, or even three, distinct phases: slumping phase, self-similar phase, and viscous phase ((Huppert & Simpson, 1980), (Rottman & Simpson, 1983)).

According to (Huppert & Simpson, 1980) the slumping phase occurs after the instantaneous release, where an initial adjustment phase is observed during which the front position varies linearly with time and the front advances with approximately constant velocity.

In the case of lock-exchange experiments, when the flow is confined within a channel of limited length, the initial constant-velocity phase merges into a second phase called self-similar phase, when a bore generated at the end wall of the channel overtakes the front (Rottman & Simpson, 1983). From this instant, the front position advances as $t^{2/3}$, with front speed decreasing as $t^{-1/3}$, t being the time after the gate removal. In both slumping and self-similar phases, the current development is governed by the balance between buoyancy and inertial forces.

Eventually a third phase know as viscous phase develops when viscous effects overcome inertial effects and the current front velocity decreases more rapidly (as $t^{-4/5}$, with front position advancing as $t^{1/5}$).

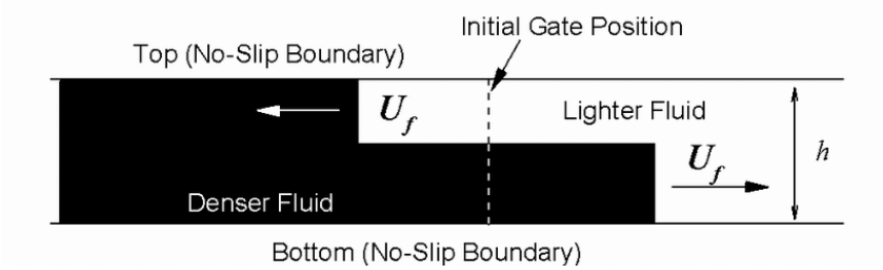

Figure 2.4: Example of the lock exchange technique.

2.3 Characterization

To characterize the density currents, it is important to start with the term of reduced gravity which refers to the force produced by the density difference between the two fluids (Ungarish, 2009), that can be expressed as:

$$g' = g\frac{\Delta\rho}{\rho_0} \tag{2.1}$$

where $\Delta\rho$ is the average density difference, ρ_0 is the density of the less dense fluid and g is the gravitational acceleration.

Another parameter it is the current speed, u_0, which is driven by a reduced gravity g' and the fluid depth, h_0. It can be expressed as:

$$u_0 = \sqrt{g' h_0} \tag{2.2}$$

The Reynolds number, Re, is a fundamental parameter to characterize density currents that is defined as a dimensionless ratio measuring the degree of viscous dissipation on the density current. In the expression, u_f is the mean velocity, h_o is the fluid depth and v is the kinematic viscosity of the current fluid (Adduce et al., 2012), expressed as:

$$Re = \frac{1}{2} \frac{u_f h_o}{\nu} \tag{2.3}$$

The viscous effects are neglectable when Reynolds values are greater than 1000 (Simpson,1982).

The density currents can also be characterized by their behaviour, and in that sense the densimetric Froude number, Fr, is the ratio of the flow inertia to the reduced gravitational force. Basically, it is a dimensionless representation of the speed of the flow, expressing the relation between the speed of the density current, u_0, and the speed of a long wave propagating along the interface of both fluids, u_f. It is given by the equation:

$$Fr = \frac{u_f}{\sqrt{g' h_0}} \tag{2.4}$$

2.4 Interaction of density currents with buff obstacules

The present works studies the interaction of a density current with an isolated circular cylinder and with an array of in-line cylinders.

Regarding interactions with vertical cylinder, (Mok et al., 2011) states the entire process can be divided into three stages: The impact stage, transition stage and quasi-steady stage. The impact stage is characterized by the first run up stage of the saline current hitting the cylinder wall which can be related to the inertia of the incident current, while the transition stage is the second run up stage which is affected by the development of the reverse flow of the less dense current around the cylinder and up the saline current. It is important to refer that the maximum run up occurs in the transition stage. Finally, the quasi-steady stage is generated by a weak internal jump reflected from the cylinder and starts after the saline current rundown on the cylinder wall reaches its minimum. During this stage, the density current head passes the cylinder, and the saline fluid behaves like a quasi-steady stream with a constant mean depth.

A representation of the impact stage and the transition stage is shown in Figure 2.5.

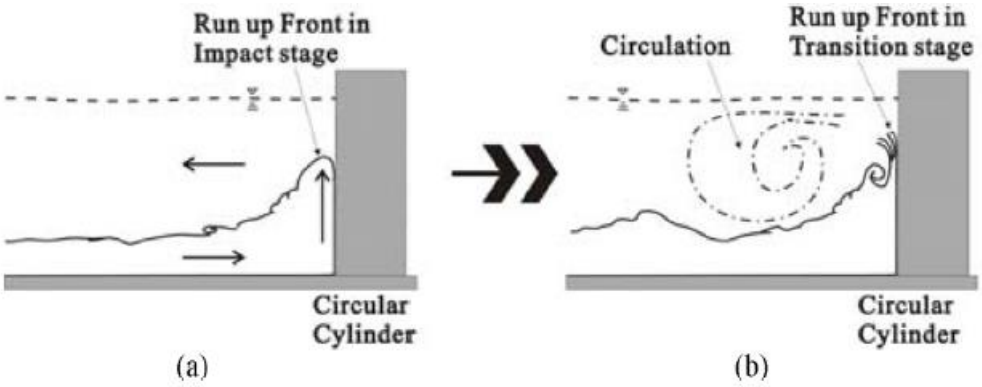

Figure 2.5: Stages of interaction between density current and a vertical cylinder: (a) impact stage ; (b) transition stage. Adapted from (Mok et al., 2011).

Regarding the interaction of density currents with an array of emerged cylinders some studies have been taken ((Tanino et al., 2005); (Zhang & Nepf, 2008); (Ozan et al., 2015)) and regarding the vortex generation of the fluid by the presence of the cylinders in certain configurations, (Sumner, 2010) has made a compilation of the studies on the experimental and numeric fields over the last decades.

The flow patterns around the array of cylinders have a strong influence by the wake and proximity effects, which are mainly determined by the longitudinal and transverse spacing between the cylinders, as shown in Figure 2.6. Other factor such as the Reynolds number, aerodynamic forces and vortex shedding have also a strong impact on the flow pattern around the cylinders. (Sumner, 2010).

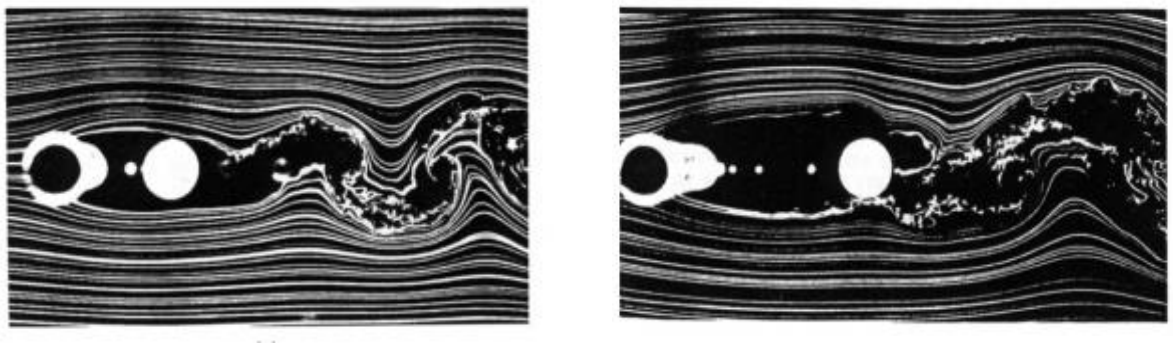

(a) (b)

Figure 2.6: Flow past two tandem circular cylinders ; (a) L/D=2 ; (b) L/D=4, Adapted from (Ljungkrona & Sundén, 1993).

2.5 Experimental studies of density currents

The second half of the XX century marks the beginning of the studies on density currents throughout experimental and theoretical works.

As previously mentioned, in this thesis were employed two different techniques of analysis for the density currents, the PIV (Particle Image Velocimetry) and the image analysis technique form high speed video recording.

Regarding the use of the high-speed image technique analysis, normally are used dyes or tracing particles so the technique can be effective. Most recently some authors such as Adduce et al.(2012) and Nogueira et al. (2014), have studied the density distribution within the density current using a food dye called rhodamine, which will be used in the second part of the laboratory experiments in this thesis. The high-speed image technique is appropriate to study the mixing processes and the entrainment of the current (Ellison & Turner, 1959), (Parker et al., 1987) and Cenedese & Adduce (2010).

The other laboratory technique that was used in the experiments it is the PIV, where tracing particles are applied in both fluids so the inner velocity of density currents can be studied.

This technique has been widely used since the beginning of the 21st century and there are some interesting articles that employ the PIV technique in density currents such as Thomas et al. (2003) and Zhu, (2006).

3 Description of experimental tests

3.1 Introduction

The present chapter provides the details for the experiments performed to assess the velocity fields and the mass distribution of density currents propagating in a confined open channel with the presence of the array of cylinders. This experimental research was carried out at the Fluid Mechanics Laboratory of Nova School of Science and Technology.

3.2 Experimental facility description

The experimental tests were performed in a 3 m long, 40 cm high and 17.4 cm wide channel, as show in Figure 3.1.

Figure 3.1: Channel where the tests were performed.

For the purpose of the thesis, inside the channel was installed a set up that consists in an array of 93 bulk cylinders fixed in an acrylic plate, as show in Figure 3.2 (a). In the experimental tests prior to this thesis were used different set ups, one without any cylinders and the other with the presence of one cylinder in the first half of the channel. In chapter 5 will be discussed some results where those configurations were used.

Regarding the array configuration, it consists in 31 lines of three bulk cylinders side by side in the second half of the channel. The cylinders have a diameter of 2 cm, were separated 2.5 cm from each other and each line distant 2.5 cm from another, Figure 3.2 (a).

The channel was divided in two parts. The first part called lock was the place where the denser fluid was filled in the channel, with a volume of $0.30 \times 0.174 \times 0.20\ m^3$. The second part was the place where the lighter fluid was filled, with a volume of $2.7 \times 0.174 \times 0.20\ m^3$. In all tests the height of the fluids was kept at 0.2 m.

Figure 3.2 (b) shows a view of the array of cylinders with the ambient fluid.

(a)

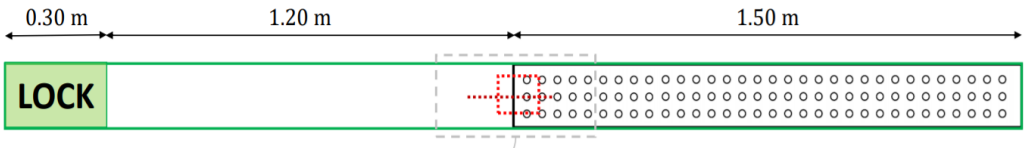

(b)

Figure 3.2: (a) Plan view representation of tests configuration (b) view of the array of cylinders.

The gate used in channel was a thin, small sheet of steel metal with a height of 40 cm, 17.4 cm width and 1 mm thickness, located 30 cm from the left end of the channel, as shown in Figure 3.3. When the lock gate is being released, it can create a small oscillation of the water surface due to its thickness and the physical vertical motion of the lock itself, so to minimize this effect the lock was removed the fastest way possible in the vertical. Attached to the gate was inserted a trigger mechanism to detect the exact instant the gate was removed.

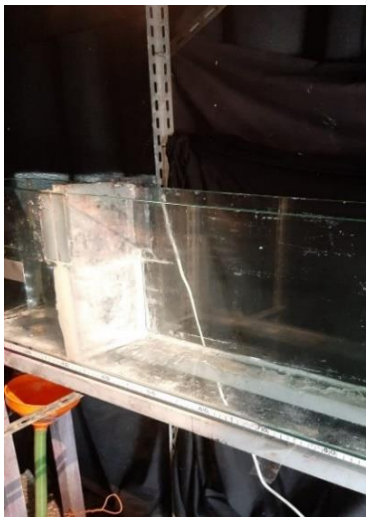

Figure 3.3: Gate placed in the channel.

The channel was supported by a steel frame structure, which consist of a rectangular section with the same dimensions as the plane of the channel. Six steel hollow legs with a height of 90 cm ran down from this structure to support the channel, keeping the tank horizontal for the duration of the experiments. It was placed a 300 cm ruler along the bottom side of the channel in the field of view of the camera.

Two LED panels were installed in the channel behind the glass. Six movable bars with a L shape were placed in the gap bellow the channel and the steel structure to accommodate the panels. In Figure 3.4 is shown one LED panel.

Figure 3.4: LED panel.

For the PIV tests it was needed black curtains around the structure, as show in Figure 3.5, that supported the laser and the camera because the brightness exposure of the environment can affect the lighting of the experiment, which may compromise the quality of the images and negatively influence the PIV test. The curtains were needed to create dark conditions, which was important to keep the conditions of the experiment constant over time.

Figure 3.5: Experimetal set-up of PIV tests cover with black curtains.

3.3 Experimental apparatus

To have a better understanding on the dynamics of the density currents were made two types of tests, first using the PIV technique, and afterwards using the image analysis technique. The density currents were created experimentally using the lock-exchange technique.

3.3.1 Experimental procedures

Despite using two different techniques for obtaining the density currents, there are some experimental procedures that were the same, or very similar, all over the tests and that will be described by order below:

i. First was very important to keep the channel clean (cleaning the channel glass, the cylinders, remove parts of vaseline who were loose).

ii. Make sure the contact zones between the lock gate and the tank walls were sealed with vaseline to avoid fluid leaking between channel sections.

iii. Prepare the salt mixture and alcohol mixture with the quantities required to reach the target reduced gravity.

iv. Fill the channel, with the denser fluid in the lock area and the ambient fluid in the bigger compartment. While filling the channel was important to keep the different fluids at the same height to maintain the hydrostatic pressure in the lock balanced.

v. After both fluids reach the 20 cm mark was necessary to determine their density in different regions of the channel using the pycnometers.

vi. Measure the water temperature using two digital thermometers, one in the denser fluid and the other in the lighter fluid. To facilitate the measurements the thermometers were placed near the lock gate.

vii. Then was important to turn off the lights and make a dark environment in the lab for the image recording.

viii. Finally proceed to remove the lock on a fast and fluid way to minimize the fluid perturbation in the channel.

In Table 3.1 is given the type of test made during the experiments, the measured plan, the target reduced gravity for the currents in each test and the number of repetitions performed.

Table 3.1: General overview of the experimetal tests performed

Type of test	Type of plane measured	Target reduced gravity (m/s^2)	Number of repetitions
PIV	Side view	0.36	10
		0.09	10
	Plan view	0.09	20
Image analysis technique	Side view (First half of the channel)	0.36	10
		0.09	10
	Side view (Second half of the channel)	0.36	10
		0.09	10

Regard the PIV test were made two types of measurements, one it is the side view where the recording camera was placed on the side of the channel, perpendicular to the glass, while the laser was on top of the channel. The other was the plan view where the camera was placed on top of the channel and the laser was on the side, perpendicular to the glass.

On the side view 20 repetitions were made in total with two distinct values of target reduced gravity for the currents, 10 repetitions with 0.36 m/s^2 and 10 with 0.09 m/s^2.

On the plan view were made 20 repetitions with the same reduced gravity, 0.09 m/s^2. With the 0.36 m/s^2 current the amount of alcohol in the channel was too high and the images recorded get poor quality, so instead the 20 repetitions were made in a different way with the plane being measured in two different heights, 10 repetitions with 1.6 cm and the other 10 repetitions at 8 cm heigh.

After the PIV test, were made repetitions using the image analysis technique. In this case were made repetitions in the side view but with the camera in different positions to see the current near the lock position, capture the channel from 0 to1.55 meters and within the array of cylinders, capturing the channel from 1.41 to 3 meters.

For each camera position were made 20 repetitions, 10 repetitions with the reduced gravity at 0.36 m/s^2 and 10 at 0.09 m/s^2, so in total with the image analysis technique were made 40 repetitions.

3.3.2 Refractive index matching and density measurements

In this experiment an important factor for the quality of the images acquired is to have a matched refractive index. After the release of the gate the denser fluid propagates near the bottom of the channel, while the lighter fluid moves over the dense one in the opposite way. The channel becomes a stratified environment in which a bottom boundary density current propagates under a top bottom boundary current with different density.

At the interface of the fluids, mixing process occurs due to turbulence and when light and the laser beam passes through the fluids interface area, the difference in density affects the speed of propagation and modify the direction of the light.

According to (Daviero et al., 2001) the amount of salt and alcohol needed can be interpolated from a function to have the same refractive index, as the density and refractive index vary linearly with the solute concentrations, both for salt and alcohol solutions.

To reach a current with $0.09\ \mathrm{m}/s^2$ reduced gravity it was needed 92 grams of salt and 2.26 liters of alcohol. To reach a current with $0.36\ \mathrm{m}/s^2$ reduced gravity it was needed 385 grams of salt and 8.89 liters of alcohol. These quantities suffer a few changes throughout the months of the experimental work due to the impact of temperature variation in the fluids that changed the density and consequently the reduced gravity.

The salt quantities were measured using a digital scale and the alcohol was filled into marked bidons as shown in Figure 3.6 (a).

(a) (b)

Figure 3.6: Measurements: (a) alcohol measurement with bidon; (b) salt measurement with digital scale.

The density measurements of the mixtures were performed through the pycnometer method after the channel was filled with water. As shown in the Figure 3.7, a pycnometer is a glass flask with a close-fitting ground glass stoper with a capillary hole through it.

It was only necessary one measure of the salt mixture density but three for the alcohol mixture because a large portion of the channel contain this kind of mixture and was necessary to check the uniformity of the mixture along the channel. By measuring the mass of fluid inside the pycnometer with a precision scale the density of the fluids could be determined with a reduced error.

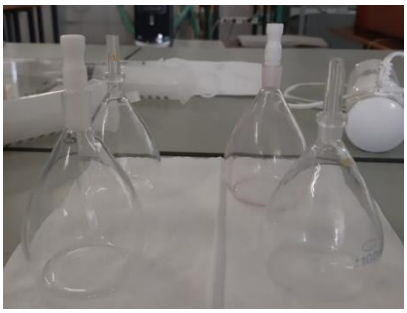

Figure 3.7: Pycnometers.

Before taking the densities, it was necessary to determine the volume of the several pycnometers. The pycnometer´s were weighted to check their mass and then, filled with distilled water at a known temperature were weighted again. The density of distilled water is given as a function of its temperature, so with some computation the volume of pycnometer´s were determined.

The salt density was considered as 3000 kg/m^3 but then the density of salt mixture with water was obtained with the pycnometer technique.

In Table 3.2 is given, as example, the values of measured densities and consequently the reduced gravity obtained for 10 repetitions of a target reduced gravity of 0.09 m/s^2.

Table 3.2: Measured densities and computed reduced gravity for ten repetitions

Repetition	Average alcohol density (kg/m^3)	Salt mixture density (kg/m^3)	Reduced gravity (m/s^2)
1	995.76	1004.6	0.087
2	996.16	1004.9	0.086
3	995.46	1004.9	0.093
4	996.10	1004.8	0.086
5	995.36	1004.8	0.093
6	995.46	1004.8	0.092
7	995.16	1004.7	0.094
8	995.51	1004.8	0.092
9	995.61	1004.7	0.089
10	995.71	1004.9	0.090

Since was very difficult to achieve the round value of 0.09 were considered valid repetitions the ones with a maximum error of 5% from the target value in the range of [0.085-0.0945].

3.3.3 Tracers used for flow visualization

Regarding the PIV tests, it was decided to use as seeding a material commercialized by Dantec Dynamics®, called Polyamide Seeding Particles (PSP). PSP is a microporous material with density of 1.03 g/cm^3.

As it has a density very similar to the water, when it is placed in moving water it follows the flow without settling or floating on the surface. This seeding is made up of particles produced through a polymerization process with a rounded shape but not exactly spherical. These particles have an average size of 50 µm within a range that varies from 30 to 70 µm and have a refractive index of 1.5 (Ricardo et al., 2013), Figure 3.8 (a).

For the image analysis technique tests was used a food dye to be mixed with the denser salt current called rhodamine, Figure 3.8 (b).

(a) (b)

Figure 3.8: (a) Polyamide Seeding Particles; (b) Bidon full of rhodamine.

3.4 PIV tests

3.4.1 Introduction and measuring principle

The PIV technique will be performed to determine the 2D velocity field measurements and the turbulent structures of the current head and tail.

This technique consists in introducing into the flowing fluid small diameter tracer particles, which must faithfully follow the flow. The measurement zone is illuminated with a laser sheet, and the images are captured by a camera located in an orthogonal position to the test section. Two images are acquired in a short time interval and stored in the computer.

The stored images are divided into small areas, called interrogation windows, which are treated by statistical methods (cross-correlation) to determine the particle displacement and hence the velocity field (Raffel et al., 2007).

By applying post-processing algorithms, the velocity field is analysed to identify the possible presence of spurious vectors that can be obtained in regions with low visibility or lack of particles. These vectors, which are expected to be negligible in number, are eliminated at this stage and replaced by interpolated vectors. In the post-processing stage, the velocity field is filtered to attenuate the presence of noise.

The quality of the acquired data, and consequently the results, depends fundamentally on three interrelated parameters: the time between two consecutive pulses (Δt), the seeding quantity and the size of the interrogation area. The time interval between pulses, Δt, should be small enough so that the particles recorded in the first image do not disappear in the transition to the second image (Raffel et al., 2007). However, for larger Δt the displacements recorded will be bigger and consequently a better accuracy of the results. Values of Δt too small or too high can lead to the skew of the instantaneous velocity. This problem is called as bias to zero (Raffel et al., 2007).

The skewness of the velocity values when Δt is too high corresponding to the problem of loss of pairs. When Δt is too small, the sub-pixel interpolation algorithm may lose accuracy and indicate zero offsets.

The size of the interrogation area is related to the value of the time interval between pulses and depends at the number of particles captured in each image. There is a common rule in which it´s intended that there are 12 seeding particles in each interrogation area and that the displacement of these particles is not greater than 25% on the side of the interrogation area (Raffel et al., 2007).

When small interrogation areas are used it is necessary to introduce in the flow high quantities of seeding whose particles should be of small dimensions. On the other hand, small interrogation areas are associated with large displacements of the seeding particles. If the displacements are too large, the seeding particles who started their displacement near the boundaries of the interrogation area may end their journey outside this area and consequently decreases the velocity bias to lower values. To minimize this problem, it is common to overlap the areas of interrogation around 25% to 75%. This way, it is ensured the maximization of the number of seeding particles used in the calculation of velocity vectors. The overlapping does not improve the quality of the results within each interrogation area, but it does improve the average quality of the instantaneous velocity maps and their resolution.

The instantaneous velocity vector is an average vector in space corresponding to the interrogation area in which it was obtained. The larger the interrogation area, the lower the spatial accuracy of the instantaneous velocity vector. The problem is greater the more complex the flow is and the more foreshortened the velocity gradients within the interrogation area are. To minimize this problem, it is usual to run the correlation algorithm iteratively over successively smaller interrogation areas.

The trend of the movement is saved between every two steps and used to eliminate errors in the correlation algorithm noticeable by leading to displacements apparently against the trend of the movement.

In this way, the choice of the size of the interrogation areas involves a compromise between the detail that is intended for turbulent structures, which is greater the smaller the interrogation, and the amount of seeding that needs to be added to the flow, which will be higher the smaller the interrogation area is (Raffel et al., 2007).

3.4.2 Components and data collection

The PIV system, already explained above, consists of the following components, shown in Figure 3.9.

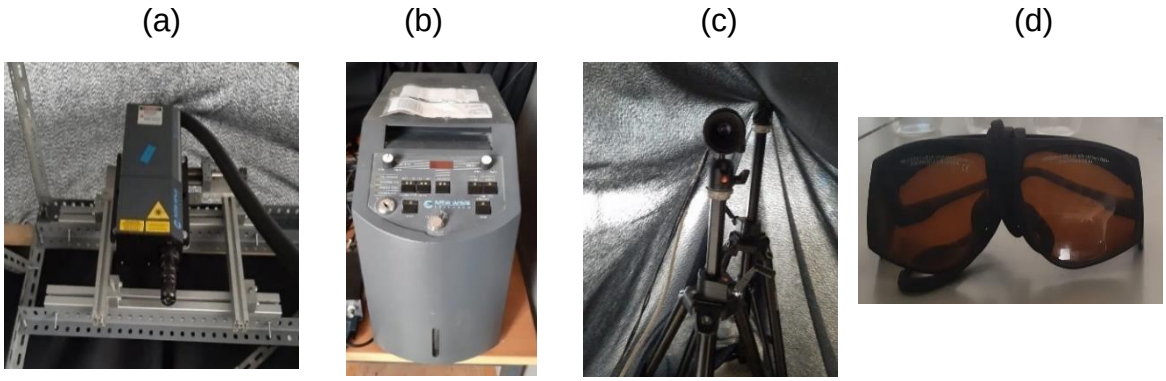

Figure 3.9: PIV components; (a) Laser head; (b) Laser beam generator; (c) Digital camera (d) Glasses.

An example of how PIV components are interconnected is shown in Figure 3.10 (Silvestre, 2016).

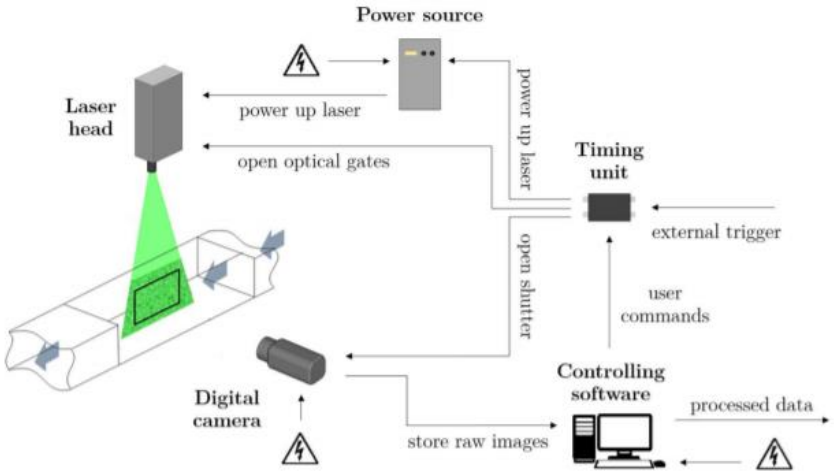

Figure 3.10: PIV components assembler; Adapted from (Silvestre, 2016).

The laser head was placed vertically or horizontally on a support depending on the field of view that is being analysed. The laser is of the type Nd:YAG (YAG crystal - Yittrium Aluminium Garnet - infiltrated with Neodymium ions) and emits a beam of light that illuminates a given section.

The laser head has an optical system which directs the light beam to the section to be illuminated by manual alignment. The laser, with a double cavity, allows the emission of radiation by pulses and the time interval between two consecutive pulses it is controlled by the user. (Ferreira, 2011)

The light emitted by the laser is mainly in the infrared range (IR), which is not suitable for making measurements because wavelengths in this range are not detected by cameras or the human eye. However, the laser head has a system that converts light in the infrared range into visible light with a wavelength of 532 nm (green colour) (Smith & Neal, 2016).

Regarding the hazard of the emitted radiation, the laser is considered as class four which is the most dangerous and therefore the operator must wear protective eyewear with green light filters. The entrance to the laboratory should also be restricted during the operation of the laser and correctly signposted to prevent any problem.

It is in the PIV generator that the laser beam is generated and controlled. The laser can be operated in two different modes: the external mode where it is controlled by the acquisition software or the internal mode where it is controlled directly by the user.

The software that controlled the laser properties and performed the data acquisition and data processing was DynamicStudio. Regarding the laser properties, the software defines the time between two consecutive pulses and the frequency of the impulses. For data analysis, the variables that can be controlled are the type of correlation, the size of the interrogation area and the data validation method.

The synchronism between the PIV system and the lock was performed using an external trigger controlled using DynamicStudio..The trigger allows to define the time delay between the remove of the lock and the beginning of the data acquisition by the PIV system (Brito et al., 2017).

The digital camera films the section illuminated by the light beam emitted by the laser, recording the position of the transported particles in suspension in the flow. The camera was installed perpendicular to the plane of the channel glasses for the measurements of vertical 2D velocity fields. For the measurements of horizontal 2D velocity fields was installed at the top of the channel.

Figure 3.11 shows an example of an image captured by the camera, where the particles can be identified as bright spots on a black background. As the illuminated particles are interpreted as shades of grey it´s very important that the brightness in the laboratory is kept to a minimum, as that it may reduce the contrast and negatively influence the quality of the images acquired.

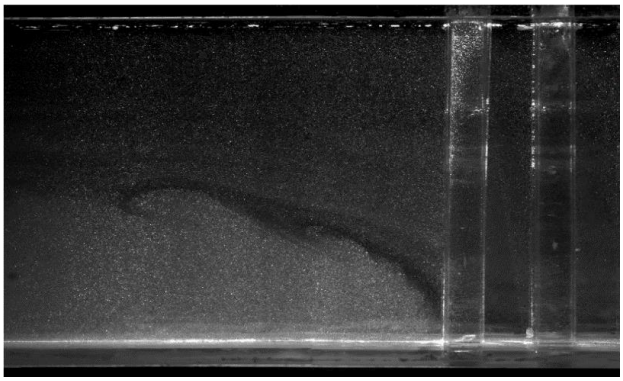

Figure 3.11: Image capture by the CCD camera where are visible the first 2 row of cylinders and seeding particles.

Another difficulty of using the PIV technique to measure the velocity field of the density currents is matching the refractive index of fluids. If they do not match, the direction of the incident laser sheet is deviated when crossing the interface of both fluids, causing blurry images due to difficulties in distinguish the seeding particles, as shown in Figure 3.12. The seeding particles between the cylinders are blurred due to bad matching.

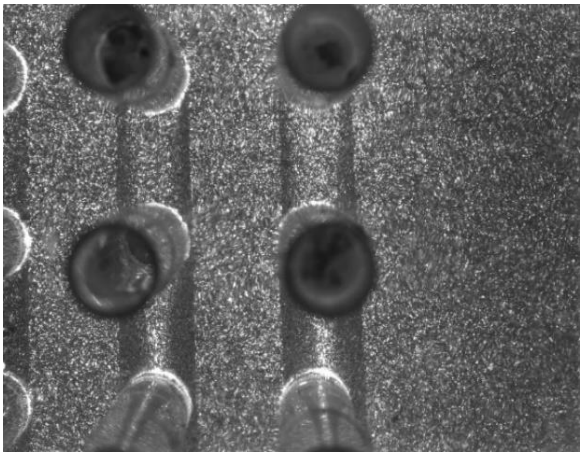

Figure 3.12: Example of blured image due to poor refractive index.

3.4.3 Data analysis

After collecting the data in DynamicStudio was necessary to take the first steps to start processing the Data.

In the experiments, before removing the lock gate, was necessary to put in the channel near the cylinders the calibration plates as show in Figure 3.13. Their function is to convert into SI units the displacement of the seeding particles because both plates have a grid with some numbers that give a dimension in centimetres. Another function is to facilitate the camera focus. On the left is illustrated the calibration plate for the side view while on the right is the plate for the plan view.

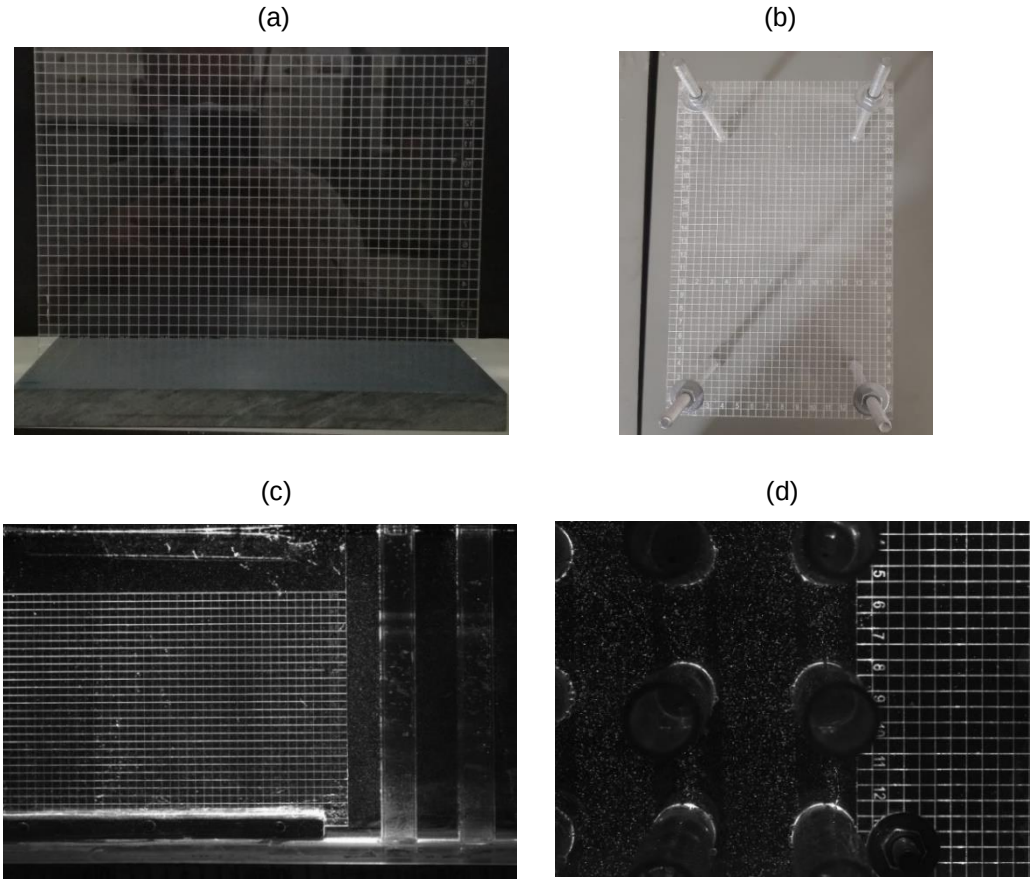

Figure 3.13: Calibration plates; (a) Side view calibration plate; (b) Plan view calibration plate (c) side view calibration plate in the channel; (d) plan view calibration plate in the channel.

After taking the pictures and with the auxiliary of MATLAB codes, the calibration process was made by inserting a minimum of 4 lines in the image area where the calibration plate is. Each of those lines give a certain value that is supposed to be the same between them and in that way a factor of calibration is calculated. With the calibration factor and after some computation in the MATLAB, the coordinates in the *x* and *y* direction are converted in meters.

In the same code where the calibration factor is obtained it was also made the masking process of the images with the cylinders. This process is important to remove some unnecessary parts in the images that could latter interfere with the results. It consists in masking the free surface limit, the plate limit, and the cylinders part in the side view. For the plan view was necessary masking the cylinders shape by making close polygons with a MATLAB function.

In Figure 3.14 is shown an example of the masking result in an image of the plan view, where it is visible six white shapes that correspond to the masked cylinders.

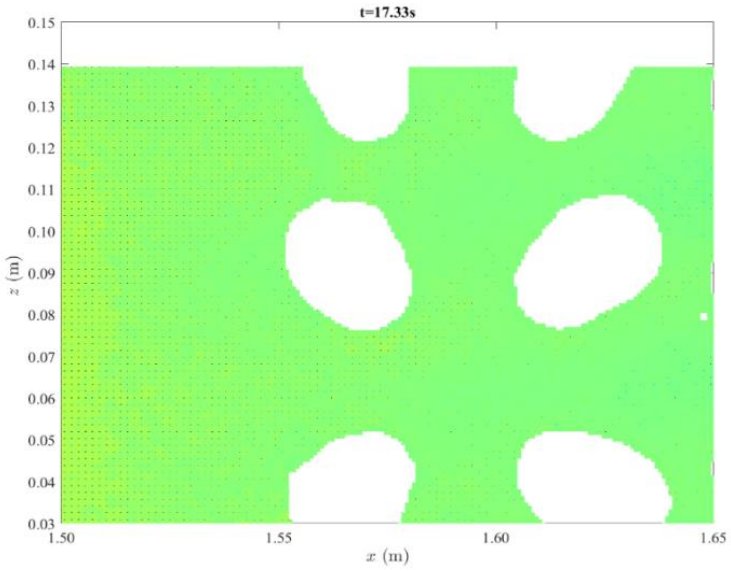

Figure 3.14: Image resulting from the masking process in the plan view.

Regarding the data analysis for the PIV is also important to refer the images were taken at a frequency of 15 Hz, and the interrogation area chosen for the analyses had a size of 16×16.

3.5 Image analysis technique from high-speed video recording

3.5.1 Introduction

In this section is described the methodologies and apparatus used to assess the mass distribution of the current. The high-speed video recording was used to analyse the transport and mixing processes of the current within the array of cylinder. It was added to the solution of water and NaCl a dye (Rhodamine), so the current could be distinguished from the ambient fluid.

The first step is doing the calibration process where the correlation of the lightning intensity and the density of mixture will be discovered. For a proper calibration process, it was used the pixel-by pixel method to get the mass distribution maps.

The camera used for this type of tests it´s an Allied Bonito CL-400B/C high speed camera, Figure 3.15, with a considerable high-definition image quality. The camera has a frontal section of 800x70 mm^2 and a width of 35 mm. On the back it has three entrances, being used for the power supply and the transmission of the data to the computer.

Figure 3.15: High speed camera Allied Bonito CL-400B/C.

The video camera recording software implemented in the test was the StreamPix5, which is an application designed to provide the images been captured by the camera to the PC memory or hard disk. The StreamPix native files format is the “. seq” for sequence files and the images are stored in their raw format, incurring no quality loss. The selected extension for the images of the experiment were in “bmp” format.

In the following figures is shown what the camera records and appears on StreamPix, being the Figure 3.16 (a) the lock view where is possible to see on the left side the denser fluid in a darker level and the Figure 3.16 (b) the array view where is possible to see the array of cylinders in the second half of the channel.

(a)

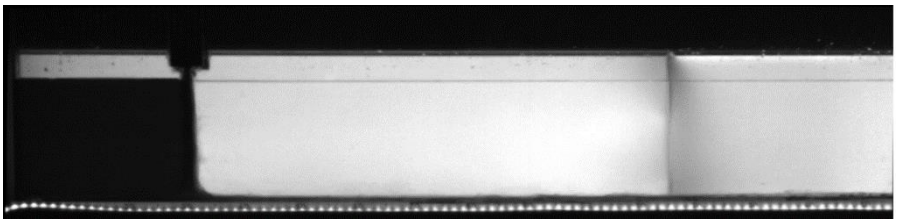

(b)

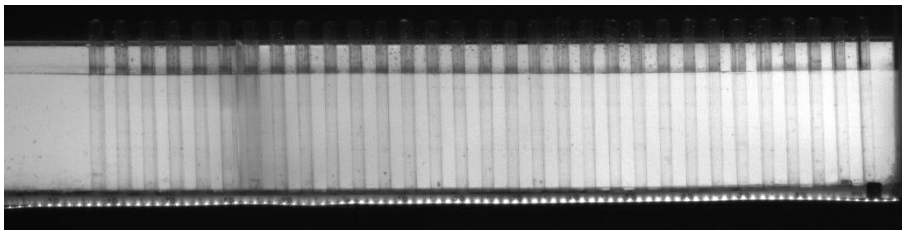

Figure 3.16: StreamPix views: (a) lock view; (b) array of cylinders view.

3.5.2 Calibration procedure

The color range of the experience allows to identify for each point during the experiment the correspondent density. The camera operates in a greyscale color range, which is influenced by the exposure time of the camera, the used concentration of rhodamine and the aperture of the lens.

The perfect greyscale, showed in Figure 3.17, as a range that goes from 0 to 255, where 0 it is the dark shade of black and 255 it is the lightest white. It is important to refer that those limits are impossible to reach. The lower one because the rhodamine even if added in large quantities to water will never present a shade of black but instead a dark red. The highest limit of 255 because if the ambient fluid would get that value, it wouldn´t be possible to change that even if the color become brighter.

Figure 3.17: RGB scale; extracted from (Gabriel,2018).

As was shown in section 3.1, for this type of tests the camera was recording the first half of the channel for two currents, seeing the lock, and another two currents seeing the second half of the channel with the array. Every time the camera moved position was necessary to do another calibration because the conditions of recording vary, and since there are two different values for a target reduced gravity, it was necessary to do 2 calibrations for each camera position because the range on density values for RGB would be considerable. So, in total 4 calibrations were made.

The first step of the calibration was filling the entire channel with the salt mixture quantities used for the density current being studied. The solution was prepared in bottles with a capacity of 20 liters to assure the mixture was good before going to the channel.

Afterwards when the channel was filled until the reference heigh of 20 cm, a measured quantity of rhodamine was added to the channel to reach the darkest shade possible. In the first calibration the amount of rhodamine put in the channel was 137.4 grams, but this quantity was found excessive because there were some difficulties in the dilution. In the fourth and last calibration were added only 44.97 grams of rhodamine which made the process easier.

Then it started the dilution of the mixture inside the channel by adding alcohol with water. After each dilution step, a sequence of photos was taken in which was possible to verify the level of grey recorded by the camera. In Figure 3.18 is shown a sequence of partial images from where is possible to see the difference between steps.

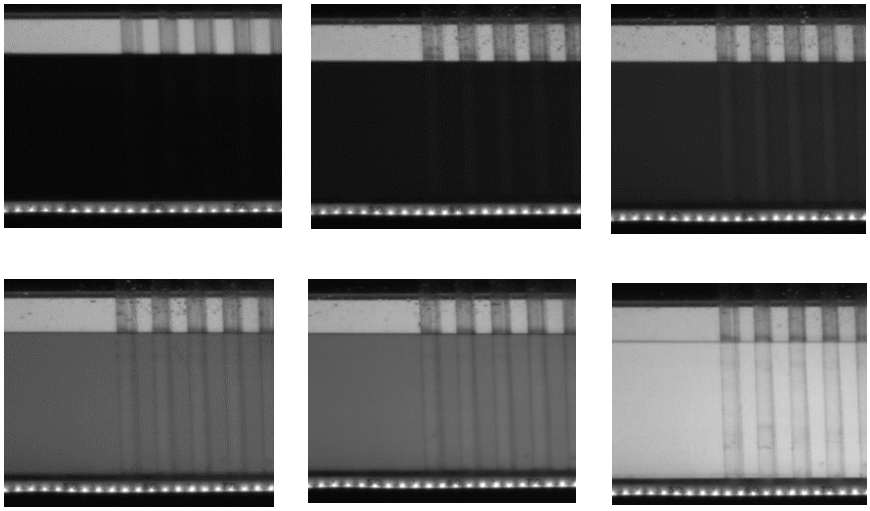

Figure 3.18: Sequence of calibration steps.

To have a clear view in what the human eye could see during the calibration process, is presented a sequence of images of the channel taken by another camera in Figure 3.19, where is possible to see the real colours of the mixtures after some dilution steps. The first image where the mixture is red, (a) is one of the first steps after the rhodamine is placed in the channel, then after some dilutions the mixture get a dark pink tonality (b), and finally in last steps the mixture gets a light pink (c).

(a) (b) (c)

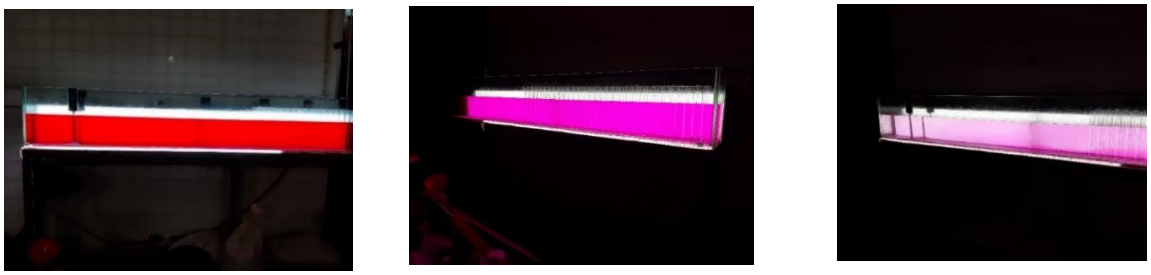

Figure 3.19: Calibration process sequence: (a) red mixture; (b) dark pink tonality; (c) light pink mixture.

The information of a calibration for a density current of 0.36 m/s^2 is presented in the Table 3.3 which includes the density inside the channel and the level of grey in a chosen pixel for each step.

Table 3.3: Calibration information for 0.36 m/s^2 current.

Step	Density in the channel (kg/m^3)	Grey color [RGB]
1	1022.45	21
2	1010.08	28
3	1002.00	34
4	997.02	42
5	993.10	49
6	991.14	60
7	989.74	68
8	987.65	82
9	986.93	94
10	985.71	136
11	985.41	156
12	985.21	183
13	985.30	254

In Figure 3.20 is shown the calibration curve related to the values of Table 3.3, where the RGB levels are plotted in function of the measured density.

Using the MATLAB codes was possible to determine the multiple calibration curves for all the pixels recorded which will be fundamental in the data treatment analysis in the next chapter.

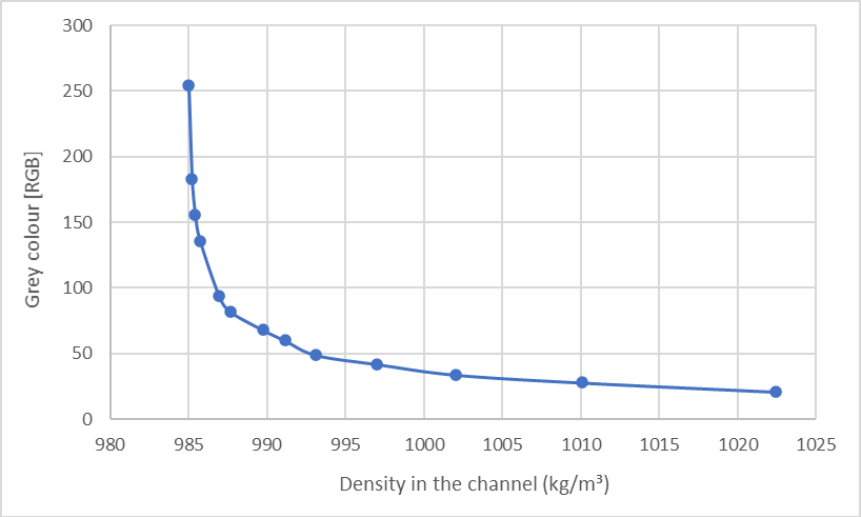

Figure 3.20: Calibration curve for the 0.36 m/s^2 current.

Table 3.4 lists the information for one of the calibrations made for the 0.09 m/s^2 density current.

Table 3.4: Calibration information for 0.09 m/s^2 current.

Step	Density in the channel (Kg/m^3)	Grey colour [RGB]
1	1004.50	21
2	1001.51	23
3	999.51	27
4	998.81	31
5	997.22	36
6	996.52	44
7	996.52	51
8	996.32	62
9	996.12	69
10	995.82	81
11	995.72	101
12	995.52	106
13	995.30	251

In Figure 3.21 is shown the calibration curve for the chosen pixel regarding the calibration information of the table above.

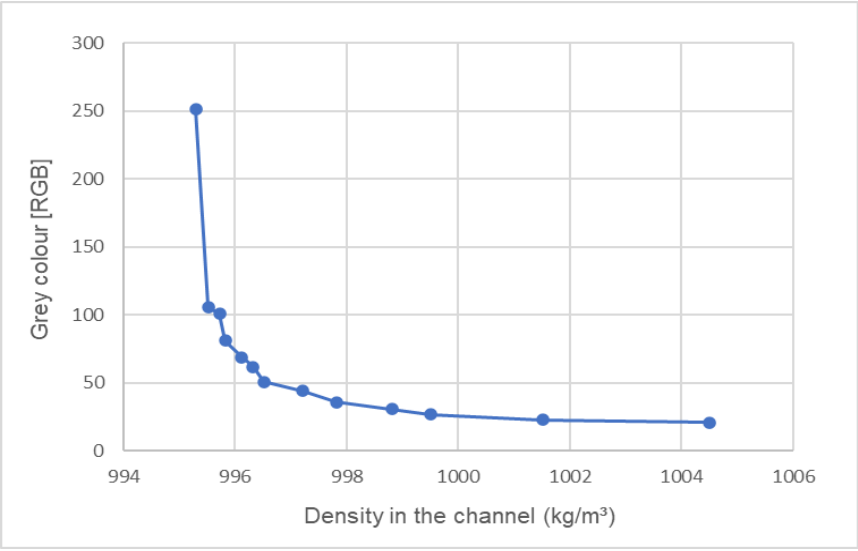

Figure 3.21: Calibration curve for the 0.09 m/s^2 current.

3.5.3 Geometric calibration

Besides the grey scale calibration explained in the section before, it is also necessary to do a geometric calibration. When the camera took pictures, the light from a three-dimensional environment was focused and captured into a two-dimensional image plane, which reduces the dimension of the data taken by the camera from 3D to 2D. Each pixel on the image plane will correspond to a part of light from the three-dimensional world so the MATLAB code determines the association between the incoming light and each pixel on the resulting image.

With the geometric calibration is possible to determine the camera parameters that are the distortion coefficients, extrinsic parameters, and intrinsic parameters. These parameters are used to correct the lens distortion and can determine the camera position in the environment.

The calibration algorithm calculates a camera matrix using the extrinsic and intrinsic parameters. The extrinsic parameters consist of a rigid transformation from the 3D world coordinate system to the camera 3D coordinates system. The intrinsic parameters represent the projection transformation from the camera 3D coordinate into the 2D image coordinates

The camera matrix does not account for lens distortion because an ideal pinhole camera does not have a lens. To accurately represent a real camera, the camera model includes the radial and tangential lens distortion.

A radial distortion occurs when the light rays bend more near the edges of a lens than they do at its optical centre, Figure 3.22. The smaller the lens, the greater the distortion. The tangential distortion occurs when the lens and the image are not parallel and the tangential distortion coefficients define this type of distortion.

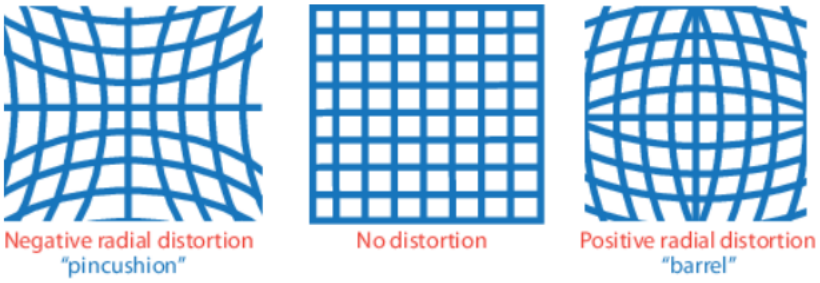

Figure 3.22: Radial distortion effects (extracted from Matlab).

Taking in consideration the distortion of the camera, a checkerboard was placed inside the channel so a MATLAB code for calibration could calculate the camera parameters, as shown in Figure 3.23. Using the StreamPix software, 20 pictures with the checkboard in different positions were taken so the MATLAB code could determine with precision the parameters. Every time the camera switched position was necessary to calculate the new camera parameters.

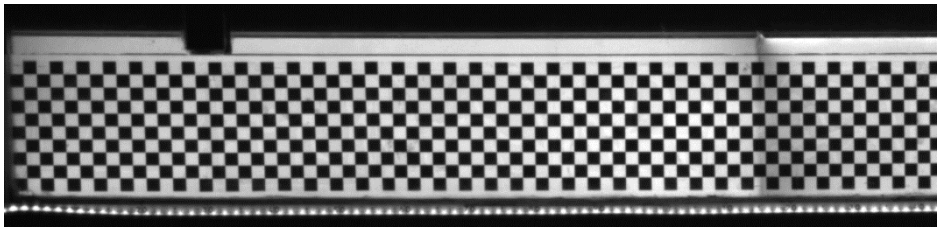

Figure 3.23: Checkerboard placed inside the channel.

3.5.4 Data Analysis

After proceeding with the calibration processes and making the tests was time to start the data analysis. The first step was applying the camera parameters to the calibration images so the distorted images could get undistorted.

After that was crucial to obtain the calibration curves for all the pixels, related to the calibration images, using MATLAB codes.

Then the images related to all tests were also undistorted. It was applied the same process of the calibration images to make them undistorted, an example is shown in Figure 3.24.

(a)

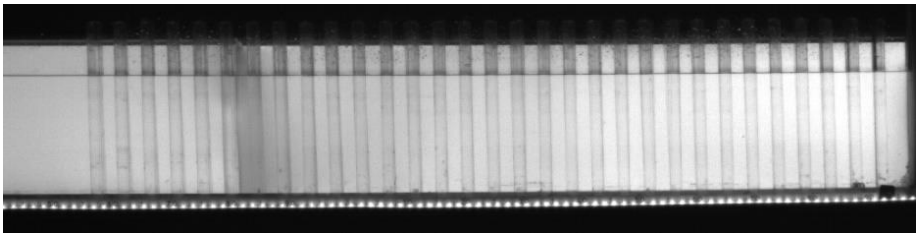

(b)

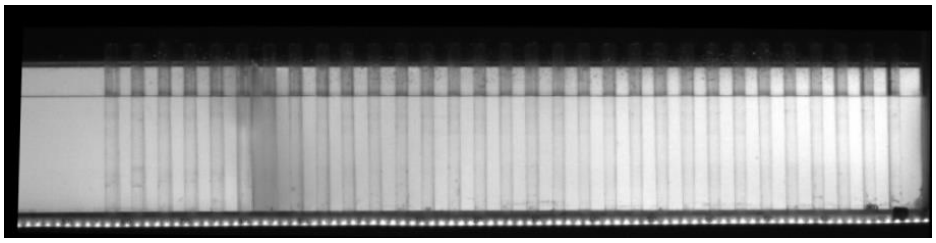

Figure 3.24: (a) Distorted image; (b) Undistorted image.

After all the relevant images were undistorted, the grey levels that the camera recorded for each test were transformed into density values using the calibration curves calculated before. Some relevant information such as the frequency the images were taken, the correspondent image where the lock was removed and the density matrix that kept the information of the density levels for all the images was saved.

It was possible to identify the moment the lock was removed in these tests because the trigger mechanism for this case consists of illuminating the ruler placed along the channel in the exact moment the lock is being released. The frame when the ruler starts showing light correspond to the beginning of the analysis.

The images recorded using this type of technique were taken at a frequency of approximately 42.4 Hz.

In this type of tests was also necessary to convert the pixel coordinates to SI coordinates. The calibration plate in this case was the checkerboard used to obtain the camera parameters because every checker has a dimension of 2x2 cm and with the help of the lightning ruler, the same principle of the lines applied in the PIV calibration process could be applied in the coordinates conversion.

The masking process was also applied but with a different approach. The cylinders were not masked, being the plate limit, the free surface limit, the vaseline area in the lock and the dark parts on the side of the undistorted images the areas being masked.

Finally, the parameters that characterize the density currents and can be studied using these type of tests were computed using MATLAB codes and will be discussed in the next chapter.

4 Density field characteristics

4.1 Introduction

This chapter is dedicated to the presentation of the results regarding tests to measure the density distribution of the currents.

Regarding the tests where the density field characteristics are going to be analysed were made 40 repetitions in total. Those were made with the camera capturing the side view and in two different longitudinal positions, covering approximately half channel as field of view. For each position, 10 repetitions for each tested reduced gravity (0.09 and 0.36 m/s^2) were carried out. The position that covers the range of x = [0, 1.55] m it is called lock view while the position that covers the range of x = [1.42, 3] meters it is called array view.

To have a clear view about the main dimensions and the placement of the array of cylinders, Figure 4.1 shows a schematic 3D view of the channel. The gate is located at $x = 0.30\ m$, the array of cylinders starts at $x \cong 1.56\ m$, the free surface height is located at $z \cong 0.20\ m$ above the bottom and the channel width is $b = 0.174\ m$.

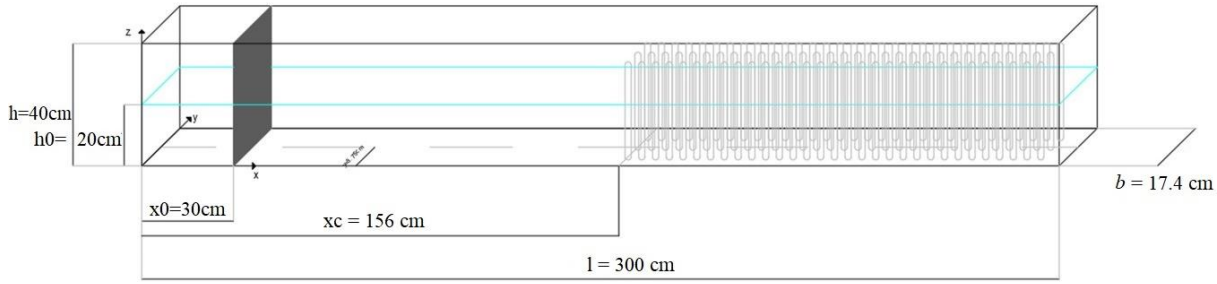

Figure 4.1: 3D view of the channel with the array of cylinders.

To analyse the density field characteristics, the behaviour of the current and to verify if the experimental procedure was correctly performed, several parameters were taken in consideration for the different tests. In this work five parameters, as a function of time and position, are analysed: current density field, the evolution of the current front position, evolution of current height, the conservation of mass in the channel and the current dilution given by the entrainment. The parameters were computed in MATLAB and the main codes employed are presented in the Appendix 1 to 3.

1. Density field

To evaluate the fluids density spatial distribution for each time instant, a conversion from the acquired grey levels to density values is applied by means of the pixel-by-pixel calibration explained at section 3.5.2. The methodology explained was implemented throw a MATLAB script presented in Appendix 1.

2. Current height evolution

The current height can be obtained by determining the interface of the fluids where the concentrations is 0.05. By assigning the maximum ρ_1 and minimum ρ_0 density value to the corresponding maximum concentration value of (1) and minimum concentration value of (0), the concentration can be obtained by the equation below:

$$C(x,y,t)_{i,j} = \frac{\rho_{i,j}(x,y,t) - \rho_0}{\rho_1 - \rho_0} \tag{4.1}$$

where *C* is the concentration and $\rho_{i,j}$ is the density value in each pixel as a function of time.

3. Current front position evolution

The current front is the interface area between the two fluids, located in the nose of the denser current in the head region (Simpson, 1982). To obtain the most advanced point of the current was identified the fluids interface where the concentration was 0.5 in each image of the tests. This value is not universal but was taking in consider based in the available literature and after an analysis it was determined it suited the problem. The computation of the current front position evolution is shown in Appendix 2.

4. Concentration profiles

To better evaluate how the current evolves, concentration vertical profiles for a certain time instant are compared for different longitudinal positions.

5. Dilution parameter (Entrainment)

The dilution parameter, E, widely known as entrainment, measures the amount of ambient fluid entering the dense fluid stream. More precisely, it is defined as the volume increase in the in-stream due to the ingress of ambient fluid (Adduce et al., 2012) :

$$E = \frac{V_i - V_0}{V_0} = \frac{\Delta V_i}{V_0} \tag{4.2}$$

where V_i is the volume of the denser fluid at the $i\ th$ time instant and V_0 is the current initial volume. ΔV_i can be estimated by the following equation:

$$\Delta V_i = (A_i - A_0)b \tag{4.3}$$

where *b* is the channel width, $A_i\ and\ A_0$ are the instant area and the lateral area of the lock ($A_0 = h_0 \times x_0$). A_i is area below the isoline of concentration equal of 0.05, which is given by the literature. (Adduce et al., 2012).

The MATLAB script used to compute the entrainment, current height and mass conservation is presented in Appendix 3.

4.2 Current front features

Figure 4.2 presents the front evolution of the current to the reduced gravity of 0.09 m/s^2 and 0.36 m/s^2 in the lock view. The non-dimensional current front position, x_f^* and time, t^*, are defined as:

$$x_f^* = \frac{x_f - x_0}{x_0} \text{ and } t^* = \frac{t \times u_0}{x_0}.$$

where x_f is the current front position and x_0 is the lock position. t is the time in seconds of the recording analysis, starting in the instant when the lock is removed, and u_0 is the buoyancy velocity.

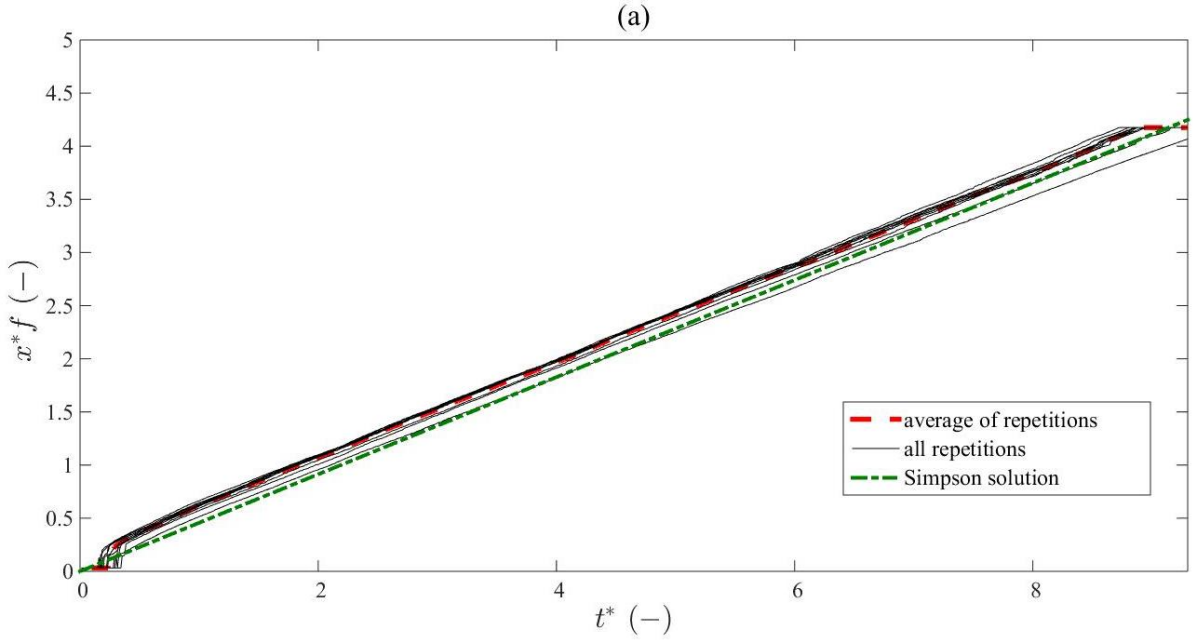

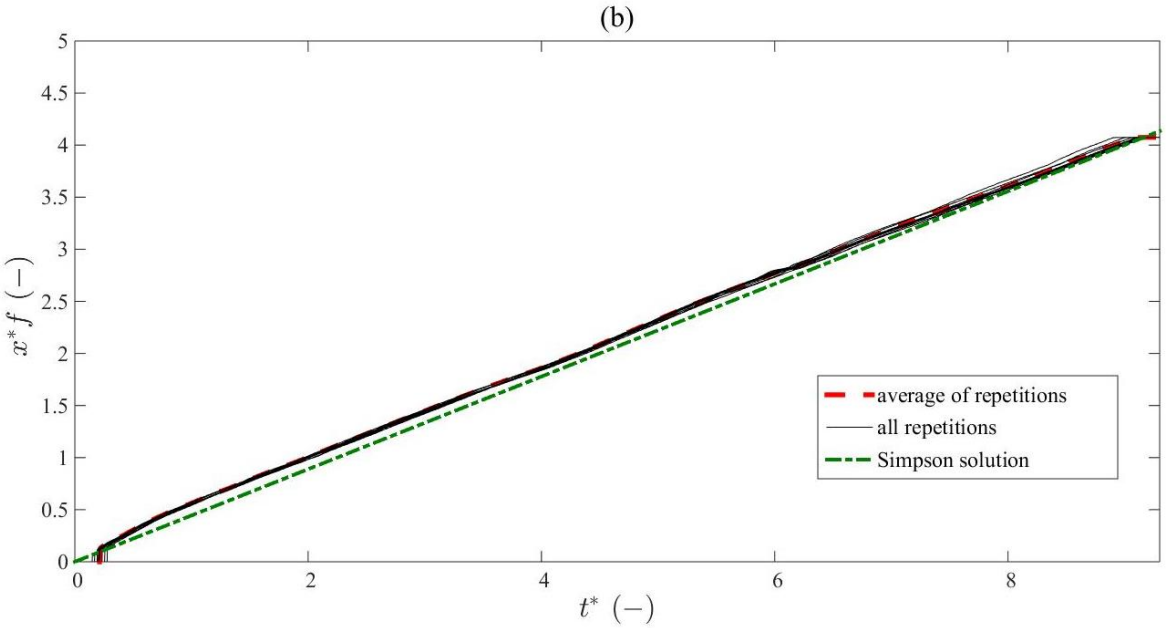

Figure 4.2: Front current evolution for : (a) $g' = 0.09\ \mathrm{m}/s^2$; (b) $g' = 0.36\ \mathrm{m}/s^2$ before the array of cylinders.

Figure 4.2. shows a linear progression of the current front position in the first half of the channel, without vertical obstacles, evidencing a constant velocity of the current front as expected in a slumping phase.

Comparing the various repetitions for the current where $g' = 0.36\ \mathrm{m}/s^2$ it is visible the tests have a good repeatability since there is little variation of the results. In Figure 4.2 (a) for $g' = 0.09\ \mathrm{m}/s^2$ there is also little variation in the results, but the differences are higher if compared to the fastest current for a superior time. That can be explained due to a minor influence of inertial forces into the current. Since the differences are small the tests ensure the repeatability conditions.

As shown in both cases, the dark green line is the solution for the current front progression given by Simpson (1980). The similarity of the results to the Simpson solution indicates the presence of the slumping phase as expected. The current front propagation dimensionless velocity is the slope of the average curve and his value is approximately 0.45.

Is noticeable a jump in the beginning of the curves that is a result of the current front analysis starts after the lock position at $x = 0.3\ m$.

In Figure 4.3 is presented the front evolution of the current to the reduced gravity of $0.09\ \mathrm{m}/s^2$ and $0.36\ \mathrm{m}/s^2$ for the second part of the channel, with the influence of the array of cylinders.

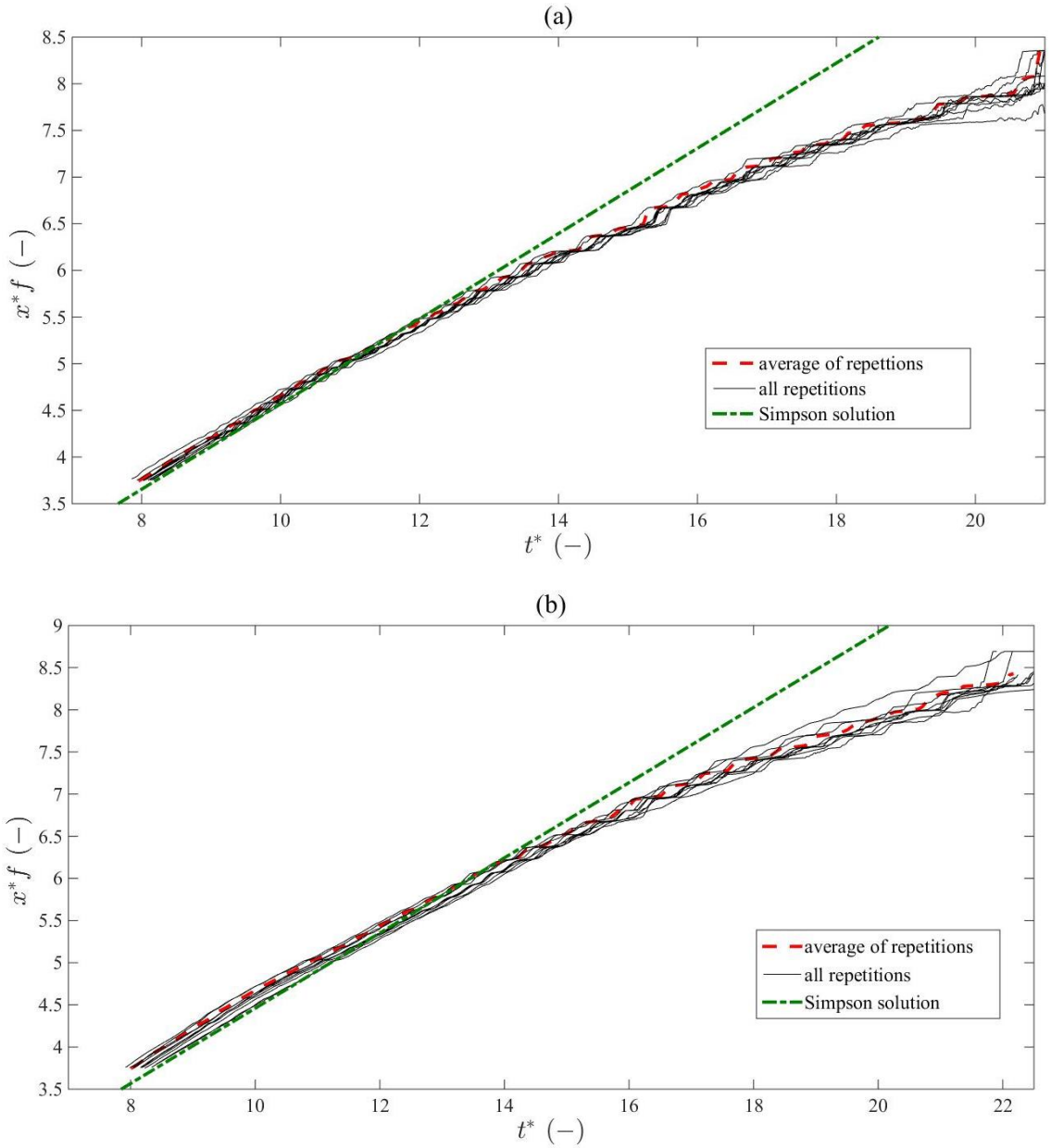

Figure 4.3: Front current evolution for: (a) $g' = 0.09\ \mathrm{m}/s^2$; (b) $g' = 0.36\ \mathrm{m}/s^2$ in the array of cylinders.

Figure 4.3 shows the progression of the current front for the second part of the channel. It follows a straight pattern until $t^* = 9$, then as the current advances throughout the array of cylinders the current front loses speed, and the front position does not vary linearly as the previously cases without cylinders. This can be seen by following the Simpson solution given in the green line.

As shown in Figure 4.3 (a) and (b) there is some oscillation in all repetitions after $t^* = 9$ due to the fact the cylinders used in the experiment are made from acrylic and as the current passes between a row of cylinders it reflects the current in the cylinder which made the detection of the current subject to a small imprecision. The variability of the front position increases as the current advances within the array.

Figure 4.4 shows the variation of the ensemble average position of the current front for all the channel length being: (a) the junction of the current averages for the $g' = 0.09\ \mathrm{m}/s^2$ before and during the array of cylinders and (b) the $g' = 0.36\ \mathrm{m}/s^2$ for the same case.

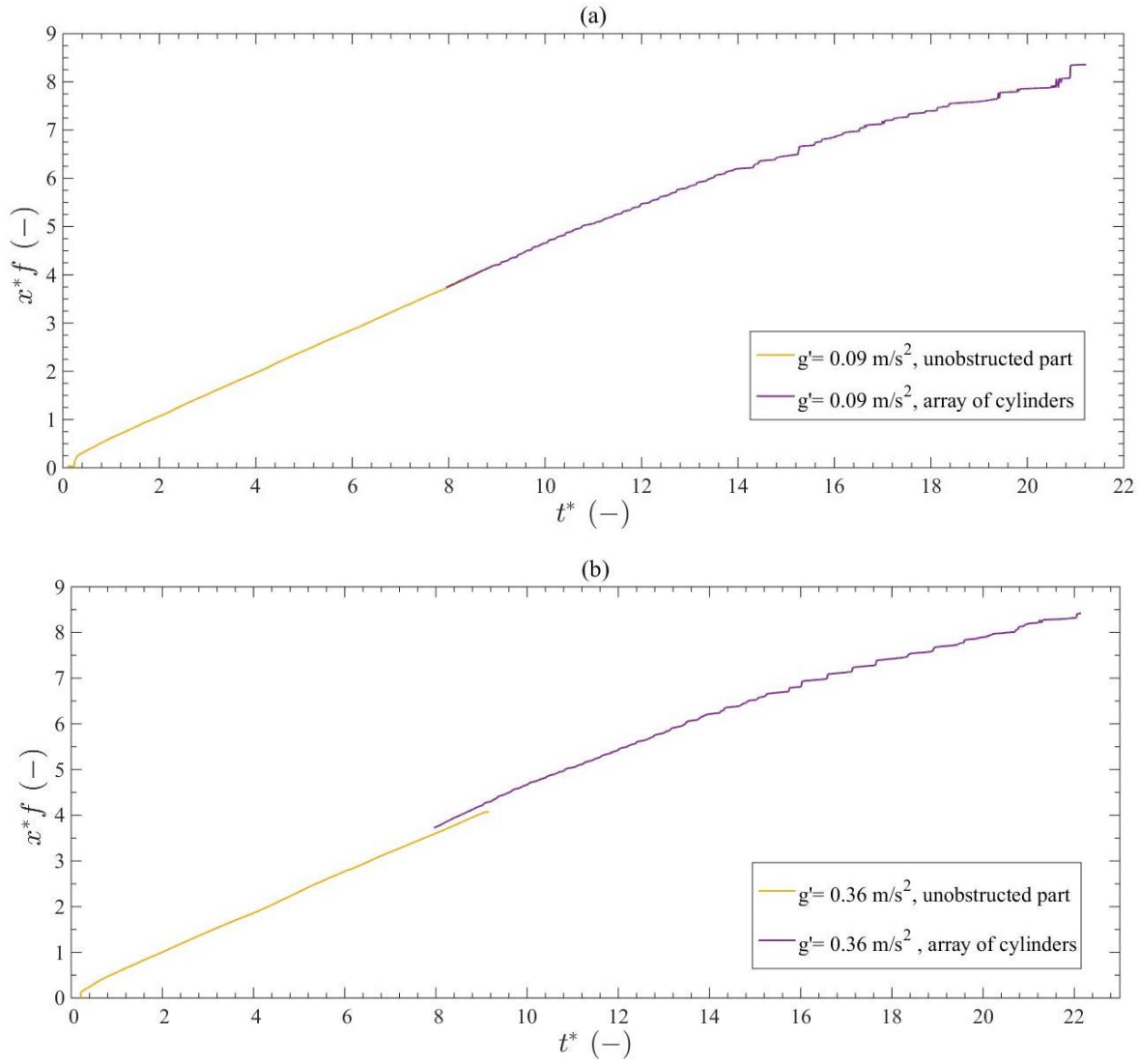

Figure 4.4: Front current evolution for all channel length: (a) $g' = 0.09\ \mathrm{m}/s^2$; (b) $g' = 0.36\ \mathrm{m}/s^2$.

It is possible to verify for both cases (a) and (b) the linear pattern of the front position until $t^* = 9$, then the linear evolution of the current front suffers a decrease due to the current propagation loss of speed that is caused by the impact of the current in the array of cylinders.

The difference in the reduced gravity between currents seems to have little influence in the behaviour of the current front propagation along the channel.

4.3 Spanwise-average current structure

This section presents and discusses the current density fields distribution, the current height, the conservation of mass and the dilution of the current aiming at the characterization of the effects of the array of cylinders in the current structure.

4.3.1 Current density field

Figure 4.5 shows the current density fields distribution for two-time instants regarding the current average and one repetition for the $g' = 0.09\ \mathrm{m}/s^2$ for the lock view while Figure 4.6 is related to the $g' = 0.36\ \mathrm{m}/s^2$ current.

In the first line, (a) and (b) are the images for the ten repetitions averaged current. In the second line, (c) and (d) are the results for one of the repetitions.

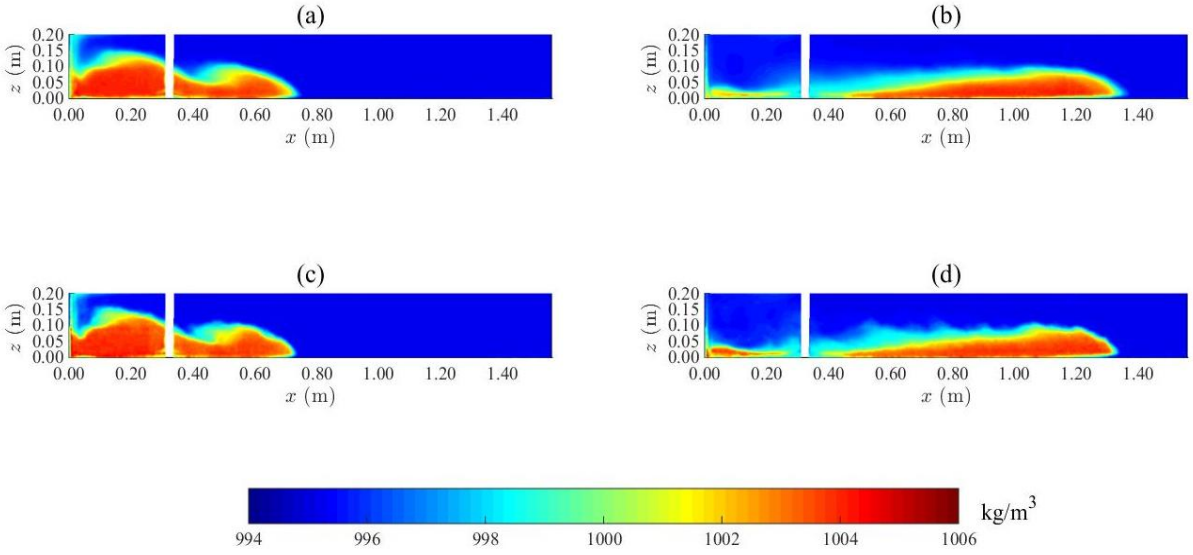

Figure 4.5: Current density field for: (a) average of repetitions, t = 6 s, (b) average of repetitions, t = 16 s, (c) test 2, t = 6 s, (d) test 2, t = 16 s.

The white vertical line in the figures around the 0.30 m is the place where the lock was placed. This part was masked to avoid some interferences in the image results due to vaseline particles that remain in the channel after the lock was released.

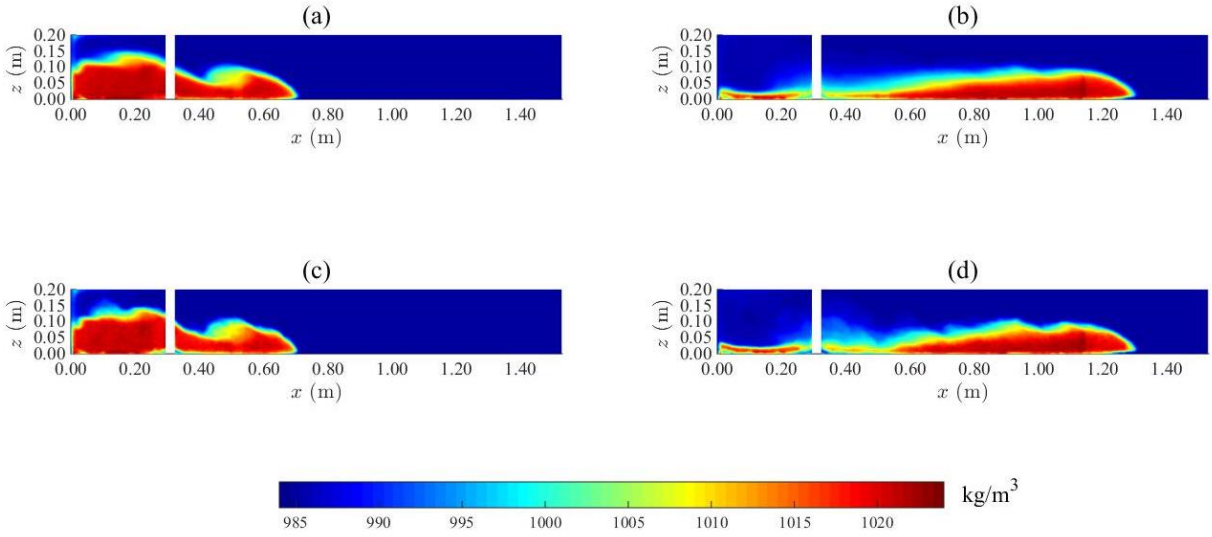

Figure 4.6: Current density field for: (a) average of repetitions, t = 3 s, (b) average of repetitions, t = 8 s, (c) test 2, t = 3 s, (d) test 2, t = 8 s.

In Figure 4.5 and Figure 4.6 (a) and (c) is possible to see the current shape some seconds after the lock was released. In that time the current head starts to develop due to the mixing of the fluids. In (b) and (d) as the current progresses through the channel and the mixing process continues, the current develops the body and the tail part. In both figures the blue area marks the presence of the ambient fluid while the red area corresponds to the denser fluid. The areas in the images with an intermediate colour correspond to the places where the mixing processes are occurring.

By comparing the images of the averaged current with the repetition analysed is possible to observe a similarity in the current structure and position in the channel. The good repeatability of the tests in the lock view was achieved.

Figure 4.7 shows the current density fields for two-time instants regarding the current average and one repetition for the $g' = 0.09\ \mathrm{m}/s^2$ for the array of cylinders view while Figure 4.8 is related to the $g' = 0.36\ \mathrm{m}/s^2$.

In the first line, (a) and (b) are the images for the ten repetitions averaged current. In the second line, (c) and (d) are the results for one of the repetitions.

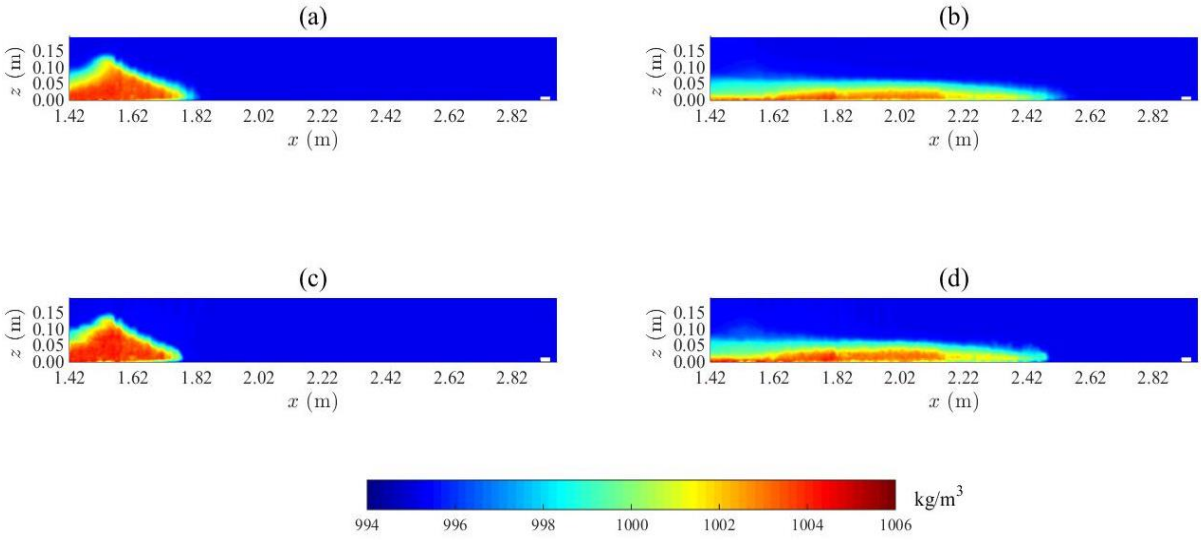

Figure 4.7: Current density field for (a) average of repetitions, t = 24 s, (b) average of repetitions, t = 38 s, (c) test 2, t = 24 s, (d) test 2, t = 38 s.

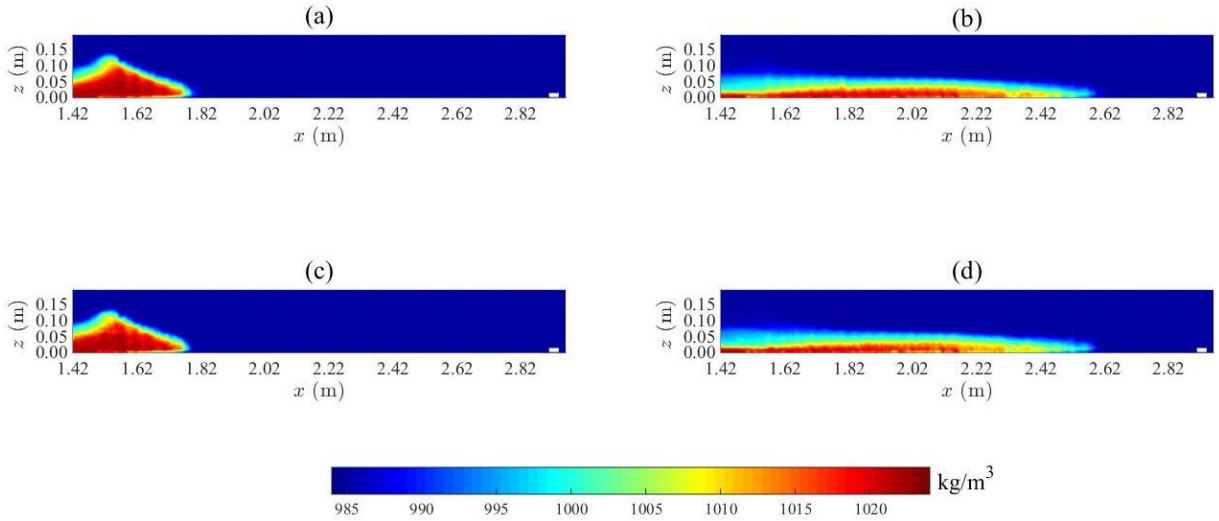

Figure 4.8: Current density field for (a) average of repetitions, t = 12 s, (b) average of repetitions, t = 20s, (c) test 2, t = 12 s, (d) test 2, t = 20 s.

.

In Figure 4.7 and Figure 4.8 (a) and (c) is represented the current front after the impact with the first row of cylinders. In (b) and (d) as the current progresses through the array of cylinders the current head loses the shape it presented in Figure 4.5 and Figure 4.6.

By comparing the images of the averaged current with the repetition analysed is possible to observe a similarity in the current structure and position in the channel. The good repeatability of the tests in the array view was achieved.

4.3.2 Current height

To address the variation of the current height all over the channel were used the concentration isolines since the current height can be obtained by determining the interface of the fluids where the concentrations is 0.05 in the head region. This concentration isoline is shown in dark blue in the following figures.

Figure 4.9 shows the results of the for the average current for $g' = 0.09\ \mathrm{m}/s^2$.

As it is possible to see by the axes, the images (a) and (b) are related to the lock view, without the presence of the cylinders, while the images (c) and (d) start from 1.42 m and goes until 3 m, being in the presence of the array of cylinders.

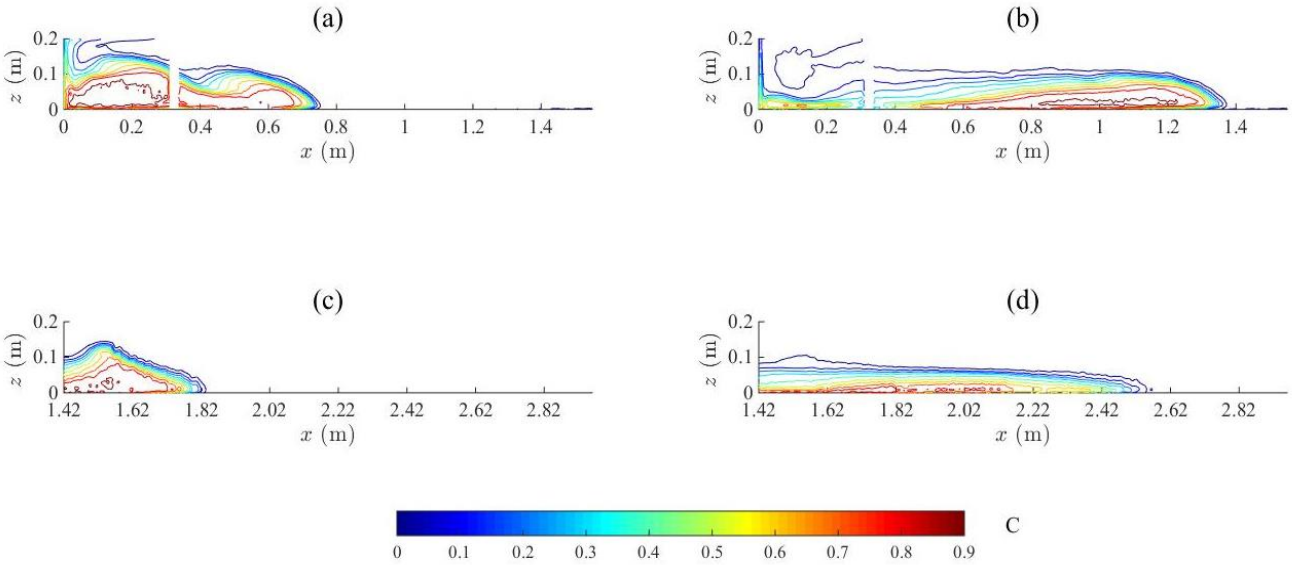

Figure 4.9: Height evolution of the average current $g' = 0.09\ \mathrm{m}/s^2$:
(a) t = 6 s , (b) t = 16 s, (c) t = 24 s, (d) t = 38 s.

In Figure 4.9 is possible to see the variation of the current height all over the channel. In Figure 4.9 (a) the current head it is in the developing stage so it is not possible to address a value to the current in these stage.

In Figure 4.9 (b) as the current progresses in the unobstructed part of the channel the height in the current head has a value of around 0.08 m.

In Figure 4.9 (c) the current has already reached the first rows of cylinders and their effect is visible in the figure because when the current hits the cylinder there is an increase of the height upstream the cylinder reaching a height above 0.10 m, while at downstream there is a quick decrease of the height.

In Figure 4.9 (d) the current is still progressing throughout the array and is visible the height continues to drop to as the current past the rows of cylinders.

While compare the (b) and (d) images is possible to see the reduction of the current height before and after it reaches the array of cylinders.

In Figure 4.10 is shown the results of the current contours for the average current for $g' = 0.36\ \mathrm{m}/s^2$. The methodology of the graphs presented is the same as in Figure 4.9.

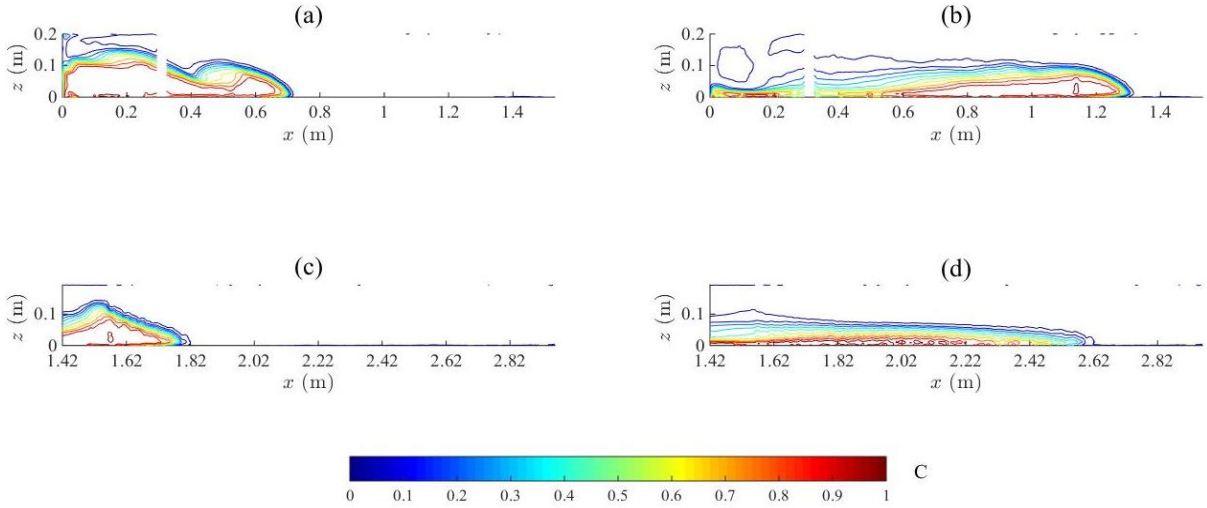

Figure 4.10: Height evolution of the average current $g' = 0.36\ \mathrm{m}/s^2$:
(a) t = 3 s , (b) t = 8 s, (c) t = 12 s, (d) t = 20 s.

The results shown in Figure 4.10 are very similar to the ones obtained for the currents with reduced gravity of $0.09\ \mathrm{m}/s^2$, which means the current height is not affected by the density differences between the fluids.

4.3.3 Vertical profile of concentration

In this section is presented the vertical profile of concentration for several points in the channel for specific time instants. The figure shows the value of concentration as a function of a normalized height, z/h_0 , where h_0 is the free surface height.

For the current with a reduced gravity of $0.09\ \mathrm{m}/s^2$, in the second half of the channel, was chosen the time, t = 44 s, where the current is almost reaching the end of the channel.

In Figure 4.11 are represented the points of measurement for the vertical profile of concentration.

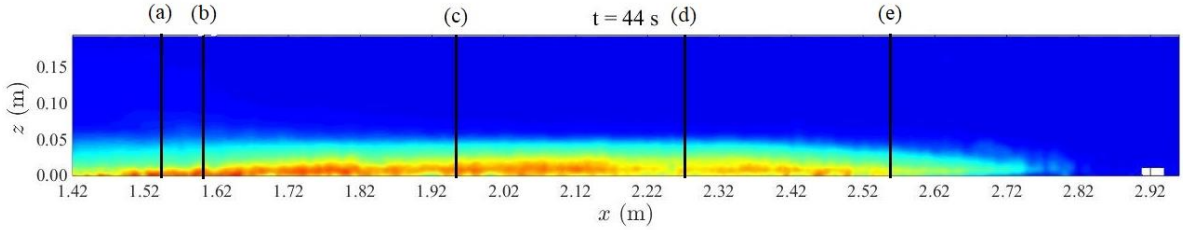

Figure 4.11: Representation of the lines used to measure the vertical profile of concentration.

In Figure 4.12 is represented the vertical profiles of concentration at different points for the $0.09\ \mathrm{m}/s^2$ current.

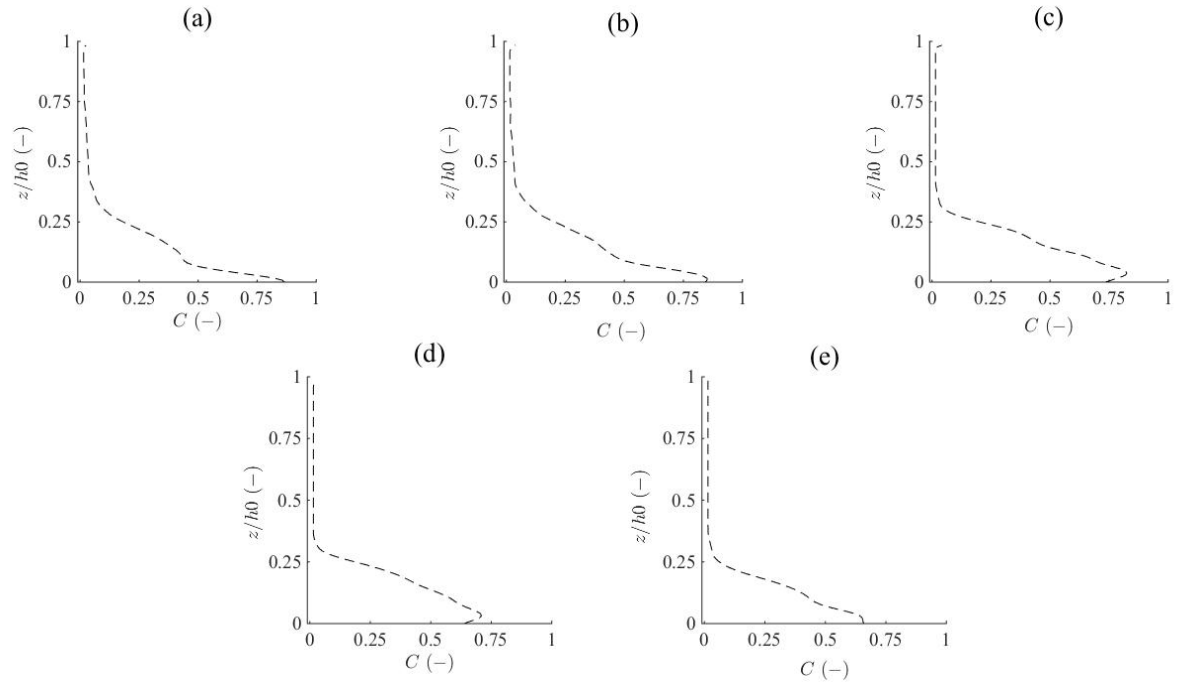

Figure 4.12: Vertical profile of concentration at time instant t = 44 s for $g' = 0.09\ \mathrm{m}/s^2$at: (a) 1.54 m, (b) 1.60 m, (c) 1.96 m, (d) 2.27 m, (e) 2.55 m.

It is visible in the image (a), (b) and (c) the concentration reaches a value above 0.75 near the bottom of the channel and then there is a reduction to a value below 0.75 in image (d) and (e). This reduction is expected as the lines (d) and (e) are placed in a region closer to the current front where the mixing processes with the ambient fluid were intense. There is a similar pattern in the variation of the concentration as the height varies.

For the current with a reduced gravity of $0.36\ \mathrm{m}/s^2$, in the second half of the channel, was chosen the time, t = 24 s, where the current is almost reaching the end of the channel.

In Figure 4.13 are represented the points of measurement for the vertical profile of concentration.

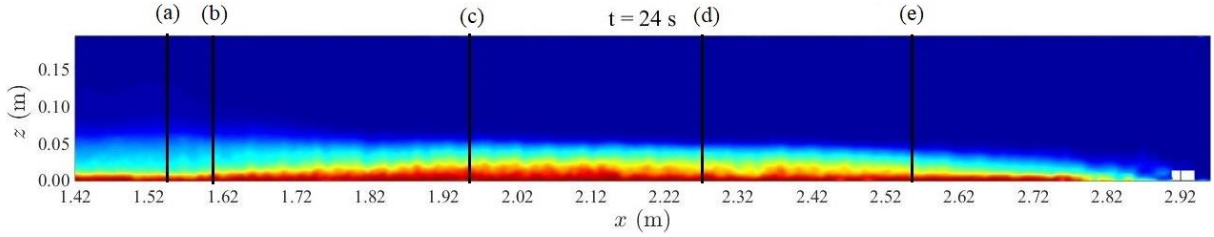

Figure 4.13: Representation of the points used to measure the vertical profile of concentration.

In Figure 4.14 is represented the vertical profiles of concentration at different points for the $0.36\ \mathrm{m}/s^2$ current.

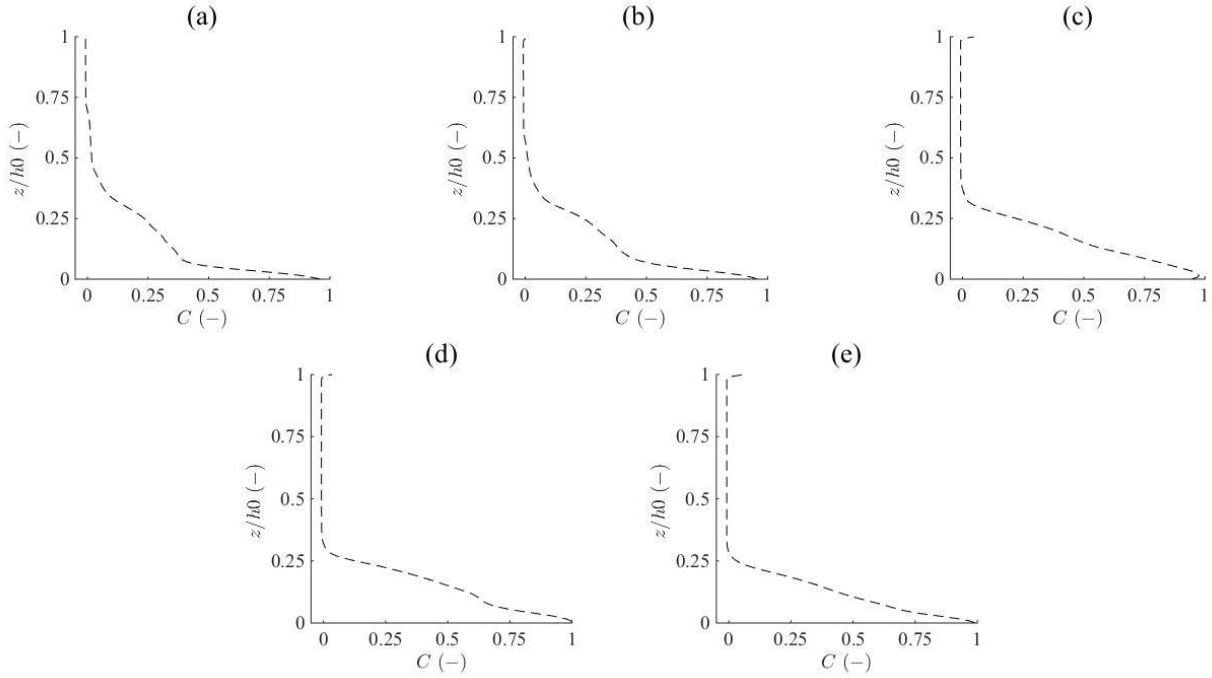

Figure 4.14: Vertical profile of concentration at time instant t = 24 s for $g' = 0.36\ \mathrm{m}/s^2$ at: (a) 1.54 m, (b) 1.60 m, (c) 1.96 m, (d) 2.27 m, (e) 2.55 m.

As is visible throughout the different graphs, for the higher reduced density current the value of the concentration reaches a value approximate to 1.

For the graphs (a) and (b) the variation of the concentration doesn´t fall a linear pattern while in graphs (c) to (e) is visible a linear increase of the concentration as the normalized height tends to 0.

A possible explanation to this phenomenon is the point (a) and (b) which have coordinates 1.54 m and 1.60 m, correspondently, are near the region where the first row of cylinders is placed. When the current passed in this area, a part of it climbs the cylinders wall (as was seen in section 4.2.2) and even after some seconds there is some mixing taking place in the upper part of the channel.

4.3.4 Conservation of mass

To validate the measurement method used in this experiment, the assess of the mass conservation is a parameter to consider. The total volume in the measurement area is the sum of the denser fluid with the ambient fluid, and by the principle of mass conservation the total fluid mass in the channel is constant. To compute the mass total value was made the integration of the concentration in all space.

Figure 4.15 represents the variation of mass throughout the experiment time for the average of the four currents studied.

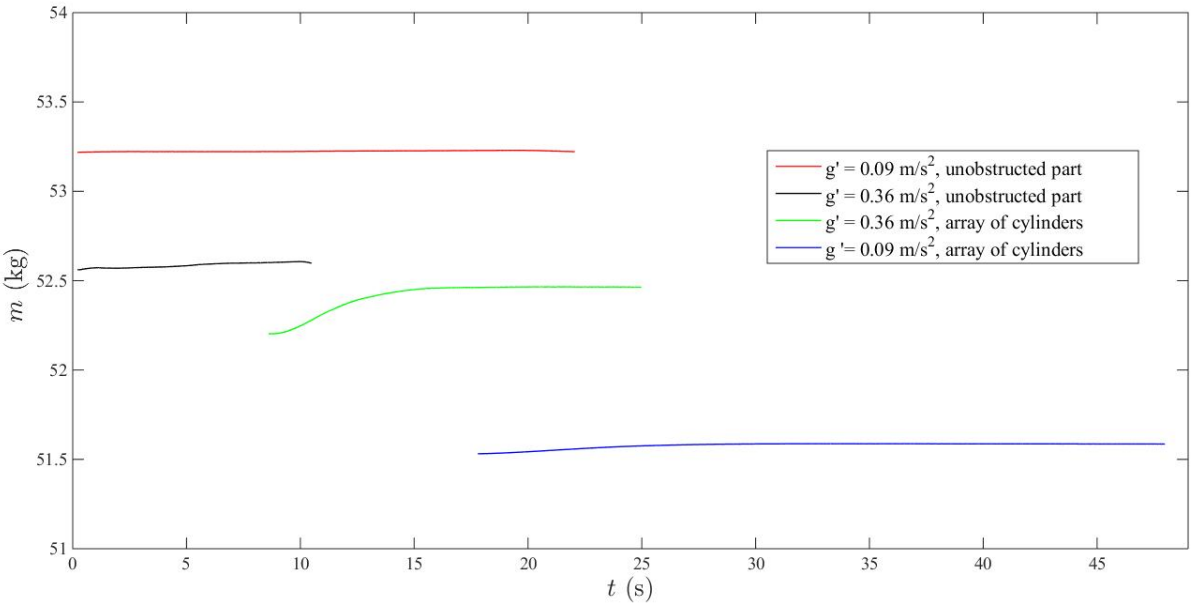

Figure 4.15: Values of the total mass of fluid in the channel as a function of time for the various reduced gravitational accelerations.

Figure 4.15 confirms the maintenance of the mass value for each current throughout the experiment.

The mass value for the current with a reduced gravity of $0.36\ \mathrm{m}/s^2$ should be higher to the currents with $g' = 0.09\ \mathrm{m}/s^2$. This situation is not confirmed by Figure 4.15 results for the currents in the obstructed part. In every repetition was difficult to reach the target height of 20 cm for the free surface. During the data treatment was discovered the repetitions in the array of cylinders have a free surface with a few millimetres less than 20 cm while the current with a reduced gravity of $0.09\ \mathrm{m}/s^2$ in the obstructed part had a few millimetres more. This difference can explain why the current with $g' = 0.09\ \mathrm{m}/s^2$ have a higher mass.

4.3.5 Entrainment

In section 4.1, the entrainment was defined as the increase in volume of the dense fluid stream by the mixing with the ambient fluid and its computation was presented in Equation (4.2). For this study the fluid stream is defined by the volume of fluid with a concentration greater than 0.05. The precise limits of the fluid stream are difficult to identify in practical conditions, thus a threshold is assumed based on the recommendations of literature and on some sensitivity analysis carried out with the analysed data. The theoretical value would be $C = 0$, but as that is impracticable for laboratory data, which is not free of uncertainty, the value of $C = 0.05$ is used as compromise.

In the following figures are shown the graphs of the variation of the Entrainment as a function of time for the currents with a reduced gravity of $0.09\ m/s^2$ and $0.36\ \mathrm{m}/s^2$ for the cases with and without the array of cylinders.

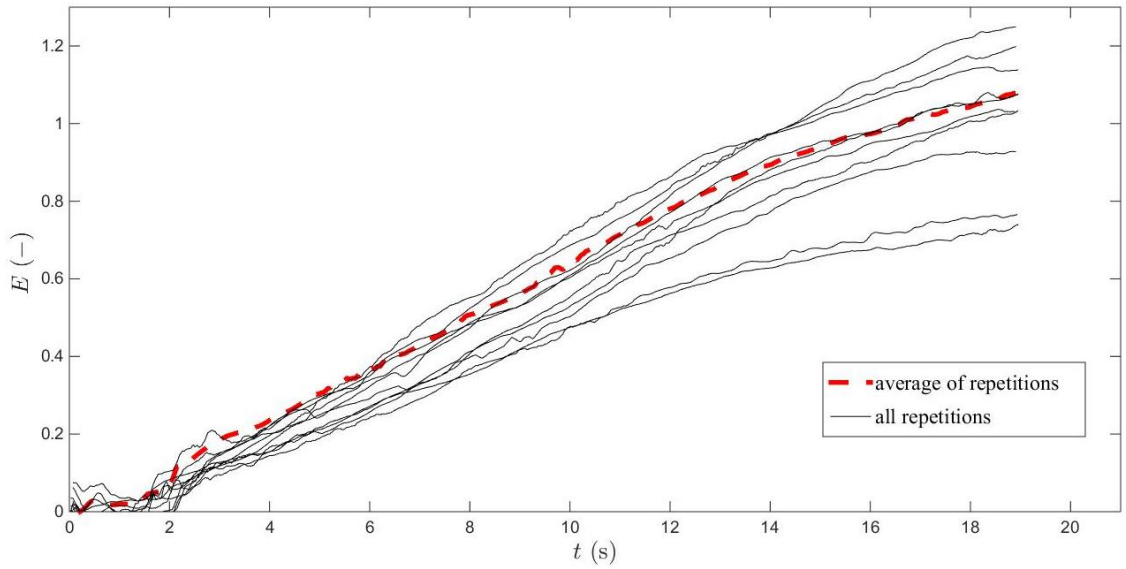

Figure 4.16: Temporal evolution of the entrainment for the density current with $g' = 0.09\ \mathrm{m}/s^2$ before the array of cylinders.

In Figure 4.16 is observed the entrainment increases as the current progresses on the unobstructed channel. In the first 2 seconds the value is almost constant because the density current is not totally formed and the mixing process it is in his initial stage. From $t = 2$ until the end of the analysis the entrainment grows as the mixing process of the ambient fluid in the denser current hits is maximum. During this time the current has enough kinetic energy to promote the mixing.

In Figure 4.17 is presented the temporal evolution of the entrainment for the density current with $g' = 0.36\ \mathrm{m}/s^2$ before the array of cylinders

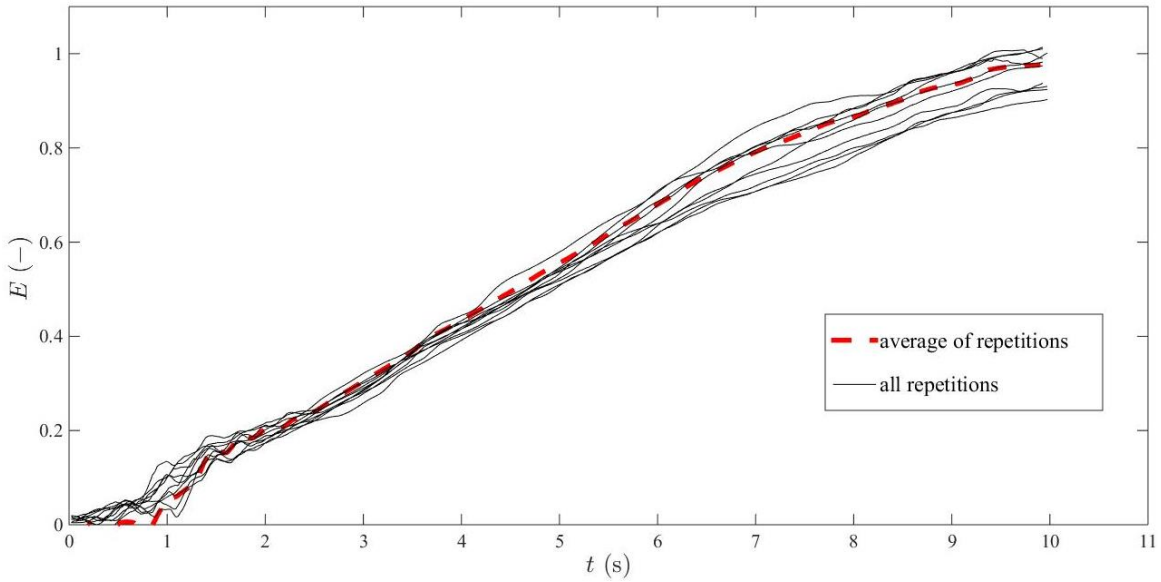

Figure 4.17: Temporal evolution of the entrainment for the density current with $g' = 0.36\ \mathrm{m}/s^2$ before the array of cylinders.

In Figure 4.17 is observed a similar behaviour for the entrainment as was shown in Figure 4.16. It increases as the current progresses throw the unobstructed channel but since the reduced gravity is higher in this current, the entrainment is now constant in the first second of the experiment, while on the other case was constant until two seconds.

It is important to notice that for the repetitions of a current with a reduced gravity of $0.36\ \mathrm{m}/s^2$ there was less variation in the values of the entrainment as the repetitions with a reduced gravity of $0.09\ \mathrm{m}/s^2$ shown in Figure 4.16.This pattern was also observed in section 4.1 in the values for the current front evolution for the currents analysed before the array of cylinders. The higher variation was caused due to a minor influence of inertial forces into these current.

In Figure 4.18 is presented the temporal evolution of the entrainment for the density current with $g' = 0.09\ \mathrm{m}/s^2$ in the array of cylinders.

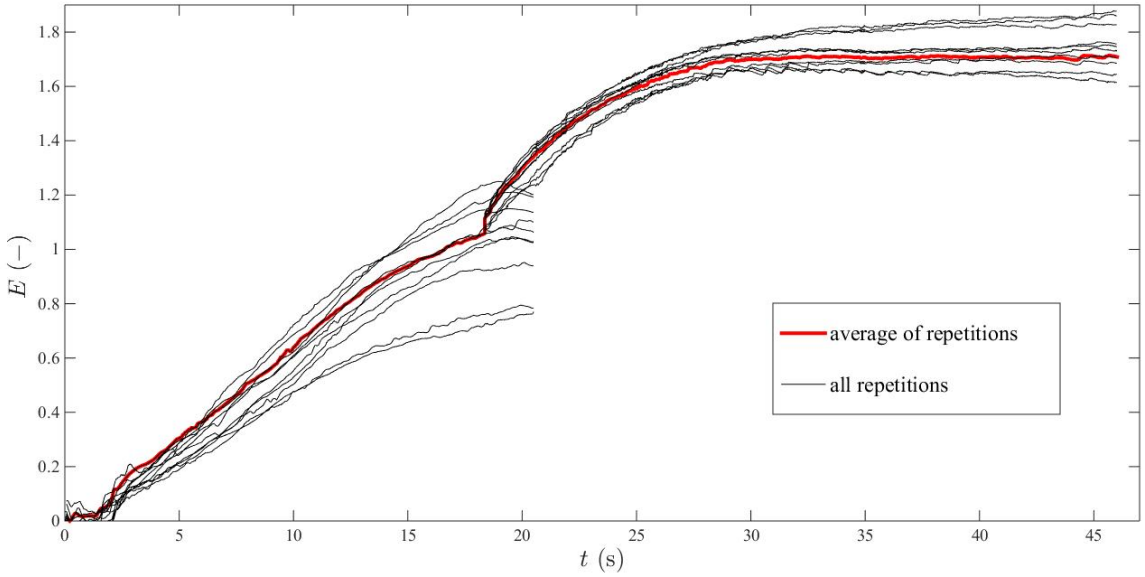

Figure 4.18: Temporal evolution of the entrainment for the density current with $g' = 0.09\ \mathrm{m}/s^2$ in the array of cylinders.

Within the array of cylinders, the methodology for the computation of the entrainment was adapted to include the volume of the current that was out of the field of view.

The current volume computation was the summation of the volume within the array and the volume in the unobstructed part, for the same time instant. As there are no measurements of the current in both parts of the channel, the current volume in the unobstructed part was obtained from the averaged current for each corresponding time. This was possible because the recordings in the unobstructed part were long enough allowing to observe the density changes on the current tail until the head have arrived at the end of the array.

In Figure 4.18 is possible to observe this methodology. From 0 to about 19 seconds there is a red line representing the variation of the entrainment for the average current before it reaches the array of cylinders. There is a window in the images ($x = [1.42, 1.55]\, m$), that the camera sees while placed in different positions (lock view and array view), so was determined the time where the current hit the x position around 1.42 m to decide the time where the synchronization was made.

Regarding the entrainment behaviour it increases from the 2 seconds, already discussed, until a time of around 30 seconds, then it keeps a constant value of 1.7 until the end of the experiment.

From the 30 seconds until the end there is not a variation of the current volume, so the ambient fluid does not mix with the denser fluid anymore. Some possible explanations for this phenomenon are the current does not have enough kinetic energy to promote the mixing anymore due to the presence of the array of cylinders and there is a saturation in the current interface that stops the injection of the ambient fluid into the denser current.

In Figure 4.19 is presented the temporal evolution of the entrainment for the density current with $g' = 0.36\ \mathrm{m}/s^2$ in the array of cylinders.

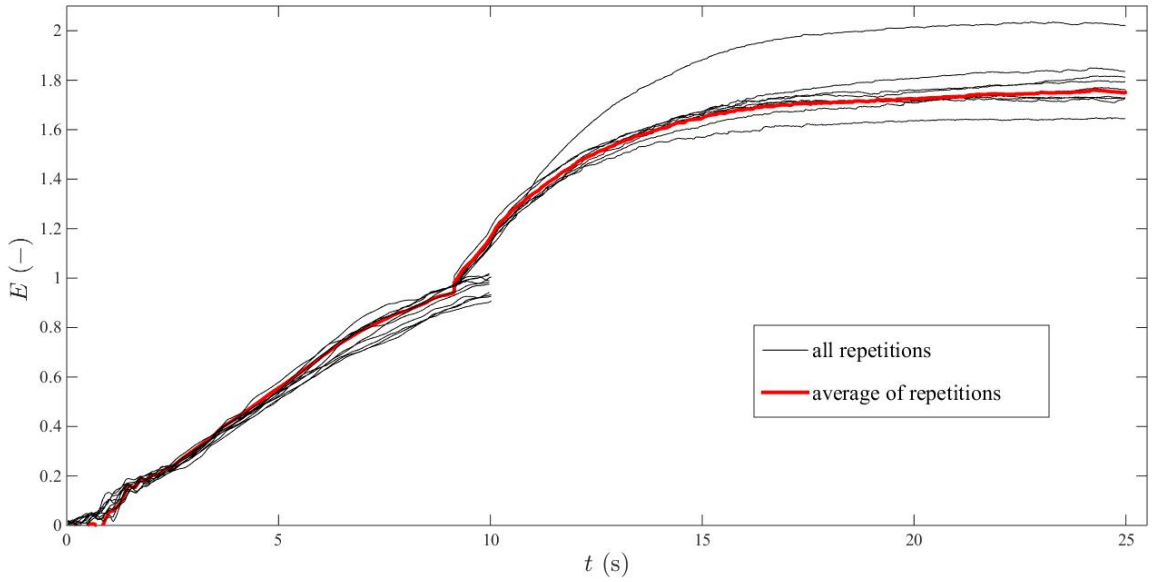

Figure 4.19: Temporal evolution of the entrainment for the density current with $g' = 0.36\ \mathrm{m}/s^2$ in the array of cylinders.

The methodology used to compute the entrainment for the $g' = 0.36\ \mathrm{m}/s^2$ current is the same used for the previous current analysed in the Figure 4.18.

Regarding the behaviour of the entrainment is possible to conclude it´s very similar in both currents, as it grows until the current has enough kinetic energy to promote the mixing and then there is not variation in the current volume, so the entrainment gets a constant value until the end of the experiment.

5 Velocity field characteristics

5.1 Introduction

This chapter is dedicated to the presentation of the results regarding the velocity field characteristics of the density currents.

Regarding the tests where the velocity field characteristics are going to be analysed was used the PIV technique.

In total 40 repetitions were made. For the side view were made 10 repetitions with a reduced gravity of approximately 0.36 m/s^2 and another 10 repetitions with a reduced gravity of 0.09 m/s^2. For the plan view were made 20 repetitions with a reduced gravity of 0.09 m/s^2, because with a reduced gravity of 0.36 m/s^2 the images obtained did not have the desire quality due to some blur caused by the high quantities of alcohol placed in the channel for those tests.

To have a clear view about the side and plan field of view, in Figure 5.1 there is a representation of the field of views with the main dimensions associated. The green rectangle represents the camera field of view, x_0 is the distance of the lock to the left wall and the other dimensions are the limits of the camera field of view that slightly vary from test to test.

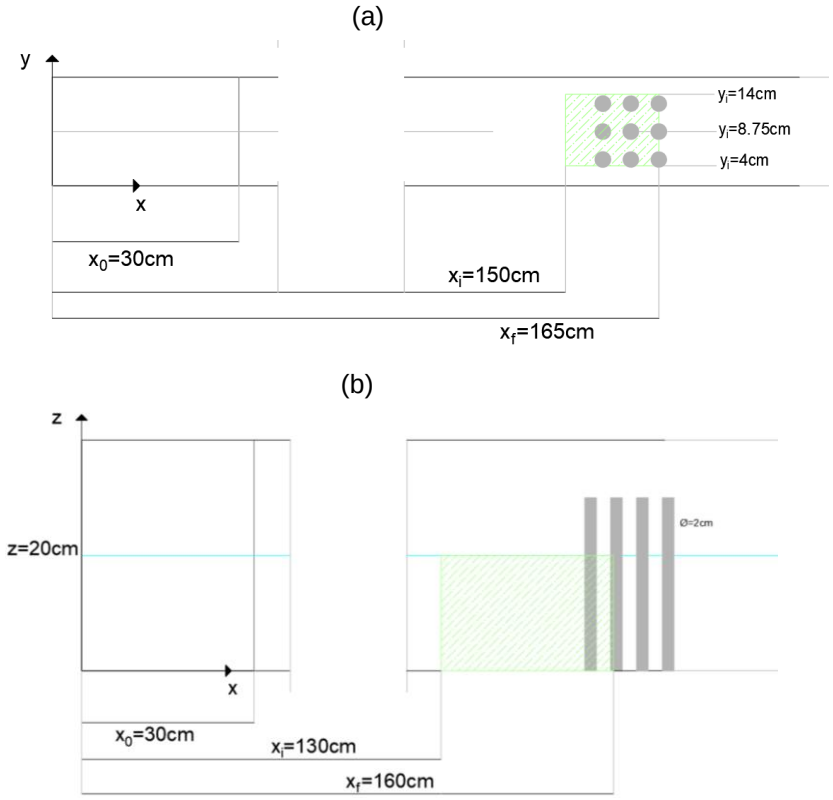

Figure 5.1: Field of view for the PIV tests: (a) plan view (b) side view.

In this chapter a comparison of the results obtained with the configuration of the array of cylinders will be made with the results obtained with the density currents interacting with an isolated cylinder. The tests with the isolated cylinder were carried out in the scope of the WinTherface project by other student.

Figure 5.2 shows a schematic 3D view of the channel with the isolated cylinder. The cylinder is positioned at a distance of approximately 90 *cm* from the channel left wall and have a diameter of 2.5 *cm*.

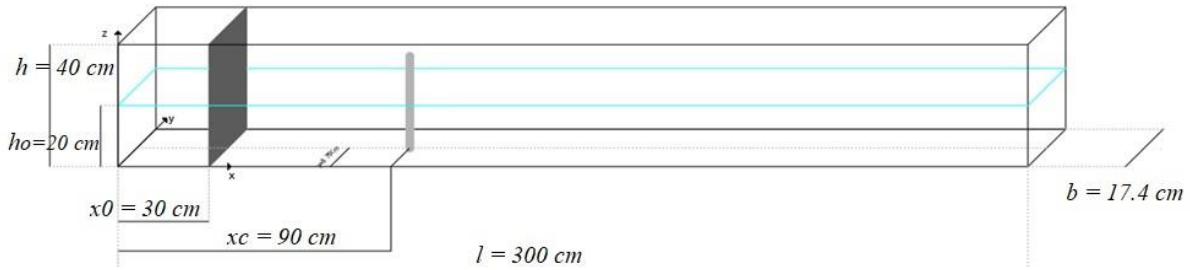

Figure 5.2: 3D view of the channel with the isolated cylinder

This chapter is divided into two sections, one regarding the presentation of results for the instantaneous velocity fields and the other the results for the impact of turbulence in current head and tail structure. In the next paragraphs is going to be explained the method used to obtain some variables important for the turbulence analysis.

1. Velocity time series

The first step was to obtain the longitudinal, transversal and vertical instantaneous velocities for every repetition. For the side view the instantaneous velocities are represented with u (longitudinal) and w (vertical direction), while for the plan view are represented with u (longitudinal) and v (transversal direction).

Then was obtained a time series for the velocities in several points of the channel for the mean current.

In Figure 5.3 is shown an example of the velocity time series for the point $(1.47,0.025)\ m$ in the mean current.

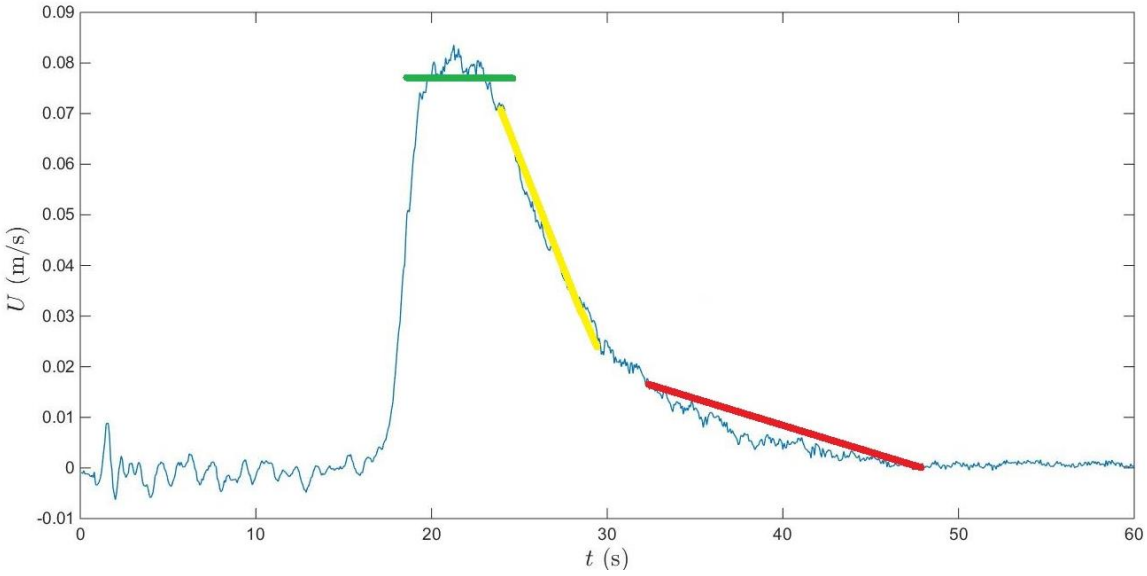

Figure 5.3: Longitudinal velocity variation of the current in the point $(1.47, 0.025)$.

By analysing Figure 5.3 is possible to verify the current front starts passing in the defined point at approximately 18 seconds, since there is a huge increase in the velocity. Then there is peak with a plateau marked with a green line in the graph that corresponds to the passage of the current head. After the plateau the velocity decreases rapidly, represented with the yellow line. At around 30 seconds and until 48 seconds, the velocity still decreases but with a lower rhythm which marks the passing of the current tail by that point, represented with the red line.

After obtaining the time series for several points of the mean current, was determined the time limits of the plateau, as shown in Figure 5.3, and the time limit of the tail. For the tail was used a polynomial function with a parabolic shape to detect the trend of the current. The methodology to obtain the plateau is shown in Appendix 4.

After obtaining the time intervals in the mean current, those were used to extract the velocity components in all the repetitions in the analysed current. With this method was possible to obtain the velocities for the chosen points in all repetitions, within the time interval correspondent to the head or tail.

The instantaneous velocity field u, is divided in two contributes:

$$u = \bar{u} - u' \tag{5.1}$$

where, the mean velocity field $(\bar{u})$ is obtained through the ensemble average of the instantaneous velocity field. The current head can be considered a quasi-steady flow, so the fluctuations (u') are obtained by subtracting the ensemble average field with the instantaneous one. In the tail the flow is characterised by a decreasing trend, so the fluctuations are obtained by subtracting the temporal trend which is defined by the parabolic curve to the instantaneous velocity field.

Table 5.1 presents a resume of the defined time intervals and the correspondent number of time instant obtained for the analysed currents.

Table 5.1: Values for the considered time interval and number of time instant for the extraction of velocity components

$g'(m/s^2)$	Section	Time interval (s)	Number of time instant
0.09	Side view/head	-	368
	Side view/tail	30-48.47	2780
	Plan view/head	19.47-22.27	430
	Plan view/tail	28-42	2110
0.36	Side view/head	-	278
	Side view/tail	16-27	1660

In Table 5.1 is perceptible that in the case the current is measured in the side view, regarding the head there is not a defined time interval for the current average where the velocities were obtained.

Since a steady and constant shape of the head can be identified in the side view, it was followed until the impact with the array of cylinders. The shape considered goes from the current nose until the beginning of the first billow, with a length of 8 cm. To always see the same part of the current, the visualization window is moved at the front velocity. Since there are some changes between the values of g' between repetition, small differences in the front velocity are detected and consequently different intervals of time are obtained. At the end of the process the velocity fields for each time analysed for a relative position in the head are obtained for each repetition.

This principle of obtaining the velocities is called moving average and was not used for the side view in the tail because it is difficult to track the current shape. Regarding the plan view it is not possible to detect and track the head and tail shapes with this configuration.

Once the velocities were obtained the next step was to compute the order moments.

2. Order moments

To study the turbulent density currents is necessary to compute the order moments. The first order moments are the ensemble averaged velocity components. The second order moments are obtained by applying the Reynolds decomposition into the Navier Stokes equation, obtaining the Reynolds Stress tensor that represents the mean momentum fluxes induced by turbulence. The third order moments explain how the energy extracted by the Reynolds stress is redistributed in the multiple directions.

The different order moments are presented in the equation of conservation of the turbulent kinetic energy (TKE):

$$\underbrace{\frac{1}{2}\bar{u}_j\frac{\partial\overline{u_i'u_i'}}{\partial x_j}}_{1}+\underbrace{\overline{u_i'u_j'}\frac{\partial\bar{u}_i}{\partial x_j}}_{2}+\underbrace{\frac{1}{2}\frac{\overline{u_i'u_i'u_j'}}{\partial x_j}}_{3}=\underbrace{-\frac{1}{\rho}\frac{\partial\overline{p'u_j'}}{\partial x_j}}_{4}+\underbrace{2\upsilon\frac{\partial\overline{s_{ij}u_i'}}{\partial x_j}}_{5}-\underbrace{\bar{\varepsilon}}_{6} \tag{5.2}$$

where i and j are indices running from 1 to 3, x_j stand for three Cartesian spatial directions, $\frac{1}{2}\overline{u_i'u_i'}$ is the TKE per unit mass, referred as TKE, $\bar{u}_j$ and u_j' are the jth components of, respectively, the time-averaged velocity and the instantaneous time fluctuations. (Ricardo et al., 2014).

In Equation (5.2) Term 1 is the convective rate of change of TKE, Term 2 is the rate of production, term 3 is the turbulent transport, Term 4 is the pressure diffusion, Term 5 is the viscous diffusion and Term 6 is the rate of dissipation. It is not going to be made a quantification of these terms since is very difficult to obtain the components derivatives through experimental work.

In the following equations are presented some examples of the components that are called order moments which are presented in Equation (5.2).

Equation (5.3) is related to the first order moment, Equation (5.4) is related to the second order moment and finally Equation (5.5) is related to the third order moment.

$$\bar{u}(x)=\frac{\sum_{i=1}^{N}u_i(x)}{N} \tag{5.3}$$

$$\overline{u'u'}(x)=\frac{\sum_{i=1}^{N}u'_i(x)\,u'_i(x)}{N} \tag{5.4}$$

$$\overline{u'u'u'}(x)=\frac{\sum_{i=1}^{N}u'_i(x)u'_i(x)u'_i(x)}{N} \tag{5.5}$$

where N is the total number of time instant extracted in each point. The methodology to compute the various order moments is presented in Appendix 5.

The different order moments were dimensionless by the current buoyancy velocity, given in Equation (2.2).

5.2 Velocity fields

In this section is presented the results for the instantaneous velocity fields of the density currents measured in the side view and in the plan view.

5.2.1 Side view

For the side view the velocity components were extracted in a plane illuminated by the laser beam at $y = 0.0875\ m$.

In Figure 5.4 is presented a sequence of images that represent the variation of the longitudinal velocity u in the average current with a reduced gravity of 0.09 m/s^2 near the array of cylinders.

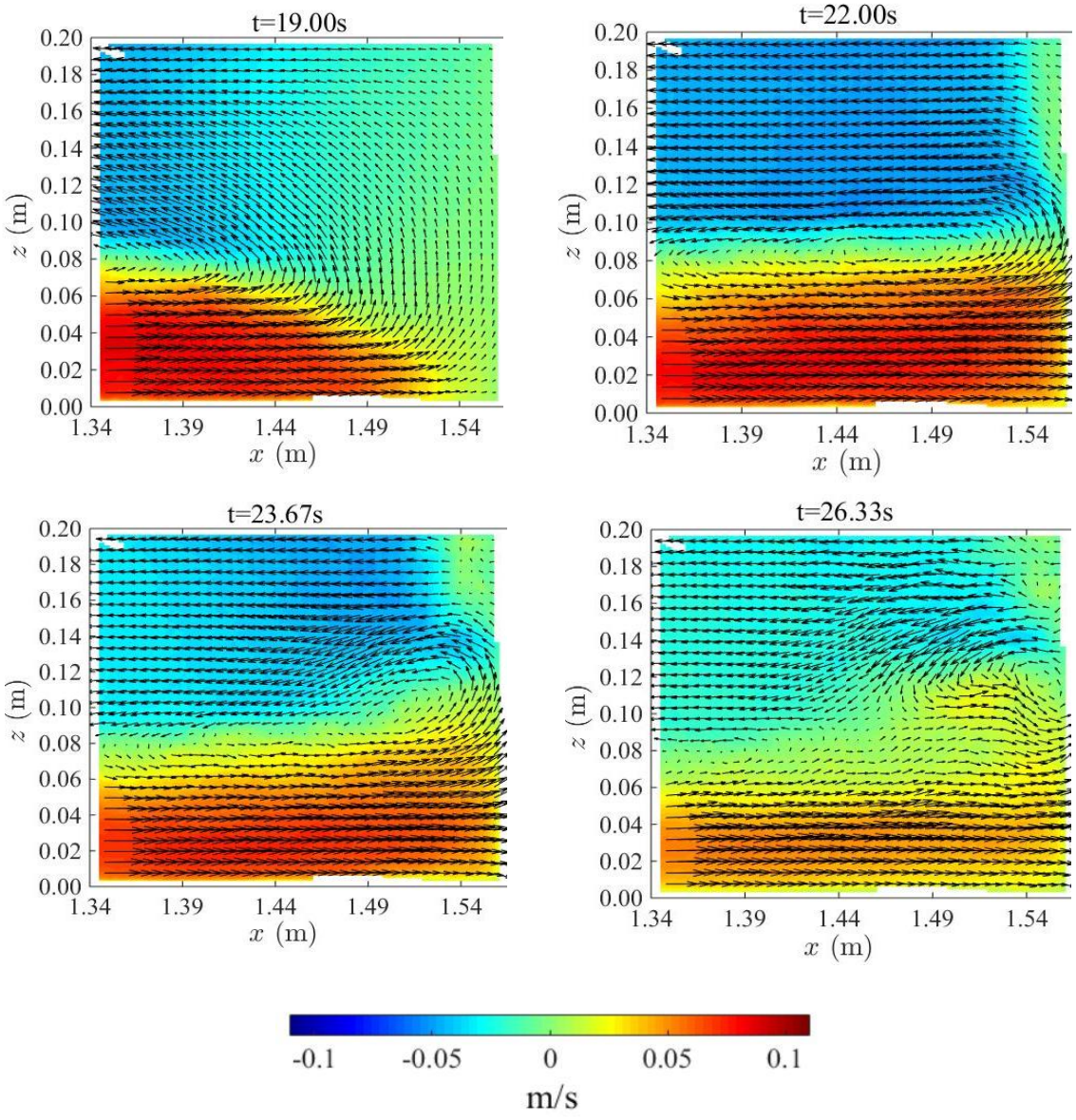

Figure 5.4: Sequence of velocity fields for the average current with $g' = 0.09\ \mathrm{m}/s^2$.

From the sequence of images is perceptible that at 22 seconds the current already hit the first row of cylinders since there is an increase in the current height after the 1.54 meters mark as the current starts to climb the cylinders wall. It is important to refer the red colour represents the velocity field for the denser current as the blue colour represents the variation of the ambient fluid velocity, the values are negative for the ambient fluid velocity because it moves from right to left contrary to the longitudinal axis.

Continuing the analysis, at 23.67 seconds is possible to see in the region near the cylinder, at a height of around 10 cm, an area of circulation with the formation of vortices as the denser current is mixing with the ambient fluid due to the impact of the cylinders. A similar phenomenon but with less intensity was observed in section 2.4 in the work of Mok et al.(2011) regarding the impact of density current with a vertical cylinder. After a few seconds in 26.33 *s* there is a reduction of velocity which marks the passage of the current body.

In Figure 5.5 is presented a sequence of images that represent the variation of the longitudinal velocity u in the current with a reduced gravity of 0.36 m/s^2.

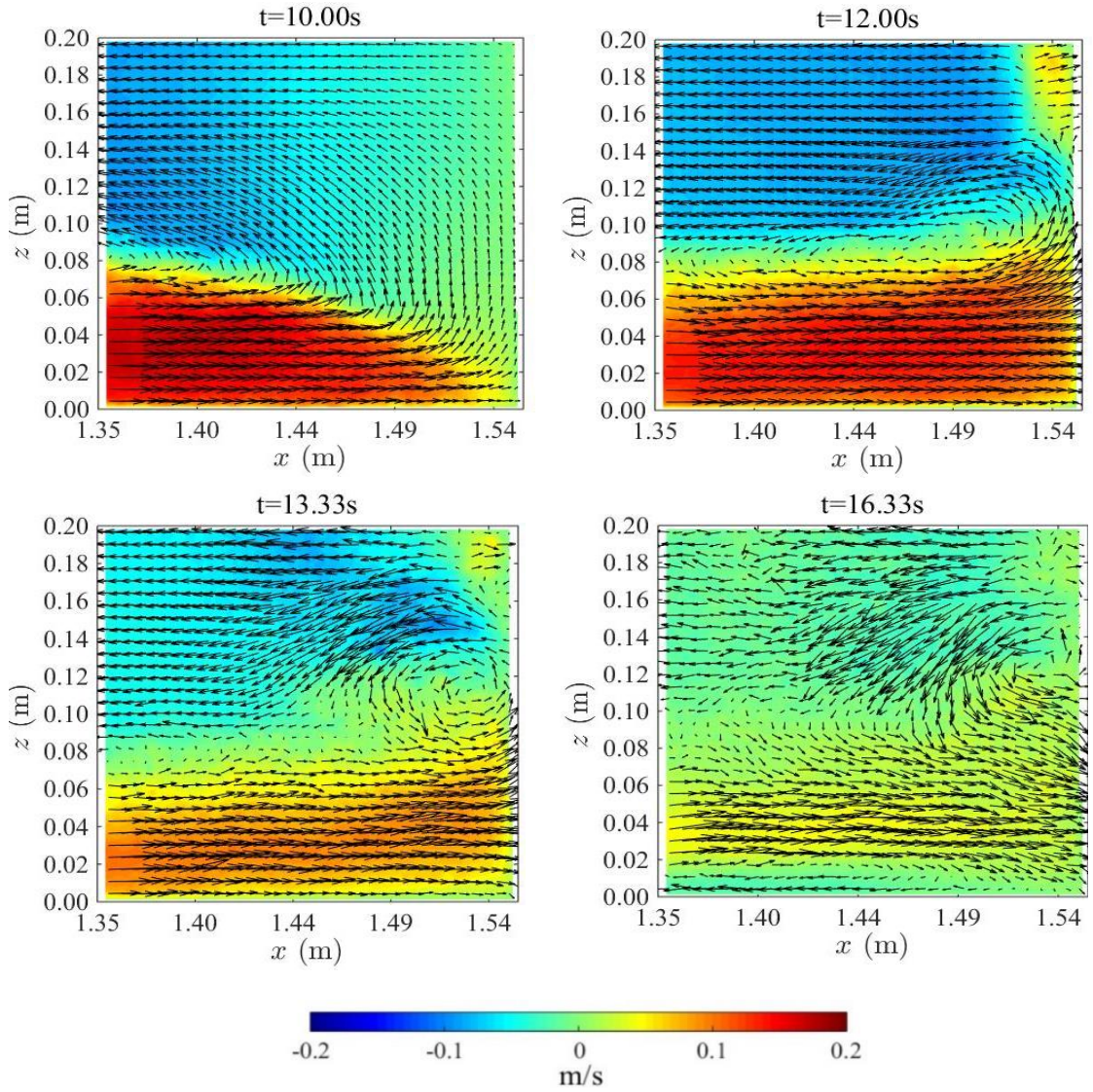

Figure 5.5: Sequence of velocity fields for the average current with $g' = 0.36\ \mathrm{m}/s^2$.

For the current with a reduced gravity of $g' = 0.36\ \mathrm{m}/s^2$ the behaviour of the current is similar, but the velocity magnitude is higher for this case as it reaches values of approximately 0.2 m/s, while for the current with a lower reduced gravity reaches 0.1 m/s.

At the 12 seconds is possible to see the circulation area with the vortices being created and it continues at 13.33 seconds with the area increasing in size.

At 16.33 seconds the velocity field presents lower values due to the presence of the current tail.

5.2.2 Plan view

For the plan view were made 20 repetitions with a reduced gravity of $0.09\ \mathrm{m}/s^2$. In ten of those repetitions the laser beam illuminates a plane at $z = 1.6\ cm$ while on the other ten repetitions the laser illuminated a plane at $z = 8\ cm$, seeing the top part of the current.

Figure 5.6 presents a sequence of images that represent the variation of the longitudinal velocity in the current with a reduced gravity of $0.09\ \mathrm{m}/s^2$ at the plane $z = 1.6\ cm$.

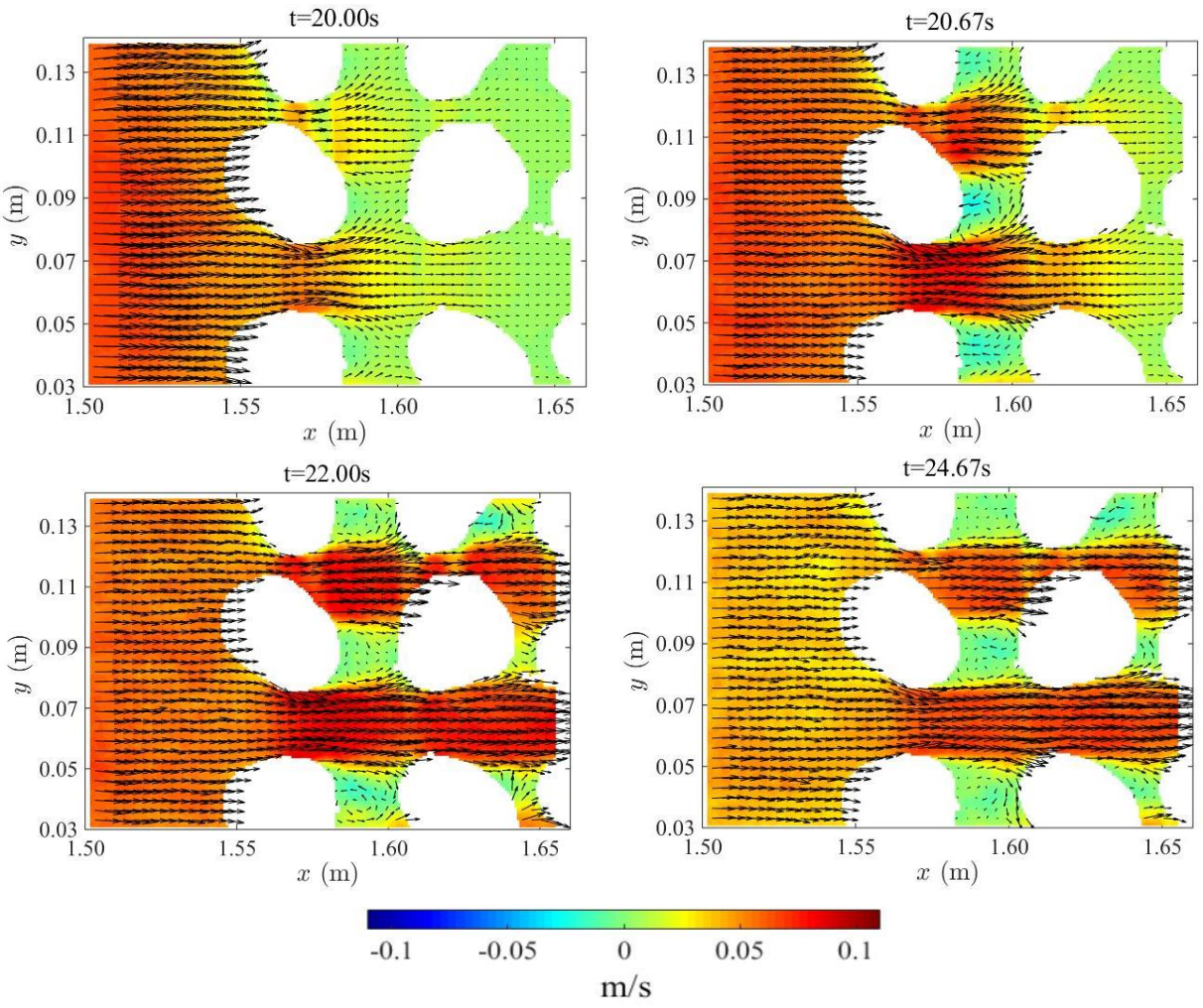

Figure 5.6: Sequence of velocity fields for the average current with $g' = 0.09\ \mathrm{m}/s^2$.

With the plan view is possible to analyse how the current propagates in the interspace of the cylinders. At 20 seconds the current is surpassing the first row of cylinders and at 20.67 seconds it arrives to the second row. Its already possible to see the velocity reaches it maximum in the side of the cylinders where the area is reduced.

At 22 seconds the current arrives to the third row of cylinders and starts to appear areas of recirculation behind the first row of cylinders, near the point $(1.60,0.04)\,m$. In the last frame at 24.67 seconds, there is a decrease in the velocity magnitude as the current front progresses to the other rows of cylinders, and the current of the current body begins to appear in the 1.50 meters.

In Figure 5.7 is presented a sequence of images showing the variation of the longitudinal velocity in the current with a reduced gravity of 0.09 m/s^2 at the plane $z = 8\,cm$.

.

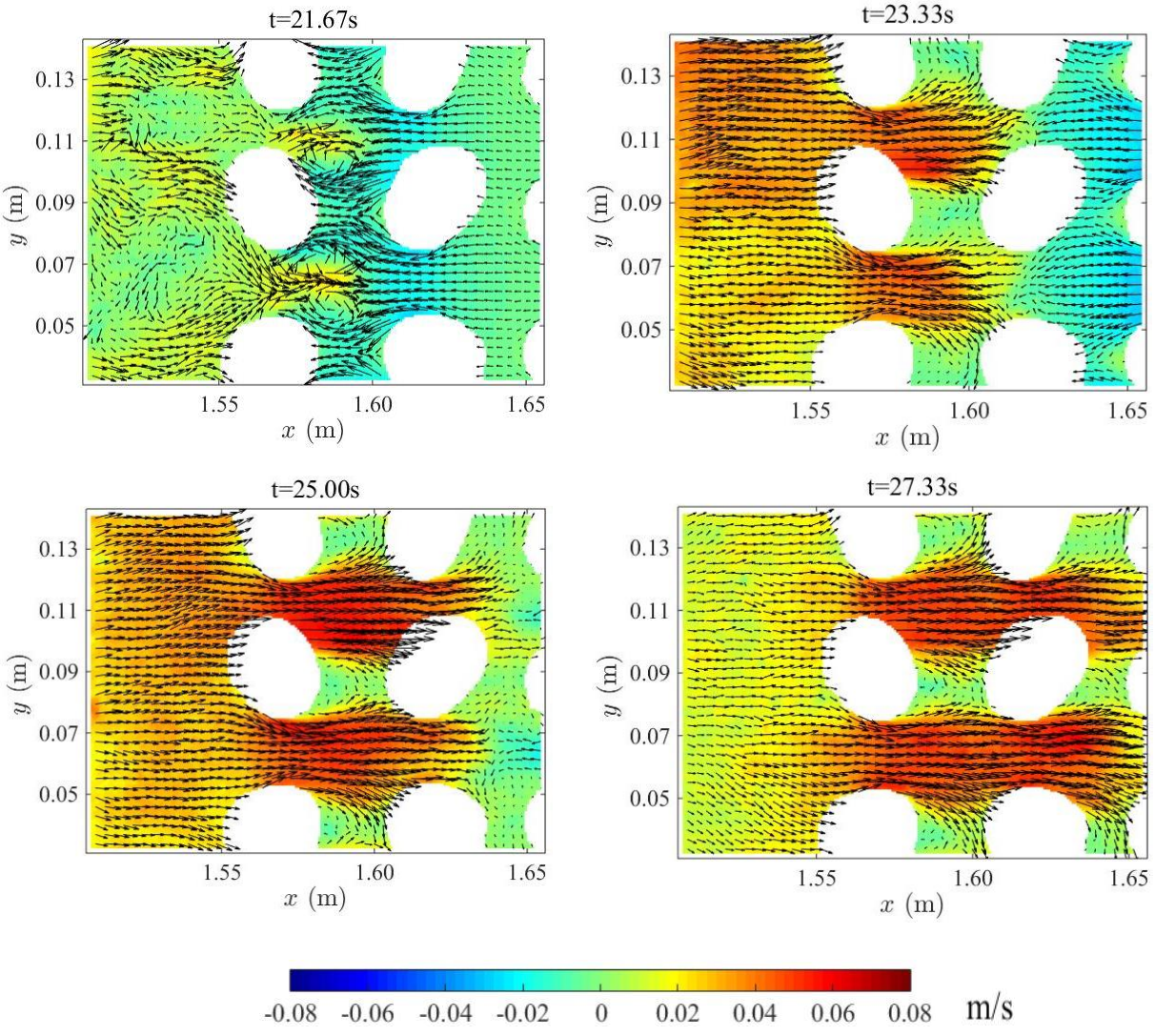

Figure 5.7: Sequence of velocity fields for the average current with $g' = 0.09\ \mathrm{m}/s^2$, in a plane of $z = 8\,cm$.

In this case the velocity magnitude is lower because the laser was placed at a different height which was illuminating the seeding particles at the top of the current.

In the first frame at 21.67 seconds is possible to observe in the space between the first row and the second some instability. Then as the time goes by the pattern is similar to the other analysed current in the plan view as the velocity magnitude reduces when the current head passes and the tail starts to show up.

5.3 Turbulence structures

In this sub-chapter are presented the results of the distribution of different order moments for the current head and tail obtained in the side view and plan view.

In the first section is going to be discussed the distribution of the ensemble average longitudinal velocity. The second section is dedicated to the analysis of the second order moment which correspond to the Reynolds stress and in the third section is going to be discussed the third order moment correspondent to the component of the turbulent transport.

5.3.1 First order moment (Ensemble average)

In the following sections, is going to be made a comparison between the case where the array of cylinders was placed and when one isolated cylinder was placed in the channel. For the measurements taken in the side view related to the head, is also introduced the case without obstacles in the channel to have a complete sequence of the impact of the cylinders. While the density currents analysed in the array had a reduced gravity of $0.09\ \mathrm{m}/s^2$ and $0.36\ \mathrm{m}/s^2$, for the isolated cylinder and without obstacles they had $0.06\ \mathrm{m}/s^2$ and $0.24\ \mathrm{m}/s^2$.

For a better understanding of the cases where the comparison between the three scenarios is made, the title given in each image correspond to:

- Letter (a) are the images for $g' = 0.09\ \mathrm{m}/s^2$ in the array.
- Letter (b) are the images for $g' = 0.06\ \mathrm{m}/s^2$ for isolated cylinder
- Letter (c) are the images for $g' = 0.06\ \mathrm{m}/s^2$ without obstacles.
- Letter (d) are the images for $g' = 0.36\ \mathrm{m}/s^2$ in the array.
- Letter (e) are the images for $g' = 0.24\ \mathrm{m}/s^2$ for isolated cylinder.
- Letter (f) are the images for $g' = 0.24\ \mathrm{m}/s^2$ without obstacles.

In Figure 5.8 is presented the images for the first order moment ($\bar{u}$) distribution in the head.

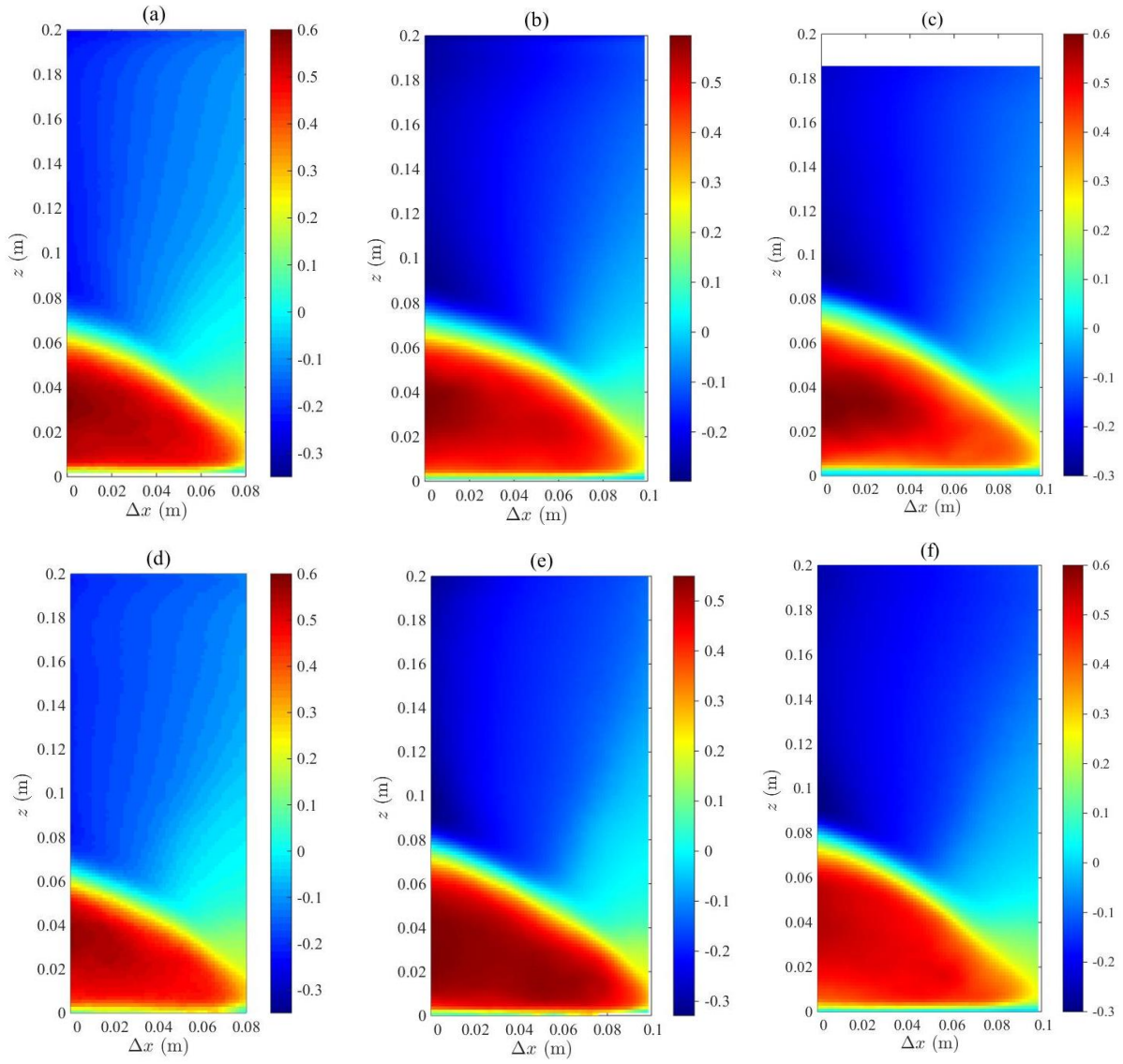

Figure 5.8: First order moment ($\bar{u}$) in the head for: (a) $g' = 0.09\ \mathrm{m}/s^2$ in the array; (b) $g' = 0.06\ \mathrm{m}/s^2$ isolated cylinder; (c) $g' = 0.06\ \mathrm{m}/s^2$ without obstacles; (d) $g' = 0.36\ \mathrm{m}/s^2$ in the array; (e) $g' = 0.24\ \mathrm{m}/s^2$ isolated cylinder; (f) $g' = 0.24\ \mathrm{m}/s^2$ without obstacles.

By comparing the different images is possible to see a similar pattern in the ensemble average distribution for the three cases analysed, so the presence of obstacles seems to have no influence in the mean flow of the head. The part with high positive values characterizes the current head, which is the place where the velocities are higher, while the blue part with a negative magnitude is the ambient fluid movement.

Figure 5.9 shows the images for the first order moment ($\bar{u}$) distribution in the tail.

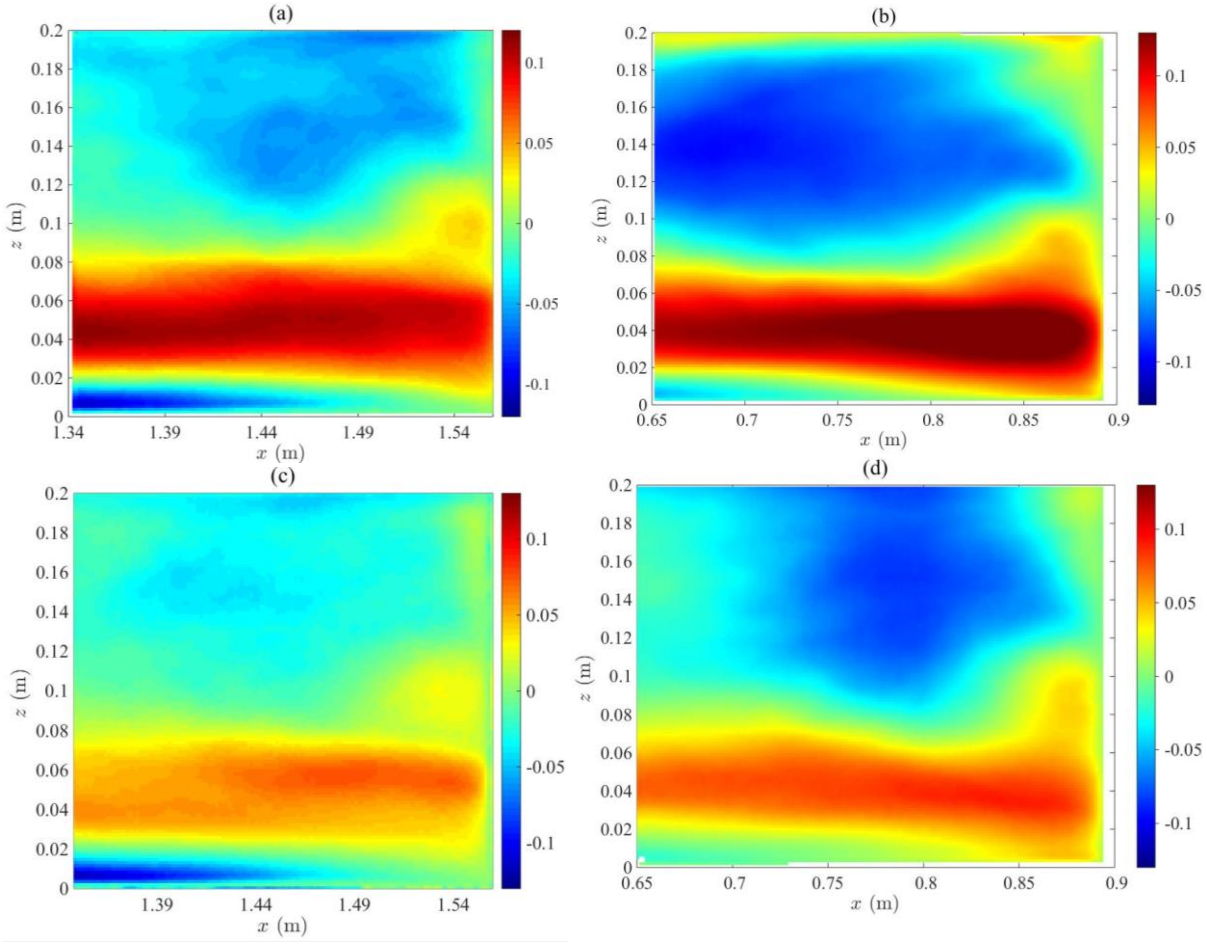

Figure 5.9: First order moment ($\bar{u}$) in the tail for: (a) $g' = 0.09\ \mathrm{m}/s^2$ in the array; (b) $g' = 0.06\ \mathrm{m}/s^2$ for isolated cylinder; (c) $g' = 0.36\ \mathrm{m}/s^2$ in the array; (d) $g' = 0.24\ \mathrm{m}/s^2$ for isolated cylinder

Is possible to see in Figure 5.9 the array of cylinders has a minor influence in the mean velocity if compared to the isolated cylinder. There is a small reduction in the longitudinal velocity of the denser current, which is caused by the generated pressure field induced by the cylinders. For the tail, the currents with a lower value of reduced gravity have a higher value for the first order moment in the tail section, as shown in the red part, with a magnitude of around 0.1. As expected, these values are lower to the ones obtained for the current head, seen in Figure 5.8.

In figures Figure 5.10 and Figure 5.11 are made the analyses for the head and tail behaviour with the current being recorded in the plan view.

In Figure 5.10 are presented the first order moment ($\bar{u}$) distribution in the head, measured in the plan view.

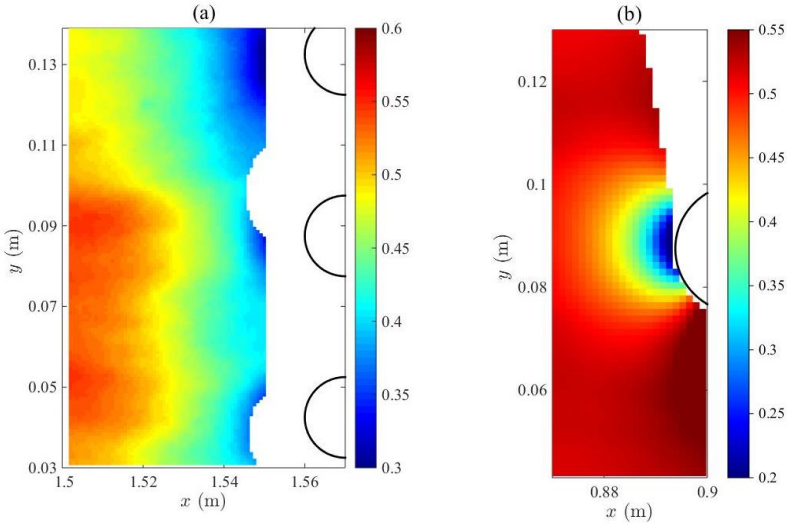

Figure 5.10: First order moment ($\bar{u}$) in the head for: (a) $g' = 0.09\ \mathrm{m}/s^2$ in the array; (b) $g' = 0.06\ \mathrm{m}/s^2$ isolated cylinder.

In Figure 5.10 (a) is marked with circular black lines the position of the first row of cylinders in the channel. Near the 1.54 m mark are two semi-circular white areas that correspond to the beginning of the cylinders shadow caused by the placement of the recording camera. This shadow made impossible to see the flow in the area right next to the cylinders wall.

In Figure 5.10 (b) the pressure field induced by the cylinder is felt behind the obstacle, generating a longitudinal velocity gradient that is confined in the proximity of the cylinder. In Figure 5.10 (a) the pressure field is also felt behind the cylinders, but the longitudinal velocity gradient is spread in the field of view due to the presence of more obstacles.

In Figure 5.11 is presented the images for the first order moment ($\bar{u}$) in the tail.

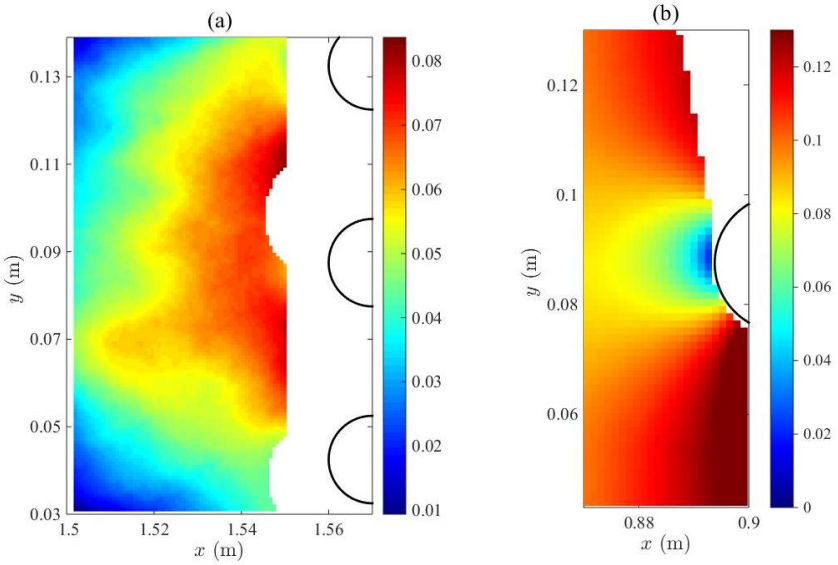

Figure 5.11: First order moment ($\bar{u}$) in the tail for: (a) $g' = 0.09\ \mathrm{m}/s^2$ in the array; (b) $g' = 0.06\ \mathrm{m}/s^2$ for isolated cylinder.

In the tail, Figure 5.11 (a) presents the velocity has a higher value in the region close to the cylinders particularly in the space between them. In Figure 5.11 (b) the velocity gradient is spread laterally, affecting the longitudinal velocity to the sides of the isolated cylinder.

The variation of the transversal mean velocity ($\bar{v}$) of the current head in the array, Figure 5.12 (a), shows there are stagnation points in the direction of the cylinders, with a positive value of transversal velocities in the upper part and negative ones in the lower part, but since is not possible to analyse the flow right next to the cylinder wall (due to the shadow), the analysis of the stagnation point is complex. In Figure 5.12 (b) the stagnation point is visible in the isolated cylinder and there is a quasi-symmetrical section characterized with positive values of ($\bar{v}$) in the upper part and negative in the lower part. This quasi-symmetrical part is difficult to identify in the array of cylinders due to the presence of more obstacles which makes the flow path more complex.

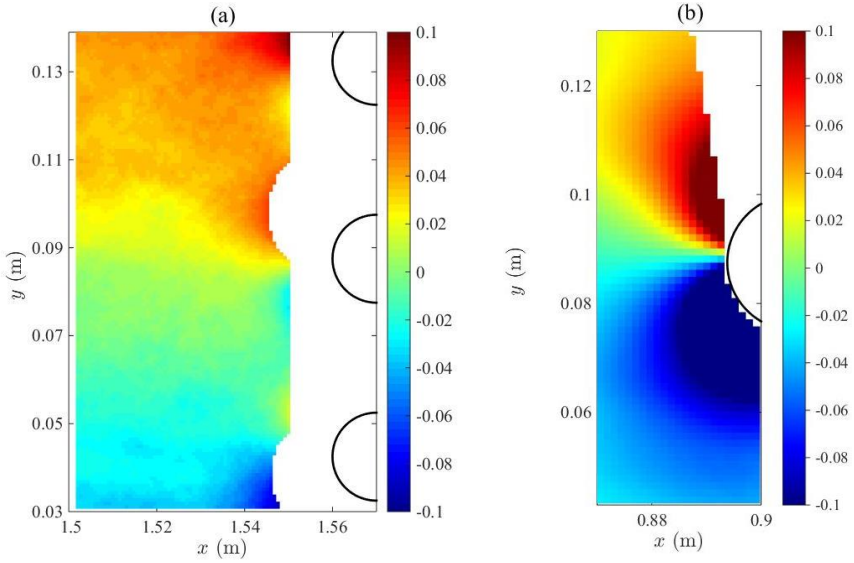

Figure 5.12: First order moment (v) in the head for: (a) $g' = 0.09\ \mathrm{m}/s^2$ in the array; (b) $g' = 0.06\ \mathrm{m}/s^2$ isolated cylinder.

5.3.2 Second order moments (Reynolds stress)

In this work were obtained the components of the Reynolds stress which correspond to the second order moments. Since the measurements carried out in this work were two-dimensional, the Reynolds components evaluated for the side view are ($\overline{u'u'}$), ($\overline{u'w'}$) and ($\overline{w'w'}$), while in the plane view are ($\overline{u'u'}$), ($\overline{v'v'}$) and ($\overline{u'v'}$).

A discussion on the behaviour of the Reynolds shear stress ($\overline{u'w'}$) and ($\overline{u'v'}$) is going to be made in the following section.

Figure 5.13 presents the images for the second order moment ($\overline{u'w'}$) distribution in the head.

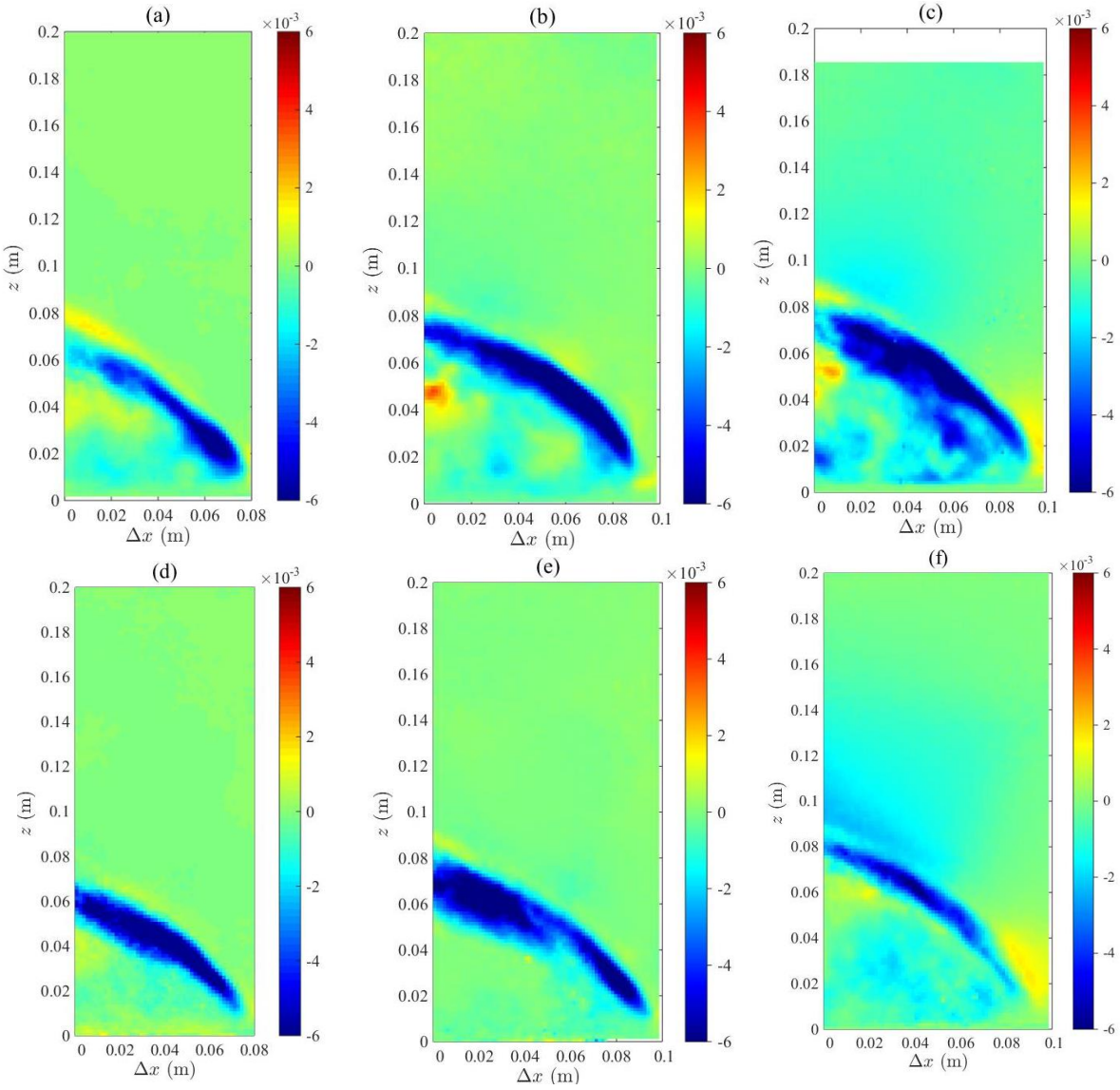

Figure 5.13: Second order moment ($\overline{u'w'}$) in the head for: (a) $g' = 0.09\ \mathrm{m}/s^2$ in the array; (b) $g' = 0.06\ \mathrm{m}/s^2$ isolated cylinder; (c) $g' = 0.06\ \mathrm{m}/s^2$ without obstacles; (d) $g' = 0.36\ \mathrm{m}/s^2$ in the array; (e) $g' = 0.24\ \mathrm{m}/s^2$ isolated cylinder; (f) $g' = 0.24\ \mathrm{m}/s^2$ without obstacles.

The areas with a higher magnitude of shear stress are the blue parts. This area is the interface zone between the denser current and the ambient fluid. The pressure field generated by the cylinders reduce the intensity of the shear stress in the head, relegating it to the interface between the two fluids. In Figure 5.13 (a) to (c) is possible to see the transition of the shear stress from the head to the interface area between the two fluids as more obstacles are placed in the channel.

Figure 5.14 shows the images for the second order moment ($\overline{u'w'}$) in the tail.

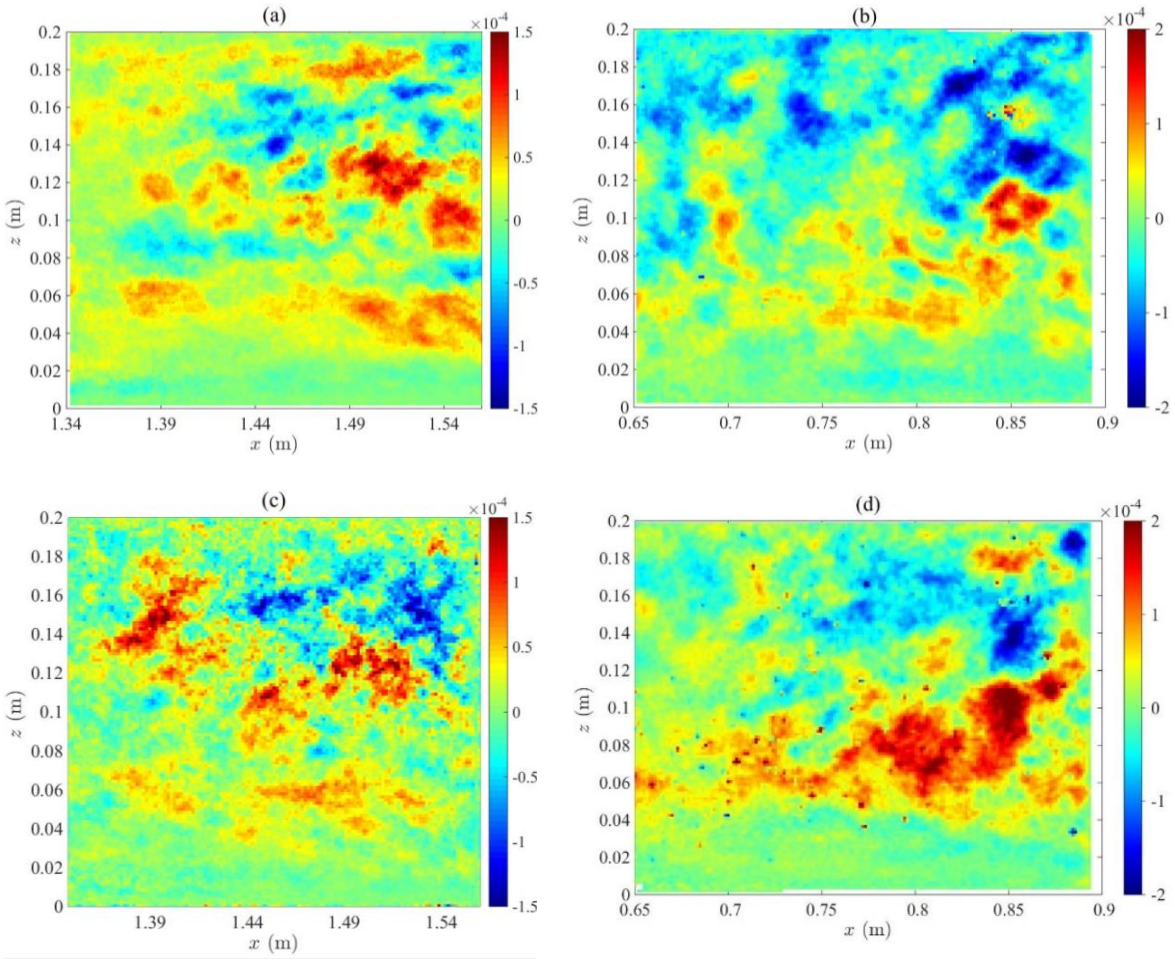

Figure 5.14: Second order moment ($\overline{u'w'}$) in the tail for: (a) $g' = 0.09\ \mathrm{m}/s^2$ in the array; (b) $g' = 0.06\ \mathrm{m}/s^2$ isolated cylinder; (c) $g' = 0.36\ \mathrm{m}/s^2$ in the array; (d) $g' = 0.24\ \mathrm{m}/s^2$ isolated cylinder

The magnitude of the shear stress values for the tail decreased significantly if compared to the head in all currents. The pattern of the shear stress is different in two cases since for the case with the isolated cylinder there is positive-negative dipole compatible with a big vortice in the mixing layer area, close to the cylinder, due to an adverse pressure gradient.

The difference in the pattern of the shear stress can be explained by a phenomenon observed in the current with help of the maps of instantaneous velocity obtained in experimental and numeric work.

The obstruction of the flow created by the array of cylinders is much higher than the obstruction created by the isolated cylinder. While with the isolated cylinder the flow is mostly bi-dimensional, with the array of cylinders the flow still has a bi-dimensional component but is also induced a strong three-dimensional component (vertical) due to the interaction with the cylinders. The obstruction created by the cylinders generates a wave that propagates upstream.

Near the bottom is the passage of an unsteady current but from $z = 7\ cm$ the flow is dominated by a robust structure marked by a strong tri dimensional turbulence that is statistically almost steady.

What is seen in Figure 5.14 (a) and (c) is a set of structures dominated by a large circulation that articulates the return flow of the ambient fluid and the flow of the dense current. The flow has strong three-dimensional disturbances because the flow cannot enter the space between cylinders without forming vertical structures.

In Figure 5.15 is presented the images for the Reynolds shear stress ($\overline{u'v'}$) in the head for the plan view.

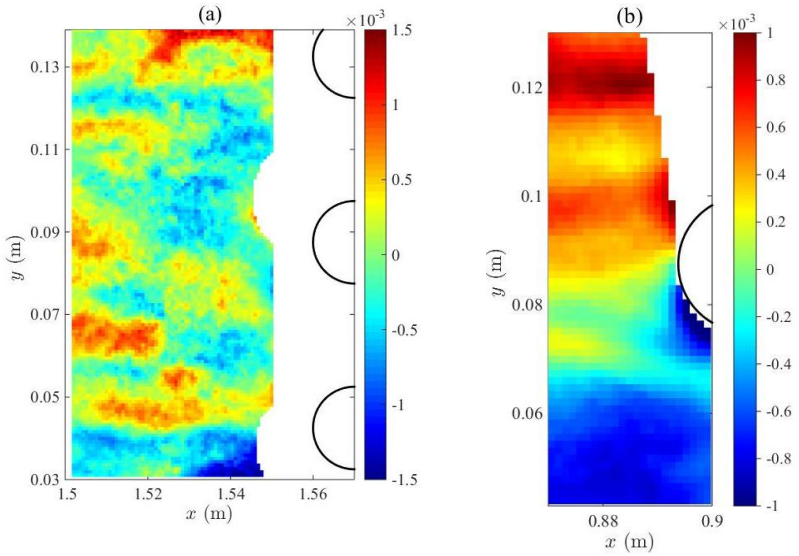

Figure 5.15: Second order moment ($\overline{u'v'}$) in the head for: (a) $g' = 0.09\ \mathrm{m}/s^2$ in the array; (b) $g' = 0.06\ \mathrm{m}/s^2$ isolated cylinder;

Figure 5.15 shows the magnitude of the shear stress is identical in both cases. The variation is different mostly due to the reasons presented above. The induced three-dimensional component in the flow by the array of cylinders adds more complexity to the flow, particularly in the approximation area of the array, which is seen in the plan view, creating a destruction of the values coherence in that particular area. In the case with the isolated cylinder the shear stress is null near the cylinder, green area where the stagnation point is presented and shows a symmetrical behaviour with positive values in the upper part and negative one in the lower part, which goes along with the predominant bi-dimensional behaviour of the flow in the presence of the isolated cylinder.

Figure 5.16 shows the images for the Reynolds shear stress ($\overline{u'v'}$) distribution in the tail.

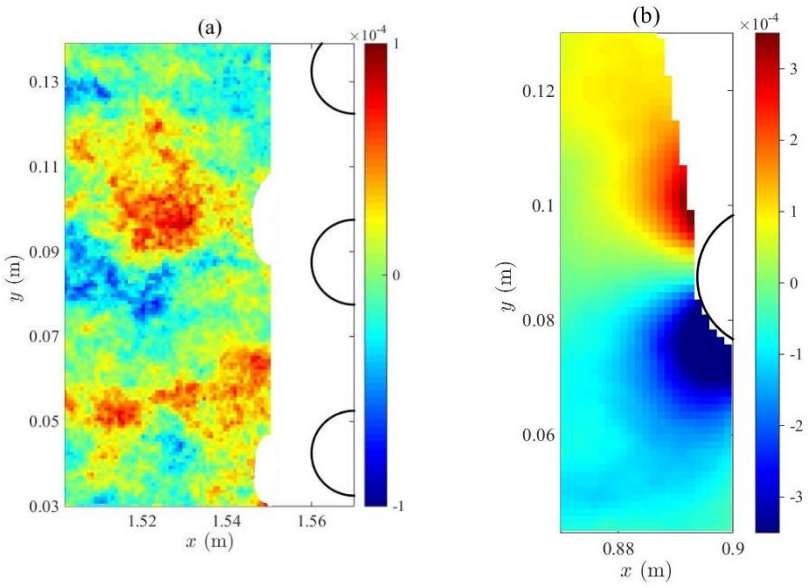

Figure 5.16: Second order moment $(\overline{u'v'})$ in the tail for: (a) $g' = 0.09\ \mathrm{m}/s^2$ in the array; (b) $g' = 0.06\ \mathrm{m}/s^2$ isolated cylinder.

In Figure 5.16 (a) is shown the same destruction of coherence for the shear stress values observed in Figure 5.15 (a) for the head. In the tail there are some areas with a high intensity of shear stress that can be related to the tri dimensional flow which creates helicoidal vortices around the cylinders and will develop into the area between them.

Figure 5.16 (b) shows the shear stress in the tail follows a similar behaviour to the observed in Figure 5.15 (b) for the head but while in the head the diffusion was not homogeneous, in the tail shows a more constant lateral gradient.

5.3.3 Third order moments (turbulent transport)

The third order moments are the components of the turbulent transport. These components explain how the energy extracted by the normal Reynolds stresses is redistributed in the longitudinal, transversal, and lateral direction.

The components evaluated for the side view are $(\overline{u'u'u'})$, $(\overline{u'u'w'})$, $(\overline{u'w'w'})$ and $(\overline{w'w'w'})$ while in the plane view are $(\overline{u'u'u'})$, $(\overline{u'u'v'})$, $(\overline{u'v'v'})$ and $(\overline{v'v'v'})$.

A discussion on the behaviour of the component $(\overline{u'u'u'})$, is going to be made in the following section.

Figure 5.17 presents the images for the third order moment ($\overline{u'u'u'}$) distribution related to the head.

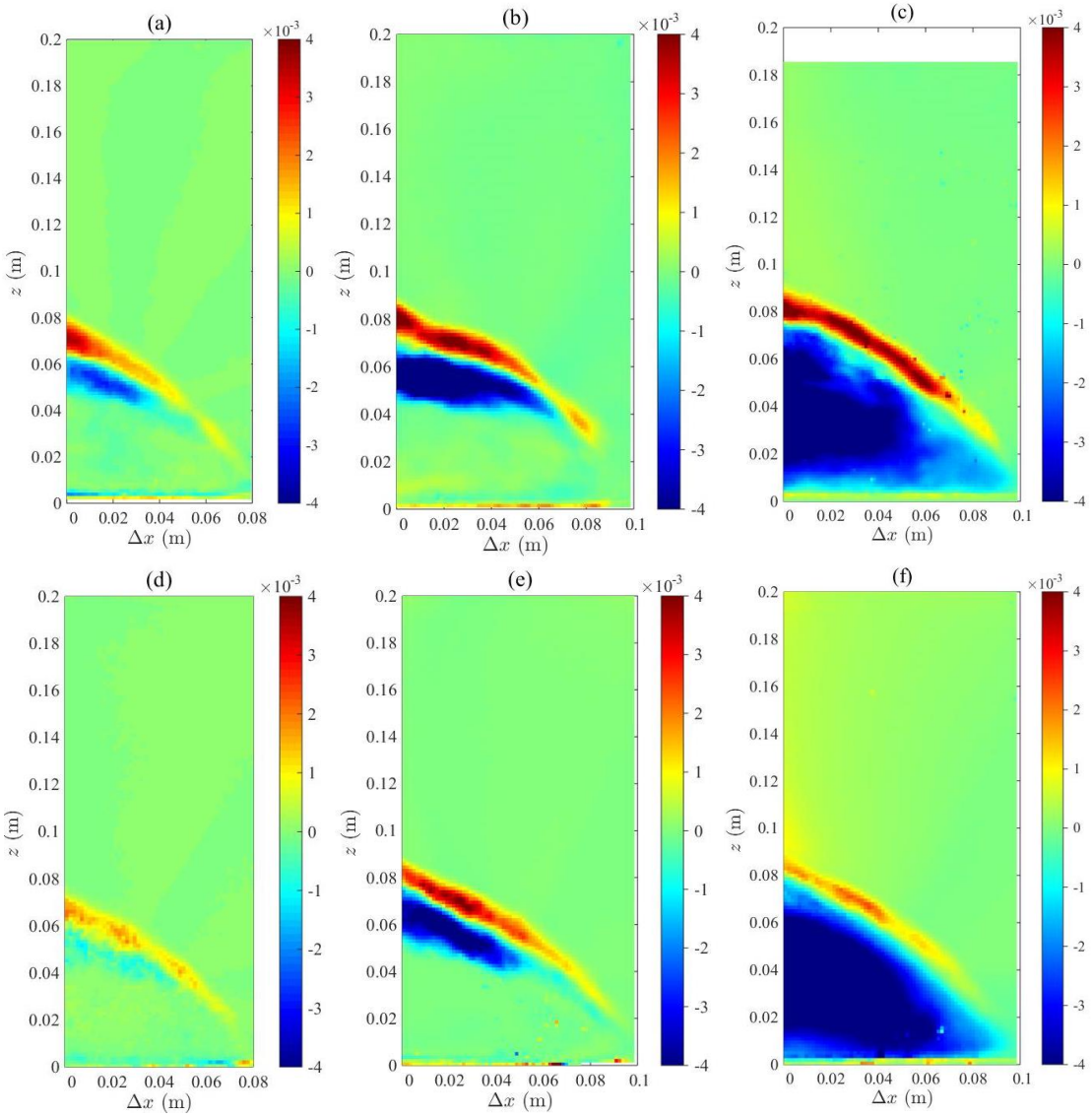

Figure 5.17: Third order moment ($\overline{u'u'u'}$) in the head for: (a) $g' = 0.09\ \mathrm{m}/s^2$ in the array; (b) $g' = 0.06\ \mathrm{m}/s^2$ isolated cylinder; (c) $g' = 0.06\ \mathrm{m}/s^2$ without obstacles; (d) $g' = 0.36\ \mathrm{m}/s^2$ in the array; (e) $g' = 0.24\ \mathrm{m}/s^2$ isolated cylinder; (f) $g' = 0.24\ \mathrm{m}/s^2$ without obstacles.

Figure 5.17 shows for the current without obstacles a large area with negative diffuse transport in the denser current head. The pressure field induced by the cylinder supresses the longitudinal transport of the longitudinal Reynolds stress inside the head, relegating it to the interface between the fluids, with positive values above the interface and negative ones below. With the array of cylinders this suppression is higher compared to the case with the isolated cylinder which corroborates the presence of a higher pressure field induced by the array.

The red and orange area with positive values, is the region where the turbulent tensions are being transported in the current direction, so there is energy addition to the average flow. In the blue area the tensions are being transported in a opposite direction to the current which means energy is being taken away from the average flow.

In Figure 5.18 is presented the third order moment ($\overline{u'u'u'}$) distribution related to the tail.

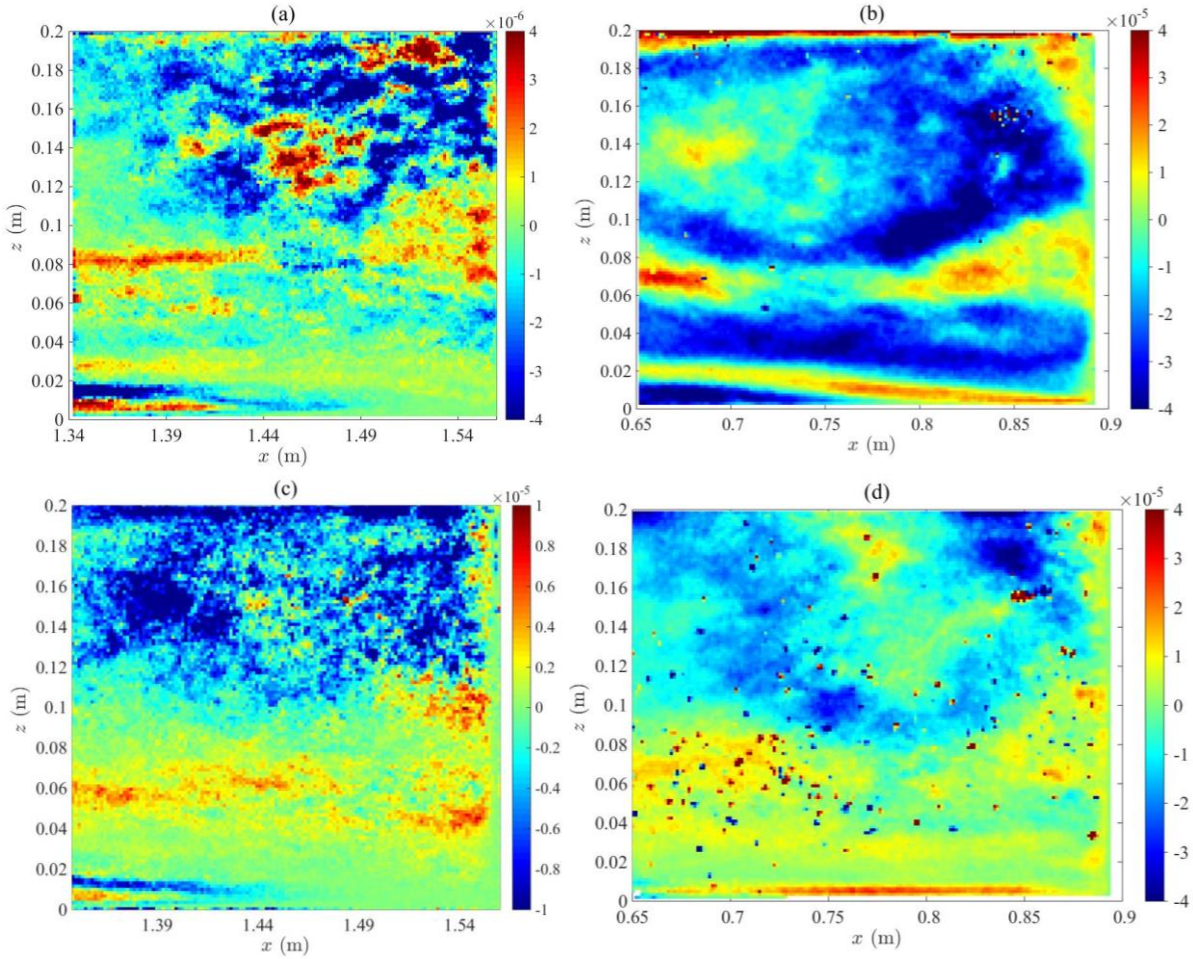

Figure 5.18: Third order moment ($\overline{u'u'u'}$) in the tail for: (a) $g' = 0.09\ \mathrm{m}/s^2$ in the array; (b) $g' = 0.06\ \mathrm{m}/s^2$ isolated cylinder; (c) $g' = 0.36\ \mathrm{m}/s^2$ in the array; (d) $g' = 0.24\ \mathrm{m}/s^2$ isolated cylinder.

For the third order moments there is a significant decrease in the turbulent intensity values for the current with $g' = 0.09\ \mathrm{m}/s^2$ in the array since the magnitude is 10^{-6},while for the isolated cylinder this magnitude is 10^{-5}.

In front of the isolated cylinder there are alternate zones of positive and negative values that can be explained by some circulation generated by the interaction between the current and the cylinder. Figure 5.18 (a) and (c) shows with the array of cylinders this behaviour is more evident as the circulation phenomenon is more intense due to the induced vertical component in the flow caused by the interaction with the different obstacles.

In Figure 5.19 is presented the images for the third order moment $(\overline{u'u'u'})$ in the head for the plan view.

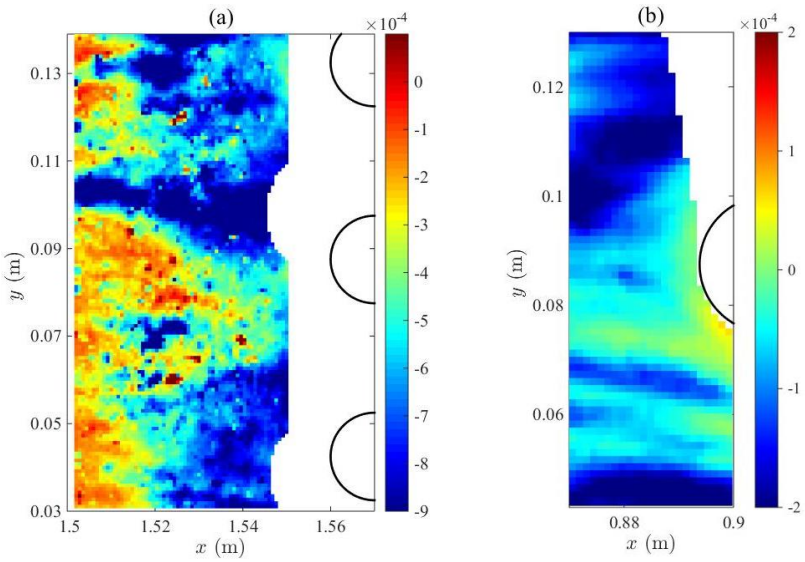

Figure 5.19: Third order moment $(\overline{u'u'u'})$ in the head for: (a) $g' = 0.09\ \mathrm{m}/s^2$ in the array; (b) $g' = 0.06\ \mathrm{m}/s^2$ isolated cylinder.

Figure 5.19 (b) shows the value of the longitudinal transport of the longitudinal Reynolds stress in the head is close to zero in the cylinder direction and along the surface. In Figure 5.19 (a) there is not a coherence in the values distribution due to the complex tri dimensional structure with high turbulence caused by the array of cylinders.

Figure 5.20 shows the images for the third order moment $(\overline{u'u'u'})$ distribution in the tail for the plan view.

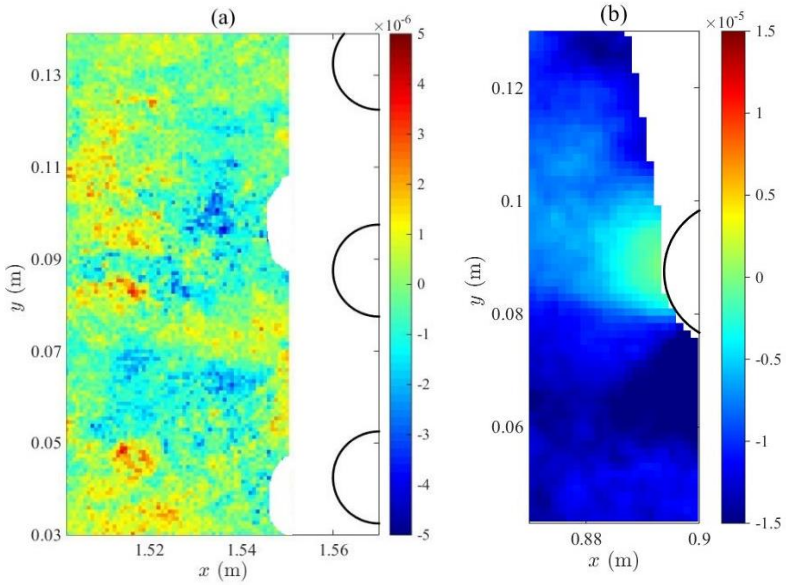

Figure 5.20: Third order moment $(\overline{u'u'u'})$ in the tail for: (a) $g' = 0.09\ \mathrm{m}/s^2$ in the array; (b) $g' = 0.06\ \mathrm{m}/s^2$ isolated cylinder.

In Figure 5.20 (a) the variation of the third order moment in the tail do not follow a defined pattern. The inexistence of coherence follows what was observed in Figure 5.19 (a) for the head. In Figure 5.20 (b) there is a defined structure, with a value of approximately zero in front of the cylinder and minimum values in the region next to the cylinder shown in the dark blue area.

In Appendix 6 to 11 are presented the images of the distribution of the different order moments in the array that were not discussed in this chapter.

6 Conclusions and future work

6.1 Main conclusions

In this dissertation the effect of an array of vertical cylinders on the structure of density currents was experimentally studied. For this purpose, tests were conducted with the "full depth lock-exchange" configuration. First, were performed tests using the PIV technique to obtain the 2D velocity field measurements for the current in the approximation of the array of cylinders. Then, were performed tests using the image analysis technique to obtain a general view of the current in all the channel length. The tests were performed for two different values of reduced gravity: $0.09\ \mathrm{m}/s^2$ and $0.36\ \mathrm{m}/s^2$. For each value of reduced gravity were made ten repetitions. For the PIV technique the current was recorded in the side view and plan view, while using the image analyses technique only the side view of the current was recorded.

Regarding the results obtained by the image analyses technique, it was observed for the currents produced by a smaller difference of densities the repeatability of the tests was harder to obtain. This can be explained by the low inertia forces presented in currents with a low value of reduced gravity.

For the macroscopic variables (front position and current height) the difference in density between the fluids did not introduce significant changes to the current but the impact with the array of cylinders was relevant as the current suffer a loss of speed in the array due to the impact and the front position did not vary linearly. As for the current height it increases in the region of impact with the first row of cylinders but as the current encounters the following rows it significantly decreases his size if compared to what happened without any obstacle.

It is possible to conclude when the current faces obstacles it restructures macroscopically, gains potential energy in a first stage but then loses total energy.

As for the microscopic variable (entrainment), it was found an increase in the value as the current advanced in the channel, until reaching the array of cylinders. After a few seconds in the array, the entrainment value kept constant until the end of the experiment (current hits the limit wall of the channel). This can be explained by the lack of kinetic energy to promote the mixing due to the presence of the array of cylinders, which means the drag in the array do not contribute to a continuous increase of the entrainment.

Regarding the results obtained for the PIV tests some considerations can be made. By the analyses of the velocity fields, the introduction of the array of cylinders in the current increases the mixing processes in the impact area of the first row of cylinders, creating a large recirculation area by the formation of vortices in the flow. This phenomenon was observed for the currents with different reduced gravities.

For the study of the turbulence was made a comparison of the results regarding the interaction of the current with the array of cylinders and the case where one isolated cylinder was placed in the channel. For the analysis in the side view of the current head, the case without any obstacles in the channel was also discussed.

Regarding the first order moments was found a similarity in the pattern of the ensemble average velocities distribution in the current head, so the presence of the obstacles seems to have no influence in the mean flow of the head. In the tail was found the array of cylinders have some influence in the reduction of the tail mean velocity caused by a higher-pressure field induced by the cylinders.

The analysis of the second order moments (Reynolds stress) and the third order moments (turbulent transport) for the case with the array showed significant differences to what was obtained for the isolated cylinder. The obstruction of the flow created by the array of cylinders is much higher than the obstruction created by the isolated cylinder. While with the isolated cylinder the flow is mostly bi-dimensional, with the array of cylinders the flow has a bi-dimensional component but is also induced a strong three-dimensional component (vertical) due to the interaction with the cylinders. This obstruction created by the cylinders generates a wave that propagates upstream. While analysing the second order moments was observed a set of structures with hight turbulence dominated by a large circulation that articulates the return flow of the ambient fluid and the flow of the denser current. The flow creates these three-dimensional disturbances because it cannot enter the space between cylinders without forming vertical structures.

6.2 Suggestions for future work

This study presented a characterization of the behaviour of density currents in the presence of obstacles which simulated submersed vegetation.

Several ways to follow up on this work arise. Firstly, should be tried to place the array of cylinders near the lock position to assess the impact of the vegetation in the density current formation. With this configuration the best way to analyse the current should be with the image analyses technique because while using the PIV technique in the array was found impossible to see the flow between the cylinders using the side view due to the reflection of the laser light in the cylinders which created a shadow. So, without any technology improvement or dramatic change in the setup, the PIV technique is useless for the new configuration.

It would be interesting to study the effect of wind in the propagation of density currents since it is a meteorological phenomenon that affects the propagation of flows near the surface. It is also recommended to increase the number of repetitions made for each current, since obtaining more data helps to improve the results of the statistical approach of turbulence.

The study of density currents needs a continuous investigation since there are more parameters to analyse. This phenomenon is transversal to several branches of science and in a direct or indirect way, influences the environment that surround us and will condition our present and future.

References

Adduce, C., Sciortino, G., & Proietti, S. (2012). Gravity Currents Produced by Lock Exchanges: Experiments and Simulations with a Two-Layer Shallow-Water Model with Entrainment. *Journal of Hydraulic Engineering*, *138*(2), 111–121.

Brito, M., Sanches, P., Ferreira, R. M. L., & Covas, D. I. C. (2017). Experimental Study of the Transient Flow in a Coiled Pipe Using PIV. *Journal of Hydraulic Engineering*, *143*(3), 04016087.

Cenedese, C., & Adduce, C. (2010). A new parameterization for entrainment in overflows. *Journal of Physical Oceanography*, *40*(8), 1835–1850.

Daviero, G. J., Roberts, P. J. W., & Maile, K. (2001). Refractive index matching in large-scale stratified experiments. *Experiments in Fluids*, *31*(2), 119–126.

Ellison, T. H., & Turner, J. S. (1959). Turbulent entrainment in stratified flows. *Journal of Fluid Mechanics*, *6*(3), 423–448.

Ferreira, R. M. L. (2011). Turbulent Flow Hydrodynamics and Sediment Transport: Laboratory Research with LDA and PIV. *GeoPlanet: Earth and Planetary Sciences*, *1*, 67–111.

Filipe, N., & Silvestre, G. (2016). *The structure of gravity currents propagating in finite domains Civil Engineering*. *July*.

Huppert, H. E., & Simpson, J. E. (1980). The slumping of gravity currents. *Journal of Fluid Mechanics*, *99*(4), 785–799.

Isabel, H., & Nogueira, S. (2013). *EXPERIMENTAL CHARACTERIZATION OF UNSTEADY GRAVITY CURRENTS DEVELOPING OVER SMOOTH AND ROUGH BEDS*.

Ljungkrona, L., & Sundén, B. (1993). Flow visualization and surface pressure measurement on two tubes in an inline arrangement. *Experimental Thermal and Fluid Science*, *6*(1), 15–27.

Mok, K. M., Leong, C. S., Hoi, K. I., & Yeh, H. H. (2011). The impact of a gravity current with a vertically mounted circular cylinder: An experimental study. *2011 IEEE 3rd International Conference on Communication Software and Networks, ICCSN 2011*, 194–198.

Nogueira, H. I. S., Adduce, C., Alves, E., & Franca, M. J. (2014). Dynamics of the head of gravity currents. *Environmental Fluid Mechanics*, *14*(2), 519–540.

Ozan, A. Y., Constantinescu, G., & Hogg, A. J. (2015). Lock-exchange gravity currents propagating in a channel containing an array of obstacles. *Journal of Fluid Mechanics*, *765*, 544–575.

Parker, G., Garcia, M., Fukushima, Y., & Yu, W. (1987). Etude expérimental de courants de turbidité sur un lit affouillable. *Journal of Hydraulic Research*, *25*(1), 123–147.

Raffel, M., Willert, C. E., Wereley, S. T., & Kompenhans, J. (2007). *Particle Image Velocimetry*.

Ricardo, A. M., Franca, M. J., & Ferreira, R. M. L. (2013). Caracterização do escoamento turbulento em canais com vegetação emersa rígida. *Revista Recursos Hídricos*, *34*(2), 55–67.

Ricardo, A. M., Koll, K., Franca, M. J., Schleiss, A. J., & Ferreira, R. M. L. (2014). The terms of turbulent kinetic energy budget within random arrays of emergent cylinders. *Water Resources Research*, *50*(5), 4131–4148. 6

Rottman, J. W., & Simpson, J. E. (1983). Gravity currents produced by instantaneous releases of a heavy fluid in a rectangular channel. *Journal of Fluid Mechanics*, *135*, 95–110.

Simpson, J. E. (1982). Gravity currents in the laboratory, atmosphere, and ocean. *In: Annual Review of Fluid Mechanics*, *14*, *M. Va*(Hoult 1972).

Smith, B. L., & Neal, D. R. (2016). Particle image velocimetry. *Handbook of Fluid Dynamics: Second Edition*, 48.1-48.27.

Sumner, D. (2010). Two circular cylinders in cross-flow: A review. *Journal of Fluids and Structures*, *26*(6), 849–899.

Tanino, Y., Nepf, H. M., & Kulis, P. S. (2005). Gravity currents in aquatic canopies. *Water Resources Research*, *41*(12), 1–9.

Thomas, L. P., Dalziel, S. B., & Marino, B. M. (2003). The structure of the head of an inertial gravity current determined by particle-tracking velocimetry. *Experiments in Fluids 2003 34:6*, *34*(6), 708–716.

Ungarish, M. (2009). An Introduction to Gravity Currents and Intrusions. In *An Introduction to Gravity Currents and Intrusions* (Issue April 2009).

Zhang, X., & Nepf, H. M. (2008). Density-driven exchange flow between open water and an aquatic canopy. *Water Resources Research*, *44*(8), 1–12.

Zhu, J. B. (2006). *PIV observation of instantaneous velocity structure of lock release gravity currents in the slumping phase*. *11*, 262–270.

```
% Convert gray levels to density values employing the calibration curves
% Input information
ny = 98; Ly = 255;% to cut the image
T0=5;% index image of gate removal
Ti=8; %time index where the analysis will start
name_base='G14_R1_09';
main_path='F:\Joao\G14\R1\'; %path to the test folder

% load calibration data
load('F:\Joao\Calib0.09_lock\avg_figure\curvas_calibracao_0.09lock.mat') %load calibration data
pixel=pixel(ny:Ly,:,:);
% Process current images
%read images
Files = dir(strcat([main_path 'Undistortedimage\'], '*.bmp*')); %To read all the figures of the current

%To order the images file name
ML=cell(1,length(Files));
for c = 1:length(Files)
    ML{c} = Files(c).name;
end
ML = natsortfiles(ML);
A=double(imread([main_path 'Undistortedimage\' ML{1}]));
A = A(ny:Ly,:);
Tf=length(ML);
density = zeros(size(A,1),size(A,2),Tf-Ti+1);
clear A;

for k=Ti:Tf
    time = (k-T0)*deltaT; % calculation of time instant
    A=double(imread([main_path 'Undistortedimage\' ML{k}]));
    A = A(ny:Ly,:);
    for i=1:size(A,1)
        for j=1:size(A,2)

            CAL =reshape(pixel(i,j,:),1,size(pixel,3));
            RGB = A(i,j);
            [CAL, index] = unique(CAL);
            % if greylevel is out of scope it gets the limit
            if RGB > max(CAL)
                RGB = max(CAL);
            elseif RGB < min(CAL)
                RGB = min(CAL);
            end
            % linear regression to find the density value
            if length(CAL) == 1
               density(i,j,k-Ti+1) = Rho(end);
            else
                density(i,j,k-Ti+1) = interp1(CAL,Rho(index),RGB);
            end
        end
    end
end

save([main_path 'Results\density_database_' name_base '.mat'],'density','T0',...
    'Ti','deltaT','ny','Ly','Tf')
```

Appendix 1: Code for determine density levels from calibration

```
g0 = 0.09; % target test reduced gravity
ensaio = 'G14';
Rep = 10; % Number of test repetition
mainpath = 'F:\Joao\G14\'; % Path to the data folder being analysed
rho0 = [995.95  995.47  995.99  995.28  995.45  995.65  995.62  995.38  995.45  995.48]; % ambient fluid density
rho1 = [1004.7  1004.5  1004.9  1004.8  1004.9  1004.9  1004.9  1004.9  1004.9  1004.8]; % salt mixture density
Timef= 20.5; %end time in seconds of analysed current
% ------------------------------------------------------------------------
load([mainpath 'R' num2str(Rep) '\Results\density_database_' ensaio '_R' num2str(Rep) '_'  num2str(g0*100,'%02.f'),'.mat'])
load([mainpath 'Calib_mask\Mask_Coord_' ensaio '_R' num2str(Rep),'.mat'])
dt = deltaT; % image aquisition rate
clear deltaT
x0 = 0.3; %Lock x position
h0 = 0.203; %Fluid depth inside the lock
t = (Ti-T0)*dt:dt:Timef; % Time
IM = flipud(density); %  pixel per pixel density matrix
clear density
IMfilter=zeros(size(IM,1), size(IM,2), length(t));
line=[0.5 0.5]; %limit of normalized density contour
%
xf=zeros(1,length(t)); tt=xf;
for n=1:length(t)
    K = fspecial('gaussian',9,2);
    Z = conv2(IM(:,:,n),K,'same');
    %
    C = (Z - rho0(Rep))/(rho1(Rep) - rho0(Rep));
    C= C.*Mask;
    [XC,YC] = contour(coord_x,coord_y,C, line,'Linecolor','r','LineWidth',1);
    if isempty(XC)
        xf(n) = NaN;

    else
        aux=find(XC(2,:)>1);% detect descontinuities between isolines
        XC(:,aux)=NaN;
        XC_new(1,:)= XC(1,~isnan(XC(1,:)));
        XC_new(2,:)= XC(2,~isnan(XC(2,:)));
        xf(n) = max(XC_new(1,:));
        clear XC_new
    end
    tt(n) = t(n);
    close all
    IMfilter(:,:,n)=Z.*Mask;
end

xf_adi= (xf-x0)/x0; %normalized front position
g_red= 9.81*(rho1(Rep)-rho0(Rep))/rho0(Rep); % reduced gravity
u0= sqrt(g_red*h0); %velocity scale
tc=x0/u0;  %time scale
t_adi=tt/tc; % normalized time

rho0=rho0(Rep);
rho1=rho1(Rep);
save([mainpath 'R' num2str(Rep) '\Results\FilterIM_R'  num2str(Rep) '.mat'],'IMfilter','t','coord_x','coord_y')
```

Appendix 2: Code to compute front position

```
% --------------- change for every repetition ---------------------------------
g0 = 0.36; % target test reduced gravity
ensaio = 'G12';
Rep = 10; % Number of test repetition
mainpath = 'F:\Joao\G12\'; % Path to the data folder being analysed
Timef= 25; %end time in seconds of analysed current
% -----------------------------------------------------------------------
load([ 'F:\Joao\G15\Average\Results\Entrainment_mean_total','.mat'])
t_first=t;
Ent_first=Ent;
t_adifirst=t_adi;
load([mainpath 'R' num2str(Rep) '\Results\FilterIM_R'  num2str(Rep) '.mat'],'IMfilter','t','coord_x','coord_y')
load([mainpath 'R' num2str(Rep) '\Results\density_database_' ensaio '_R' num2str(Rep) '_'  num2str(g0*100,'%02.f'),'.mat'])
load([mainpath 'R' num2str(Rep) '\Results\Front_position_R'  num2str(Rep) '.mat'],'rho0','rhol')
dt = deltaT; % image aquisition rate
clear deltaT
x0 = 0.3; %Lock x position
h0 = 0.195; %Fluid depth inside the lock
c_width=0.174; % channel width in meters
t = (Ti-T0)*dt:dt:Timef; % Time
V0 =x0*h0*c_width; %  lock volume
Ent= zeros(1,length(t));
isoline_x=coord_x(1,:);
isoline_y=zeros(1,size(IMfilter,2));
line=[0.05 0.05]; %limit of normalized density contour
current_height=zeros(length(t),length(isoline_y));
mass=zeros(length(t),1);
for n=1:length(t)
    %Entrainment computation
     C = (IMfilter(:,:,n) - rho0)/(rhol - rho0);
     valid_C=zeros(size(C));
     valid_C(C<line(1))=NaN;
     max_C=zeros(size(C));
     max_C(C>0.8)=1;
     max_C= logical(max_C);
     max_id=zeros(1,size(IMfilter,2));
     for j=1:size(IMfilter,2)
         [id1, id2] =  find(isnan(valid_C(:,j)));
         id= find(max_C(:,j)==1,1,'last');
         if ~isempty(id)
             max_id(j)=id;
         end
         if isempty(id1)
             if ~isempty(id)
                 isoline_y(j)=coord_y(id); % to detect the current height for each coord_x
             else
                 isoline_y(j) = 0;
             end
         else
             isoline_y(j) = coord_y(min(id1),j);
         end
     end
     % To interpolate the current height on the masked vaseline part
     aux_x=find(isoline_x==0);
      isoline_y(1:aux_x+2)=0;% cut the first pixels close to the wall
      Ent(n) = (trapz(isoline_x,isoline_y)*c_width - V0)/V0;
      %Detect the current height
     current_height(n,:)=isoline_y;
     %Compute the mass conservation
     Aux_density=IMfilter(:,:,n);
     Aux_density(isnan(Aux_density))=0;
      mass(n)=trapz(coord_y(:,1),trapz(coord_x(1,:),Aux_density,2))*c_width;
end

Ent(42:end)=Ent(42:end)+Ent_first(379:378+length(Ent(42:end)))+1;%
g_red= 9.81*(rhol-rho0)/rho0; % reduced gravity
u0= sqrt(g_red*h0); %velocity scale
tc=x0/u0;  %time scale
t_adi=t/tc; % normalized time

save([mainpath 'R' num2str(Rep) '\Results\Entrainment_modified_R'  num2str(Rep) '.mat'])
```

Appendix 3: Code to compute the entrainment, current height and mass conservation

```
clear all;close all
load('G9_AV_U_5Points.mat')
load('G9_AV_V_5Points.mat')
g=0.09;
G=9;
x1=1.51; x2=1.53;x3=1.59; x4=1.65;
y1=0.06;y2=0.09;y3=0.115;
t=(1:size(U_1_1_G9_av,2))/15;
%
k_i_1_1=292; k_f_1_1=334;
k_i_1_2=292; k_f_1_2=334;
k_i_1_3=292; k_f_1_3=334;

k_i_2_1=292; k_f_2_1=334;
k_i_2_2=292; k_f_2_2=334;
k_i_2_3=292; k_f_2_3=334;

t_interv_1_1=t(k_i_1_1:k_f_1_1);
U_interv_1_1=U_1_1_G9_av((k_i_1_1:k_f_1_1));

t_interv_1_2=t(k_i_1_2:k_f_1_2);
U_interv_1_2=U_1_2_G9_av((k_i_1_2:k_f_1_2));

t_interv_1_3=t(k_i_1_3:k_f_1_3);
U_interv_1_3=U_1_3_G9_av((k_i_1_3:k_f_1_3));

t_interv_2_1=t(k_i_2_1:k_f_2_1);
U_interv_2_1=U_2_1_G9_av((k_i_2_1:k_f_2_1));

t_interv_2_2=t(k_i_2_2:k_f_2_2);
U_interv_2_2=U_2_2_G9_av((k_i_2_2:k_f_2_2));

t_interv_2_3=t(k_i_2_3:k_f_2_3);
U_interv_2_3=U_2_3_G9_av((k_i_2_3:k_f_2_3));

p_1_1=polyfit(t_interv_1_1,U_interv_1_1,1);
f_1_1=polyval(p_1_1,t_interv_1_1);

p_1_2=polyfit(t_interv_1_2,U_interv_1_2,1);
f_1_2=polyval(p_1_2,t_interv_1_2);

p_1_3=polyfit(t_interv_1_3,U_interv_1_3,1);
f_1_3=polyval(p_1_3,t_interv_1_3);

p_2_1=polyfit(t_interv_2_1,U_interv_2_1,1);
f_2_1=polyval(p_2_1,t_interv_2_1);

p_2_2=polyfit(t_interv_2_2,U_interv_2_2,1);
f_2_2=polyval(p_2_2,t_interv_2_2);

p_2_3=polyfit(t_interv_2_3,U_interv_2_3,1);
f_2_3=polyval(p_2_3,t_interv_2_3);

% Ensamble Average U
k_150=1;
k_155=64;
k_i=292; k_f=334;
load('Average_current_G9_16.mat');
U_G9_av_pre_cil=U_av(:,k_150:k_155,k_i:k_f);
V_G9_av_pre_cil=V_av(:,k_150:k_155,k_i:k_f);
save(['U_G' num2str(G) 'AV_pre_cil'],['U_G' num2str(G) '_av_pre_cil']);
save(['V_G' num2str(G) 'AV_pre_cil'],['V_G' num2str(G) '_av_pre_cil']);
```

Appendix 4: Code to define the velocity plateau regarding the current head

```
U_av_G9_pre_cil=mean(U_G9_pre_cil,3);
V_av_G9_pre_cil=mean(V_G9_pre_cil,3);

for ii=1:size(U_G9_pre_cil,3)
    U_fluct_G9_pre_cil(:,:,ii)=U_G9_pre_cil(:,:,ii)-U_av_G9_pre_cil;
    V_fluct_G9_pre_cil(:,:,ii)=V_G9_pre_cil(:,:,ii)-V_av_G9_pre_cil;
end
U_G9_2order_pre_cil=mean(U_fluct_G9_pre_cil.^2,3); %component u'^2
V_G9_2order_pre_cil=mean(V_fluct_G9_pre_cil.^2,3); %component v'^2

UV_G9_shear_stress_pre_cil=mean(U_fluct_G9_pre_cil.*V_fluct_G9_pre_cil,3);

U_G9_3order_pre_cil=mean(U_fluct_G9_pre_cil.^3,3);
V_G9_3order_pre_cil=mean(V_fluct_G9_pre_cil.^3,3);

U2_G9_3order_pre_cil=mean(U_fluct_G9_pre_cil.*U_fluct_G9_pre_cil.*V_fluct_G9_pre_cil,3);
V2_G9_3order_pre_cil=mean(U_fluct_G9_pre_cil.*V_fluct_G9_pre_cil.*V_fluct_G9_pre_cil,3);
%  adimensional moment
u_G9_scale=nanmean(nanmean(U_av_G9_pre_cil));
u_G9_scale=sqrt(g*h);
U_av_G9_adi_head_pre=U_av_G9_pre_cil./u_G9_scale;
V_av_G9_adi_head_pre=V_av_G9_pre_cil./u_G9_scale;

UU_G9_adi_head_pre=U_G9_2order_pre_cil./(u_G9_scale.^2);
VV_G9_adi_head_pre=V_G9_2order_pre_cil./(u_G9_scale.^2);
UV_G9_adi_head_pre=UV_G9_shear_stress_pre_cil./(u_G9_scale.^2);

UUU_G9_adi_head_pre=U_G9_3order_pre_cil./(u_G9_scale.^3);
VVV_G9_adi_head_pre=V_G9_3order_pre_cil./(u_G9_scale.^3);
UUV_G9_adi_head_pre=U2_G9_3order_pre_cil./(u_G9_scale.^3);
UVV_G9_adi_head_pre=V2_G9_3order_pre_cil./(u_G9_scale.^3);
```

Appendix 5: Code to compute the order moments for the current head

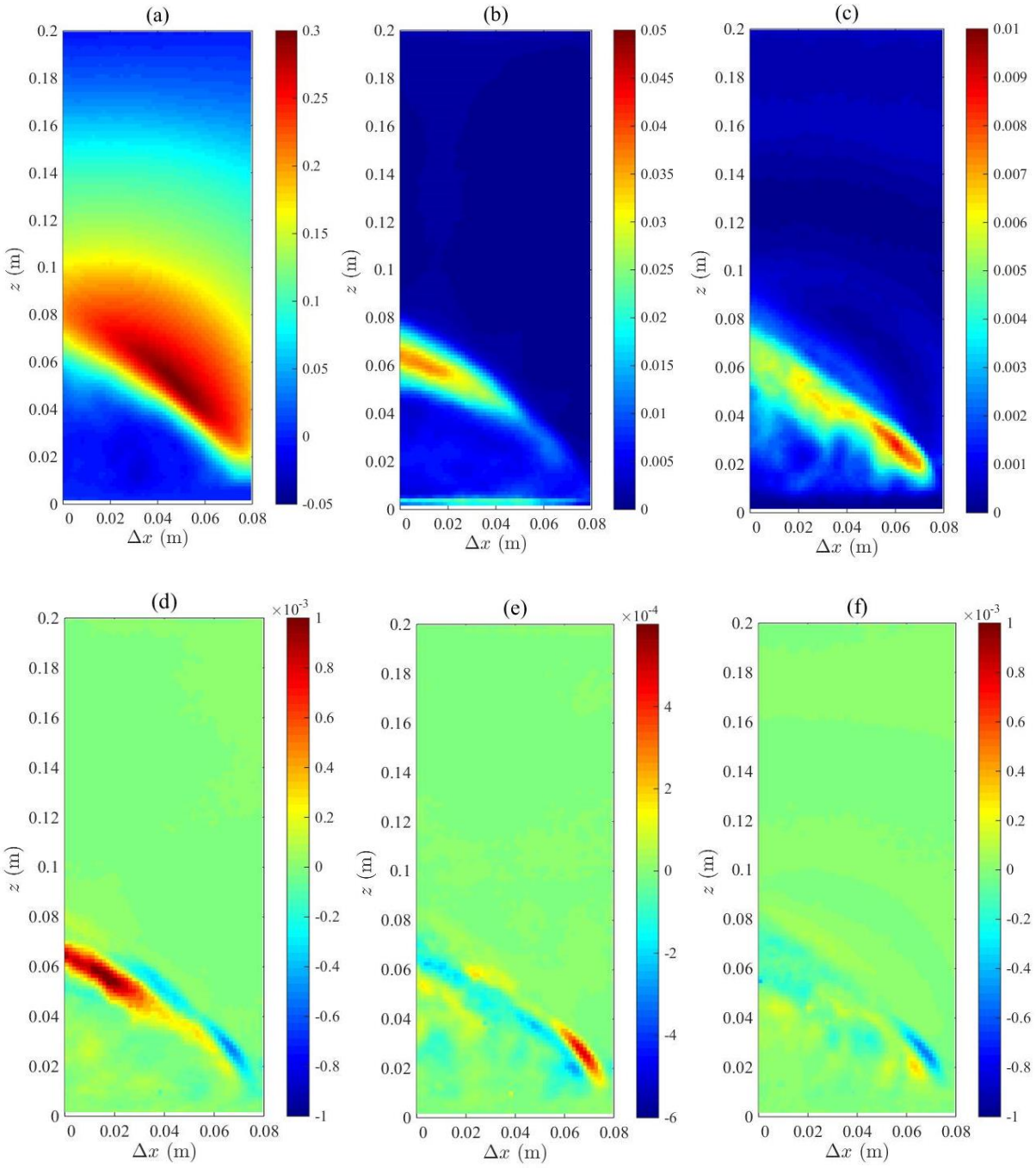

Appendix 6: Order moments in the head for current with $g' = 0.09\ \mathrm{m}/s^2$: (a) $\overline{w}$; (b) $\overline{u'u'}$; (c) $\overline{w'w'}$; (d) $\overline{u'u'w'}$; (e) $\overline{u'w'w'}$; (f) $\overline{w'w'w'}$.

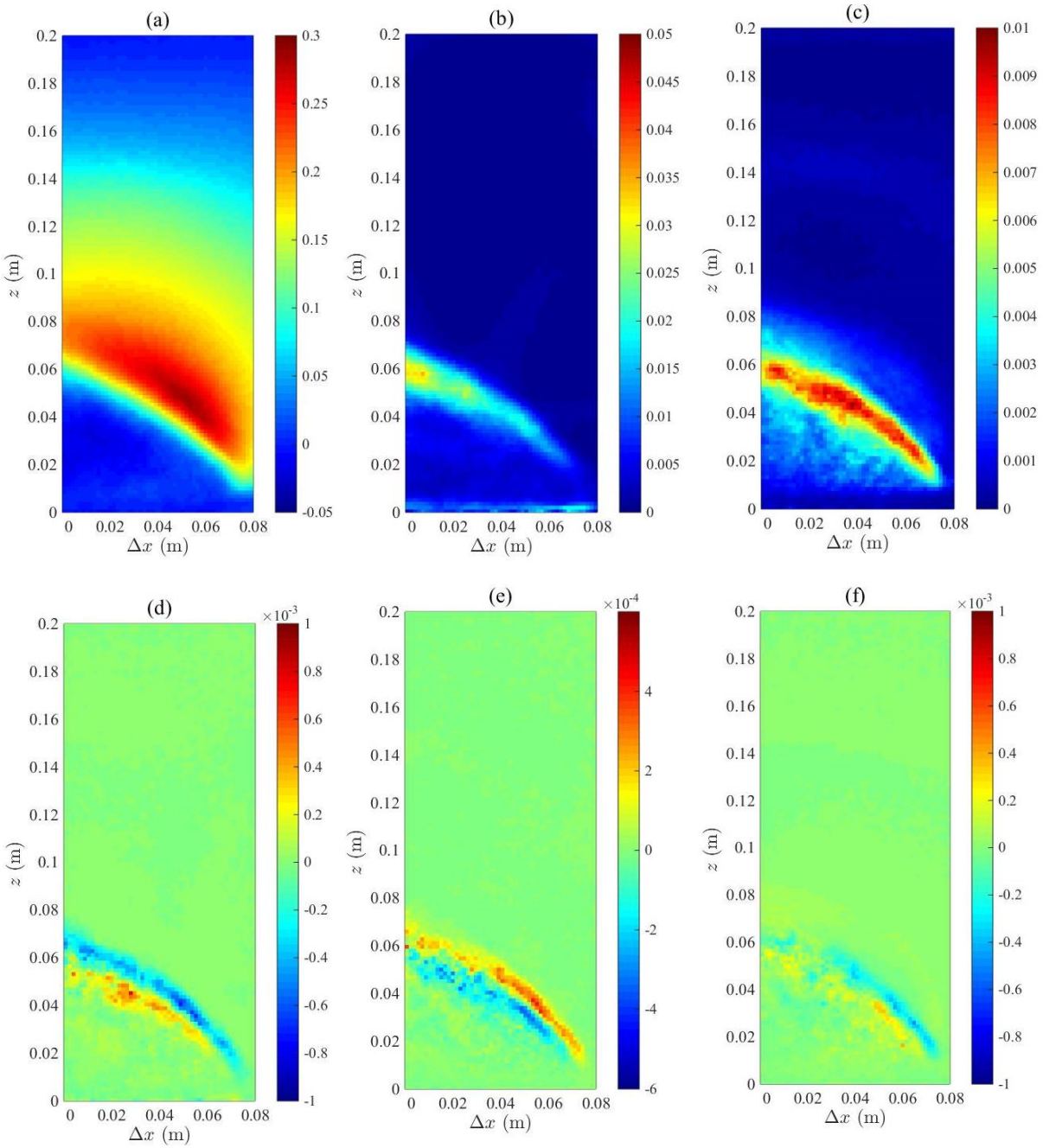

Appendix 7: Order moments in the head for current with $g' = 0.36\ \mathrm{m}/s^2$: (a) $\overline{w}$; (b) $\overline{u'u'}$; (c) $\overline{w'w'}$; (d) $\overline{u'u'w'}$; (e) $\overline{u'w'w'}$; (f) $\overline{w'w'w'}$.

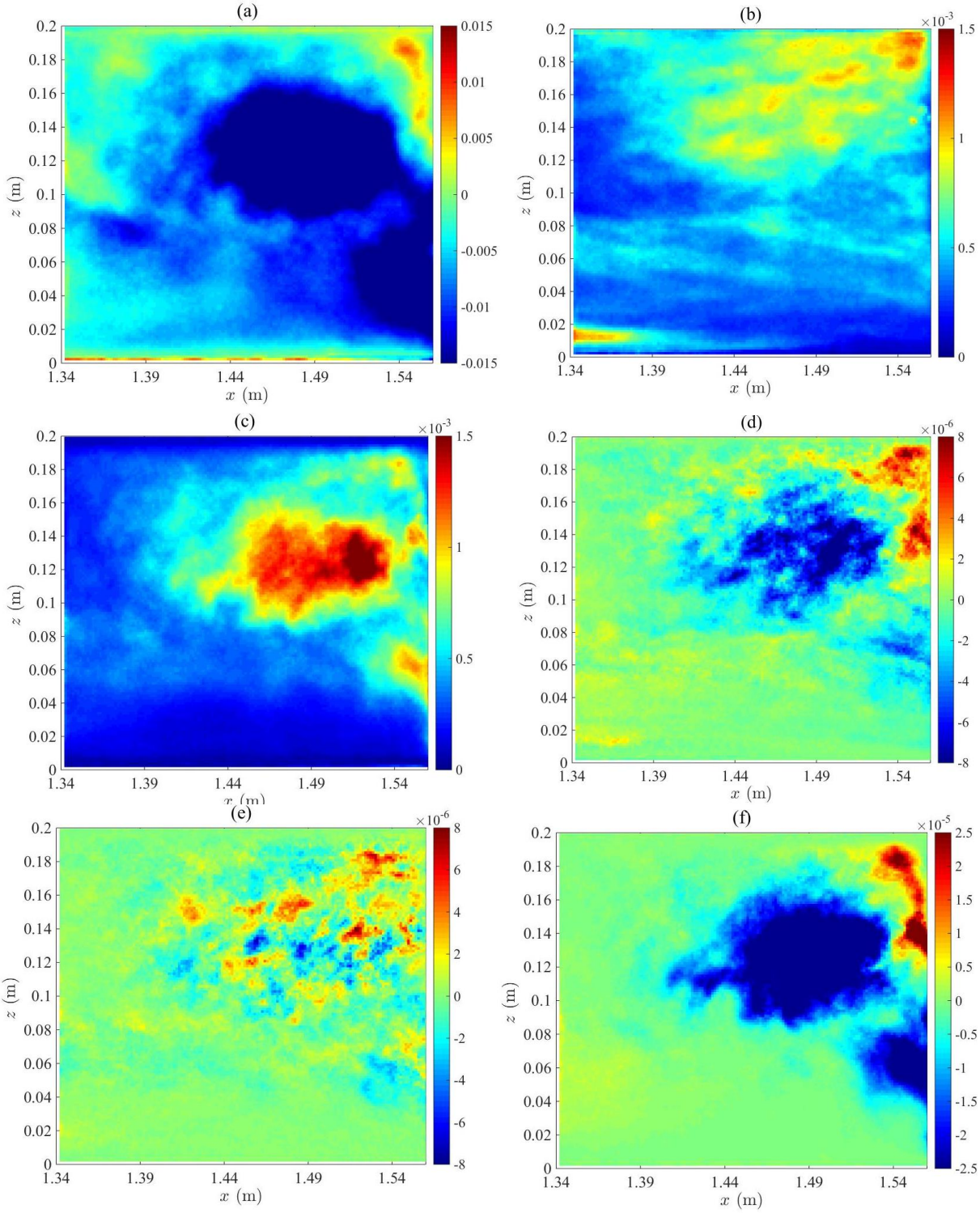

Appendix 8: Order moments in the tail for current with $g' = 0.09\ \mathrm{m}/s^2$; (a) $\overline{w}$; (b) $\overline{u'u'}$; (c) $\overline{w'w'}$; (d) $\overline{u'u'w'}$; (e) $\overline{u'w'w'}$; (f) $\overline{w'w'w'}$.

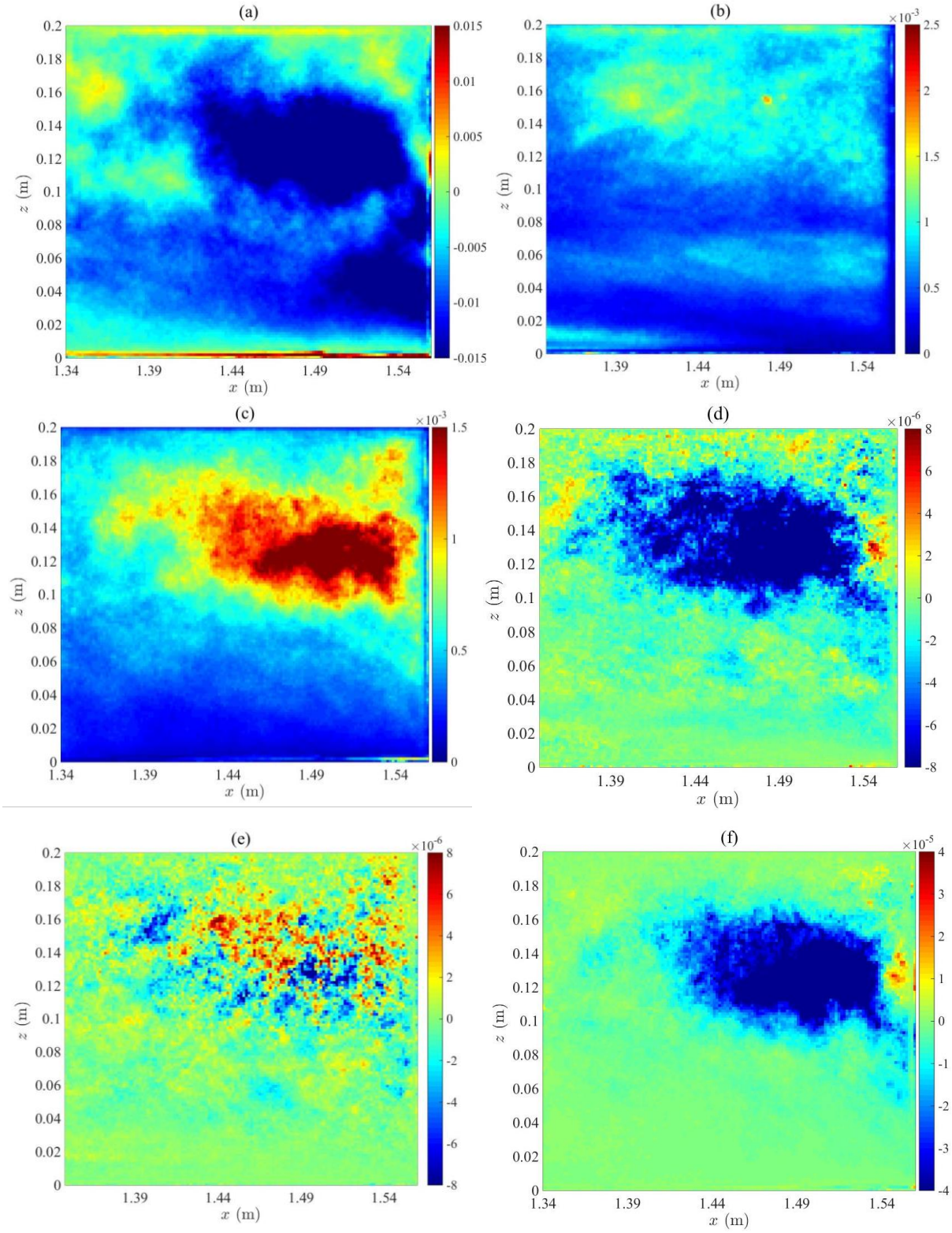

Appendix 9: Order moments in the tail for current with $g' = 0.36\ \mathrm{m}/s^2$: (a) $\overline{w}$; (b) $\overline{u'u'}$; (c) $\overline{w'w'}$; (d) $\overline{u'u'w'}$; (e) $\overline{u'w'w'}$; (f) $\overline{w'w'w'}$

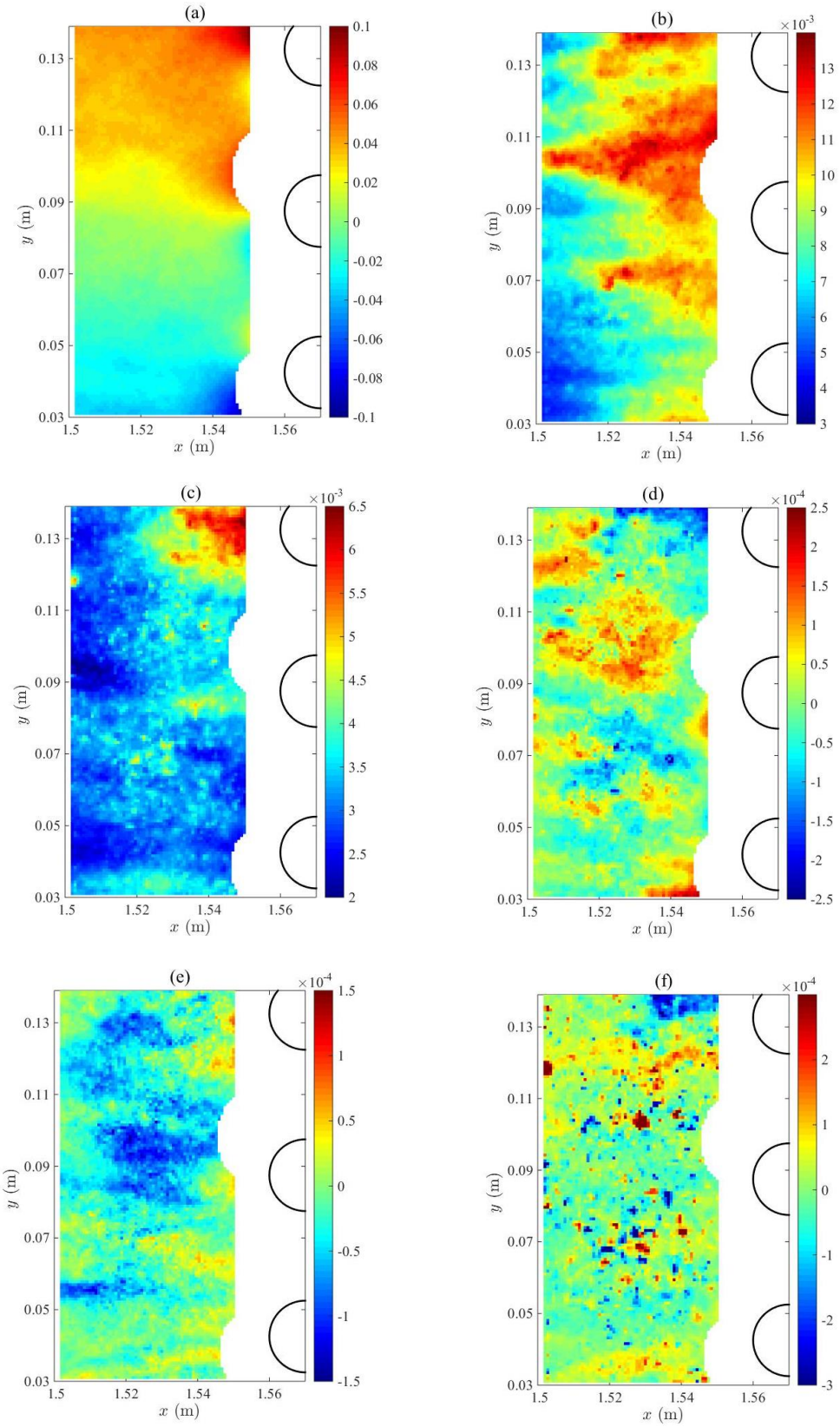

Appendix 10: Order moments in the head for current with $g' = 0.09\ \mathrm{m}/s^2$: (a) $\bar{v}$; (b) $\overline{u'u'}$; (c) $\overline{v'v'}$; (d) $\overline{u'u'v'}$; (e) $\overline{u'v'v'}$; (f) $\overline{v'v'v'}$

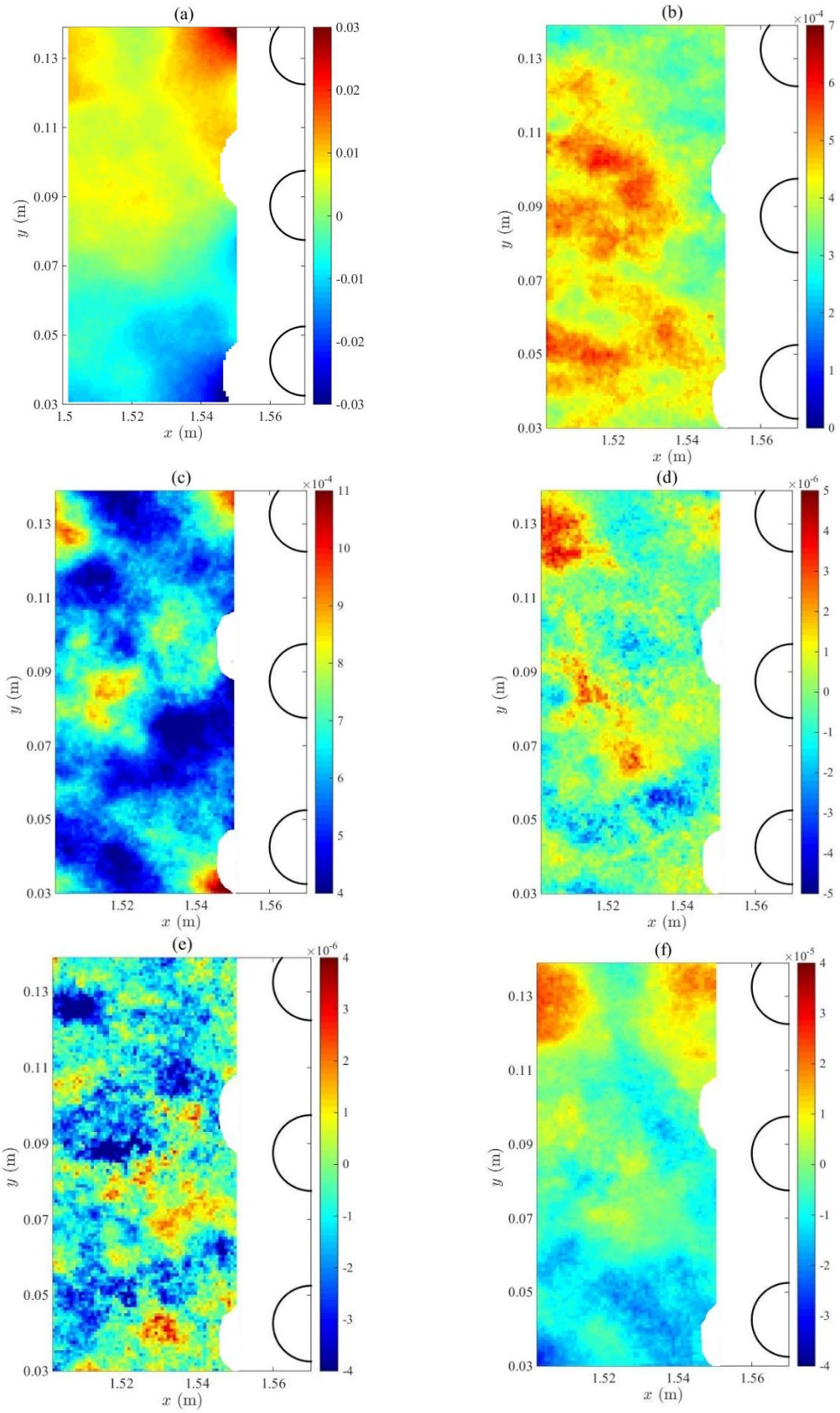

Appendix 11: Order moments in the tail for current with $g' = 0.09\ \mathrm{m}/s^2$: (a) $\bar{v}$; (b) $\overline{u'u'}$; (c) $\overline{v'v'}$; (d) $\overline{u'u'v'}$; (e) $\overline{u'v'v'}$; (f) $\overline{v'v'v'}$